

5-2013

A Preliminary Discourse on Adhesion of Nanofibers Derived from Electrospun Polymers

Pei Chen

University of Akron, main campus

Please take a moment to share how this work helps you [through this survey](#). Your feedback will be important as we plan further development of our repository.

Follow this and additional works at: http://ideaexchange.uakron.edu/mechanical_ideas



Part of the [Mechanical Engineering Commons](#)

Recommended Citation

Chen, Pei, "A Preliminary Discourse on Adhesion of Nanofibers Derived from Electrospun Polymers" (2013). *Mechanical Engineering Faculty Research*. 675.

http://ideaexchange.uakron.edu/mechanical_ideas/675

This Dissertation is brought to you for free and open access by Mechanical Engineering Department at IdeaExchange@UAKron, the institutional repository of The University of Akron in Akron, Ohio, USA. It has been accepted for inclusion in Mechanical Engineering Faculty Research by an authorized administrator of IdeaExchange@UAKron. For more information, please contact mjon@uakron.edu, uapress@uakron.edu.

A PRELIMINARY DISCOURSE ON ADHESION OF NANOFIBERS DERIVED
FROM ELECTROSPUN POLYMERS

A Dissertation

Presented to

The Graduate Faculty of The University of Akron

In Partial Fulfillment

of the Requirements for the Degree

Doctor of Philosophy

Pei Chen

May, 2013

A PRELIMINARY DISCOURSE ON ADHESION OF NANOFIBERS DERIVED
FROM ELECTROSPUN POLYMERS

Pei Chen

Dissertation

Approved:

Accepted:

Advisor
Dr. Shing-Chung Wong

Department Chair
Dr. Celal Batur

Committee Member
Dr. Gregory N. Morscher

Dean of the College
Dr. George K. Haritos

Committee Member
Dr. Shengyong Wang

Dean of the Graduate School
Dr. George R. Newkome

Committee Member
Dr. George G. Chase

Date

Committee Member
Dr. Todd A. Blackledge

Committee Member
Dr. Gunjin Yun

ABSTRACT

To bio-mimic gecko's foot hair, which possess high adhesion strength and can be re-usable for lifetime, fibrous membranes are fabricated by electrospinning to provide sufficient adhesion energy. Shaft-loaded blister test (SLBT) is firstly used to measure the work of adhesion between electrospun membrane and rigid substrate.

Poly(vinylidene fluoride) (PVDF) were electrospun with an average fiber diameter of 333 ± 59 nm. Commercial cardboard with inorganic coating was used to provide a model substrate for adhesion tests. In SLBT, the elastic response PVDF was analyzed and its adhesion energy measured. FEA model with cohesive layer is developed to evaluate the experiment results. The results show SLBT presented a viable methodology for evaluating the adhesion energy of electrospun polymer fabrics. Electrospun membranes with different fiber diameter are tested for their distinctive adhesion property. Five sets of PVDF membranes with different fiber diameters (from 201 ± 86 nm to 2724 ± 587 nm) are electrospun for size effect evaluation. Obtaining testing results from SLBT adhesion test, adhesion energy ranges from 258.83 ± 43.54 mJ/m² to 8.06 ± 0.71 mJ/m². Significant size effect is observed, and electrospun membrane composing from finer fibers possesses greater adhesion energy. Thickness effect is also evaluated. By stacking multiple layers of electrospun membrane together,

membrane samples with different thickness are produced. Test results illustrate thick membrane trends to debond easier than thin membrane.

After considering the characteristic of electrospun membrane, the effect of substrate is also evaluated. One approach is made by substituting SiC substrates with different roughness for cardboard substrate. The grit size of the SiC substrates varies from 5 μm to 68 μm . A correlation between adhesion energy and mean peak and valley roughness (Rz) is established from mechanical interlocking theory. The other approach is comparing adhesion energies if substrate is cast film or electrospun fibrous substrate. Between electrospun PCL membranes, adhesion energy is exhibited at $305.0 \pm 41.9 \text{ mJ/m}^2$. This value is 1.32 times larger than the adhesion energy between electrospun PCL membrane and cast PCL film. The high adhesion energy is attributed to the large surface contact and interlocking effect initiated by the amorphous fiber morphology of the electrospun PCL membranes. The results establish a novel methodology and provide a feasible way to control the adhesion properties of electrospun membranes.

In the end, a unique approach to fabricate PVDF/PVA hollow fiber structure is presented. Hollow structure is potential used for mimicking muscular contraction and extension, which will need to fill with functional fluid into the fiber. The fabrication methodology includes co-axial electrospinning of PVDF and PVA solutions, and a water assisted route to mitigate secondary erosion. Without solvent erosion, PVDF/PVA fibers exhibit smooth inner and outer surfaces and hollow structure. Furthermore, the hollow fiber diameter and wall thickness are controllable by the feed rate of PVA solution in

electrospinning. SLBT test is adopted to determine the adhesion energy between hollow fiber and rigid substrate. The hollow structure exhibited better adhesion performance compare to solid fiber in similar diameter.

Overall, SLBT test is adopted to determine the adhesion energy of electrospun membrane for the first time. Size of the fibers, thickness of the membrane, topography of the substrate, loading speed and materials of the substrate are the considered parameters in this study. Contribution is made to establish adhesion mechanism of electrospun membrane. Applications of the electrospun membrane are developed for potential nano-connector and hollow piezoelectric fibers.

ACKNOWLEDGEMENTS

First and foremost, I would like to thank my advisor Dr. Shing-Chung Wong for all his guidance, friendship, support, constant availability, patience, and willingness to answer my questions during the course of this study.

I would like to thank the Department of Mechanical Engineering, College of Polymer Science and Polymer Engineering at The University of Akron. I am deeply thankful to Dr. Todd Blackledge to allow me to use the NanoBionx at Biology Department. I am also genuinely thankful to Dr. Rong Bai for teaching me how to use the atomic force microscope among other key instruments in my research. I would thank Prof. Kai-Tak Wan from Northeastern University on his effort on mathematical modeling.

I really want to thank Dr. Haining Na for his help on experimental design and data processing. I also want to thank Mr. Wenzhi Wang for his help on Numerical Modeling by ABAQUES. I would like to thank all my friends including each member of Dr. Wong's group for their help and friendship.

At the end, I would like to profoundly thank my family giving my continuous effort on my research.

TABLE OF CONTENTS

	Page
LIST OF FIGURES.....	xiii
LIST OF TABLES.....	xx
CHAPTER	
I. INTRODUCTION.....	1
1.1 State of Problems.....	1
1.2 Scope of Research.....	3
II. LITERATURE REVIEW.....	5
2.1 Existing Adhesives Technologies.....	5
2.1.1 Physically Hardening Adhesives.....	6
2.1.2 Chemically Curing Adhesives.....	7
2.1.3 Pressure Sensitive Adhesives.....	10
2.2 Gecko-Inspired Dry Adhesives.....	12
2.2.1 Mechanism of Gecko Adhesive.....	12
2.2.2 Types of Gecko-Inspired Adhesives.....	14
2.3 Mechanism of Adhesion.....	20

2.3.1 Physical Adsorption.....	20
2.3.2 Mechanical Interlocking.....	22
2.3.3 Diffusion.....	24
2.3.4 Electrostatic Interactions	24
2.3.5 Weak Boundary Layer.....	25
2.4 Existing Models for Adhesive Contact	25
2.4.1 The Work of Adhesion	25
2.4.2 Adhesion Model for Adhesive Contact	26
2.5 Methods of Adhesion Measurement	29
2.5.1 Direct Pull-Off Test.....	29
2.5.2 Indentation Adhesion Test.....	31
2.5.1 Peel Test	32
2.5.2 Blister Test.....	33
2.6 Electrospinning Technology	36
2.6.1 Key Parameters of Electrospinning	40
2.7 Polyvinylidene Fluoride (PVDF)	43
2.8 Polycaprolactone (PCL)	47
2.9 Wong and Coworkers' Recent Work on Adhesion between Electrospun Fibers.....	52

III. RATIONALES OF THE DISSERTATION	58
3.1 Hypothesis	59
3.2 Validation	60
IV. EXPERIMENTAL METHODS	62
4.1 Fabrication of Electrospun Nonwoven.....	62
4.2 Polymer Film Casting.....	64
4.3 Setup for SLBT Adhesion Measurement	64
4.4 Scanning Electron Microscopy (SEM) characterization.....	68
4.6 Atomic Force Microscopy (AFM) Measurement.....	69
4.7 Tensile Test	71
4.8 Differential Scanning Calorimetry (DSC).....	71
4.9 Wide-Angle X-ray Diffraction (WAXD).....	72
4.10 Fourier Transform Infrared Spectroscopy (FTIR)	74
V. THEORETICAL STUDY BASED ON SLBT TEST.....	75
5.1 Governing Equation of SLBT Test	75
5.2 Adhesion Energy Calculation.....	78
5.3 Evaluation by Numerical Method	80
5.3.1 Problem Formulation	80
5.3.2 Numerical modeling	82

VI. MEASUREMENT OF ADHESION WORK BETWEEN ELECTROSPUN MEMBRANE AND RIGID SUBSTRATE.....	86
6.1 Introduction.....	86
6.2 Sample Preparation.....	87
6.3 Morphology of Electrospun PVDF Membrane and Rigid Substrate.....	89
6.4 Evaluation of the Adhesion Energy.....	90
6.5 Comparison of Elastic Modulus.....	98
6.6 FEA Results Comparison.....	99
6.7 Conclusions.....	102
VII. EFFECT OF FIBER DIAMETER ON ADHESION ENERGY OF ELECTROSPUN MEMBRANE.....	103
7.1 Introduction.....	103
7.2 Sample Preparation.....	103
7.3 Experimental Work.....	104
7.4 Morphology of Electrospun Membranes from Different Solutions.....	106
7.5 Effect of Fiber Diameter on Tensile Properties.....	109
7.6 Effect of Fiber Diameter on Applied load and Debonding Radius.....	111
7.7 Effect of Fiber Diameter on Adhesion Energy.....	113
7.8 Effect of Membrane Thickness on Adhesion Energy.....	116
7.9 Crystallinity of PVDF membranes.....	119
7.10 Conclusions.....	120

VIII. EFFECT OF SUBSTRATE MICROTOPOGRAPHY ON ADHESION PROPERTY OF ELETROSPUN MEMBRANE	122
8.1 Introduction	122
8.2 Materials Preparation	123
8.3 Morphology Study of SiC Substrate	126
8.4 Adhesion Test between Electrospun PCL membrane and SiC substrate	127
8.5 Effect of Substrate on the Work of Adhesion	131
8.6 Effect of Loading Speed on Adhesion Energy	133
8.7 Conclusions	135
IX. ADHESION BETWEEN ELECTROSPUN PCL MEMBRANES: DUE TO VARIOUS SUBSTRATES.....	137
9.1 Introduction	137
9.2 Sample Preparation	138
9.3 Surface Morphology.....	139
9.4 Adhesion Characterization	141
9.5 Calculation of Adhesion Energy	147
9.6 Conclusions	150
X. FABRICATION OF ADHESION ENERGY BETWEEN HOLLOW FIBERS AND RIGID SUBSTRATE	151
10.1 Introduction	151
10.2 Co-Axial Electrospinning of PVDF/PVA Hollow Fibers	153

10.3 Formation of PVDF/PVA Hollow Fibers.....	155
10.4 Diameters of the Hollow Fibers	158
10.5 Adhesion Test between Hollow Fibers and Rigid Substrate.....	160
10.6 Crystalline Structures of PVDF Hollow Fibers.....	163
10.7 Conclusions	167
XI. SUMMARY	168
11.1 Conclusions	168
11.2 Suggestion on Future Work.....	170
REFERENCES	175

LIST OF FIGURES

Figure	Page
1.1 Schematic of cohesion failure and adhesion failure. Cohesion failure causes a material damage, and adhesive failure is an interfacial delamination.	2
2.1 A schematic to illustrate the mechanism of anaerobic adhesives. Yellow circles represent oxygen, white cycles represent the monomers, and the red cycles represent peroxide molecules. (a) In the oxygen-riched condition, the monomers are connected by the peroxide molecules, remain in liquid state. (b) Once the oxygen is limited, the peroxides change to free radicals. (c) Monomers begin to form monomer chains, and a macro molecular is finally formed.	9
2.2 Mechanism of PSA. For figure (a)-(d), red layer on the top represents the back of PSAs, the light blue layer in the middle represents the functional polymer adhesive layer, and the dark blue layer underneath is the adherend. (a) Before contacting with adherend, the polymer adhesive layer is undeformed. (b) Adhesive layer deformed to occupy the space among the asperities of the adherend. Larger applied pressure will cause more intimate contact with adherend, and the bonding strength is enhanced. (c) Due to the high normal and shear adhesion strength, Peeling is the easiest way to release PSA from adherend. (d) A novel PSA can be releasead by stretching. Horizontal elongation of adhesive layer suspend the adhesion layer from the adherend.	11
2.3 A schematic to present the bunching issue of nanohairs (a) An array of polyimide nanohairs and (b) due to the lack of self-support ability, bunching of the nanohairs happened after testing, leads to a reduction in adhesive force.	16
2.4 Multiwalled carbon nanotube structures: (a) grown on silicon by chemical vapor deposition, (b) transferred into a PMMA matrix and then exposed on the surface after solvent etching [41]	17
2.5 Directed self-assembly-based method of producing high-aspect-ratio micro/nanofibers. (a) A layer of polymer solution (in red) lays upon a conductive place (in yellow), and a voltage is applied to two parallel plates (in yellow). (b) aligned pillars are formed between parallel plates.	18
2.6 Contact Mechanical models, Hertz, JKR, Brandly and DMT.	27

2.7 A schematic of direct pull-off test	30
2.8 A schematic of indentation adhesion test.....	31
2.9 A schematic of peel test	33
2.10 Schematics of the geometries of various blister tests: (a) standard blister test; (b) constrained blister test;(c) island blister test and (d) peninsula blister test.....	34
2.11 (a) A schematic of electrospinning station; (b) polymer nonwoven produced by electrospinning.....	38
2.12 A schematic representation of the orientation of molecular chain inside the PVDF electrospun fiber, and also the conformation of the helical structure of the chain. ...	39
2.13 Repeat unite of polyvinylidene fluoride	43
2.14 XRD spectra for the raw PVdF material, and the corresponding electrospun PVdF membrane and PVdF fiber-based polymer electrolyte [135].....	46
2.15 FT-Raman spectra for the raw PVdF material, and the corresponding electrospun PVdF membrane [135].....	46
2.16 Repeat unit of PCL.....	47
2.17 WCAs of (a) random and (b) uniaxially aligned PCL webs. Comparison of WCA measurements taken at 5 min for two differently oriented fiber mats [142].	49
2.18 Representative stress–strain curves of single fibers obtained from tensile tests. Fibers with small diameters are seen to have higher modulus and strength [144]. ...	50
2.19 Plot of tensile modulus vs. fiber diameter. Tensile modulus increases with a decrease in fiber diameter [144].	51
2.20 Plot of tensile strength vs. fiber diameter. Tensile strength increases with a decrease in fiber diameter [144].	51
2.21 Schematic of the dry adhesion test. (a) The cardboards are cut into U shapes and mounted on the nanoforce tensile tester (b) Two fibers are arranged in the cross-cylinder geometry, and the contact circle has a diameter of 2a (c). Vertical compressive load deforms the tw0 fibers into V-shapes [8].....	52
2.22 Applied external load F measured as a function of crosshead displacement u for PCL fibers of three different radii [8].	53
2.23 Measured “pull-off” force as a function of fiber radius. Data are fitted to a linear relationship according to the JKR theory [8].....	54

2.24 Adhesive strength as a function of fiber radius. The adhesion strength increases with decreasing fiber radius [8].	55
2.25 Adhesive force as a function of pull-off speed [145].	56
2.26 Comparison of adhesion energies between measured and theoretical data [145].	57
4.1 A schematic of electrospinning station. A syringe pump is used to control solution feeding rate, and a 10 KV voltage is applied to the needle. A costume-made rotate collector is used to collect fibers. After collecting, fibrous membrane will be peeled from the collector.	64
4.2 Digital image of tensile testing stage, microscope, and recording camera.	65
4.3 (a) Setup of SLBT adhesion test, including the load cell, lower/upper grip, home-made fixture, reference ruler, replaceable substrate and rigid shaft. (b) A close view of home-made fixture, a tested membrane is attached to the replaceable substrate. .65	
4.4 A schematic illustrating the apparatus and process of the shaft-load blister test. The apparatus is shown in (a) rigid substrate with a round hole bored through its center and clamped by a fixture. Electrospun PVDF attaches onto the top surface of the rigid substrate. Central shaft with a spherical cap located below the center of the hole offers an external load. Adhesion tests are motorized by 1" travel stage imperial (Thorlabs, MTS 25-Z) and the debonding forces are recorded by 1 N load cell (Futek Advanced Sensor Tech). The detailed dimensions of the apparatus are described in (b). Both (b) and (c) exhibit the formation of a blister and debonding between the membrane and rigid substrate with a testing speed at 20 mm/min.	67
4.5 Scanning electron microscopy (JEOL JSM-6510LV).	69
4.6 Atomic force microscopy (Ntegra Spectra, NT-MDT).....	70
4.7 Digital image of TA DSC	72
4.8 Digital image of Bruker WAXD equipment.....	73
4.9 Digital image of PerkinElmer FT-IR	74
5. 1 A Schematic of SLBT test	75
5.2 Traction-separation law	81
5.3 Simplified triangular traction-separation law	81
5.4 Computational model for SLBT.	83
5.5 A configuration of membrane and substrate after testing.	84

5.6 FEA results on element size study. Element size varies from 0.1 mm to 2 mm, and the relationship between central deflection and applied load is established.....	85
6.1 The morphology of the contact surface of electrospun PVDF (a, b) and surface composition of the rigid substrate (rigid cardboard) (c, d). SEM image of PVDF membrane (a) shows the fiber diameters fall in around 300-400 nm and the average diameter is 333 ± 59 nm (measured by Photoshop 9.0). In order to calculate the surface fiber density, electrospun fiber in the image is adjusted to bright field. And the background is changed into dark field. Bright area in (b) occupies 76.97 ± 2.05 % which shows the fiber density at the contact surface about 77 %. The top surface of the rigid cardboard is scanned by surface profiler. Calculated from the scanning curve (c), the valley depth is around 100-600 nm. Elemental analysis (d) of the cardboard surface shows contents of inorganic materials coating. The percentage of Ca, C and O are 33.54 wt%, 30.85 wt% and 34.49 wt%, respectively.....	88
6.2 A schematic of SLBT adhesion test.....	89
6.3 Debonding between electrospun PVDF membrane and rigid substrate in SLBT. The debonding is observed by optical microscope. An approximate single conical blister of electrospun membrane is formed in testing and it shows that the elastic response of the membrane appears in the tests [left side of the Figure]. The central deflection and debonding radius of the electrospun membrane blister within 10 s are measured by video recording and analyzed by Photoshop 9.0 to get the slope of w_0/a curve [right side of the Figure].	91
6.4 Externally applied force plotted as a function of blister central deflection for electrospun PVDF membrane. An average of 10 measurements is taken in sequence to show the relations between applied force and central deflection. The initial parts of $P-w_0$ curves exhibit a stable debonding between PVDF membrane and rigid substrate.	93
6.5 The work of adhesion between electrospun membrane and rigid substrate. The adhesion energy shows a slight decrease through SLBT. The average of adhesion energy between electrospun PVDF and rigid cardboard is 206 ± 26 mJ/m ²	94
6.6 SEM micrographs of PVDF membranes before (a) and after (b) blister tests. Before blister tests, uniform fiber could be observed at the surface of electrospun PVDF membrane (a). After the blister test, some fibers are flattened slightly and fuse together at the intersections (b, circled by red ellipses). Roller is utilized to fix the PVDF membranes onto cardboard papers. After ten measurements, the fiber morphology changes slightly due to excessive pressure. It leads to slight decrease in adhesion energy of the PVDF membrane.	94
6.7 3-D AFM topographic imaging and surface profiling of (a) electrospun PVDF membrane and (b) a cast PVDF film . Electrospun PVDF membrane exhibits fiber morphology and a uneven surface. The membrane produces additional cylindrical	

contact area against the rigid substrate thereby enhancing adhesion energy. The cast film only shows a relatively smooth and featureless surface in comparison to the membrane. The actual contact area between cast film and the rigid substrate is lower.97

6.8 Comparison of data from numerical model and experimental SLBT test. Hollow circles illustrate data from numerical modeling..... 101

6.9 Comparison of data from numerical model and experimental SLBT test. 101

7.1 (a) The setup of SLBT test, the electrospun membrane is represented in red color, and the blue color shows the rigid substrate, (b) The test procedure of SLBT is illustrated, the membrane will keep debonding when a displacement is applied vertically. (c) The relationship between applied force and central deflection, central deflection and debonding radius are obtained, which are the key parameters to calculated the adhesion energy. 106

7.2 SEM images (a)-(e) corresponding to sample A-E. 1(f) illustrates fiber diameter distribution. From sample A to sample E, fiber diameter gradually increases. Scale bar is 5 μm 108

7.3 The stress-strain relationships for Sample A-E obtain from tensile test..... 109

7.4 Relationship between fiber diameter and elastic modulus of electrospun membrane, as determined by tensile test. 110

7.5 Applied load (P) vs central deflection (w_0) for five samples tests (A, B, C, D, E). Linear elastic deformation occurs for every curve in the initial region. Each test reveals a yielding point around 2mm. The P/w_0 value is obtained from each curve's linear section, 24.6 N/m , 19.4 N/m , 13.7 N/m , 10.5 N/m , 0.35 N/m for sample A, B, C, D, E, respectively..... 111

7.6 Relationship between adhesion energy and fiber diameter for sample A-E. A significant increase trend is established from sample E ($8.06\pm 0.71 \text{ mJ/m}^2$) to A ($258.83\pm 43.54 \text{ mJ/m}^2$). The solid line shows a polynomial regression of experiment data. Red dash-dot line illustrates a proportional relationship as $\propto 1/d$ 112

7.7 Applied load vs central deflection for PVDF membranes with different thickness. . 117

7.8 Central deflection vs debonding radius for PVDF membranes with different thickness. 117

7.9 Relationship between adhesion energy and numbers of membrane layer. 118

7.10 (a) Thin membrane has not beading moment. (b) Thick membrane has a bending and compression in the membrane, more energy will be consumed.	119
7.11 DSC thermograms of Sample A-E.....	120
8.1 SEM image of electrospun PCL membrane, scale bar is 5 μ m.....	124
8.2 SEM images of SiC substrate a-e. The scale bar is 100 μ m.	125
8.3 The surface profile of substrate a-e. he grit size is different, and confirmed with manufacture's data. The peak and valley distance is also various from substrate a-e.	125
8.4 The relationship between grit size and the mean peak and valley roughness (R_z), the grit size information is supplied by manufacturer, and the R_z is obtained from the surface profile of each substrate.	126
8.5 The relationship between central deflection and applied force for substrate a-e.....	128
8.6 The relationship between P/w_0 (applied force/central deflection) and R_z (shown in triagler) and the relationship between w_0/a (central deflection/debonding radius) and R_z . Both show a linear increase trend with R_z increase.	129
8.7 The relationship between adhesion energy and R_z . A linear regression is established. ...	130
8.8 The schematic for substrate effect, R_z increase causes an increase of the surface area of each grit, and thus the adhesion energy increases reasons from actual contact area increase.	130
8.9 The relationship between P/w_0 (applied force/central deflection) and loading speed (shown in triangle) and the relationship between w_0/a (entral deflection/debonding radius) and loading speed.....	134
8.10 The relationship between adhesion energy and loading speed. No obvious effect of loading speed is observed.	135
9.1 Fiber morphology and surface topography of test membrane. Test membrane is composed by electrospun PCL fibers. SEM image (a) shows the uniform fiber morphology at surface. Fiber diameters (b) are concentrated at 250-400 nm. Surface topography (c) is obtained by surface scanning with AFM. The scanning profile (d) fluctuates obviously. The height fluctuation of the membrane surface is \sim 800 nm. The test film shows fiber morphology and rough surface.	140

9.2	Surface topography and profile of membrane covers of the test substrates. Electrospun PCL membrane (a, b) and cast PCL film (c, d) are respectively used as membrane cover for the test membrane. Electrospun membrane cover shows a rough surface (a) with the height fluctuation ~ 800 nm (b). In comparison, a relative smooth surface (c) is exhibited in cast film cover. The height fluctuation of cast film is ~ 150 nm.	141
9.3	Exterior force (P) vs. central deflection (w_0) curves of SLBT by use of test substrates covered with (a) electrospun PCL membrane and (b) cast PCL film respectively. 5 measurements are taken to show the relations between exterior force and central deflection. The initial parts of P - w_0 curves exhibit linear trend concerned with the stable debonding between test membrane and membrane cover.	144
9.4	The central deflection (w_0) plotted as a function of debonding radius (a) for the test membrane blister. w_0 and a of test membrane blister are measured from video record by use of (a) electrospun PCL membrane and (b) and cast PCL film covered substrates in SLBT. When w_0 is 0-2 mm, w_0 - a curves show a linear trend.	145
9.5	Adhesion energy of test membrane against membrane covers. Adhesion energy is calculated from Equation (2) by use of the data from Table 9.1. The average adhesion energy between electrospun PCL membranes (ESM vs. ESM) is 305.0 ± 41.9 mJ/m ² . This value is considered 1.32 times larger than the adhesion energy between electrospun PCL membrane and cast PCL film (ESM vs. CF).	147
9.6	A schematic to represent the interpenetration and mechanical interlocking of electrospun membrane. (a) Contact between two electrospun membranes, both of the red and blue circles are PCL membranes, red color represents the upper tested membranes, and the blue color represents the substrate membranes. The fibers entangled with each other and interlocked with each other. (b) Contact between electrospun membranes and cast film substrate. The fibers (in red) could not penetrate into the cast film, and therefore less contact area is observed, and no fiber interlocking could happen either.	150
10.1	Schematic that illustrates the set-up for coaxial electrospinning. Two different measuring pumps are used to independently control the feed rates of core and shell solutions. The inner solution is indicated by blue color. The shell solution is indicated by green. Two needles are packed in a co-axial setup. The internal needle is 0.5 mm longer than external needle. Applied voltage is kept constant at 10 kV to electrospin fibers. A rotating collector is prepared by two parallel metal wires. The distance between the two metal wires is about 9 cm, and the rotational speed is 60 rpm. H ₂ O bath underneath is utilized to assist coagulating PVDF/PVA hollow fibers simultaneously during electrospinning.	155
10.2	SEM micrographs of the PVDF/PVA hollow fibers prepared at different core/shell feed rates (mL/h) at (a) 0.1/1.7. PVDF/PVA hollow fibers exhibit the smallest diameter; (b) 0.3/1.7, the inner diameter in the PVDF/PVA hollow fibers increases;	

(c) 0.5/1.7, the thickness of the wall decreases, and approximately equals the inner diameter; (d) 0.8/1.7, the hollow fibers can be considered as thin-walled cylindrical shell, since the inner diameter is larger than the wall thickness; (e) 1.5/1.7, hollow fibers with ultra-thin wall is formed.	157
10.3 Diameters and wall thicknesses of the electrospun hollow fibers for different solution feed rates. The inner diameters of the PVDF/PVA hollow fibers increase from $1.16 \pm 0.15 \mu\text{m}$ to $6.61 \pm 1.80 \mu\text{m}$. The outer diameter increases slightly while the wall thickness of the PVDF/PVA decreases.	159
10.4 (a) An image of PVDF hollow fibers under transmission optical microscope. (b) A SEM image of PVDF hollow fibers taken from the view of cross-section.	160
10.5 Output of adhesion tests. Five different samples are tested under some test conditions. (a) Applied force vs central deflection. (b) Debonding radius vs central deflection.....	161
10.6 FTIR spectra of PVDF in the electrospun hollow fibers prepared at different core/shell feed rates (mL/h) at (a) 0.1/1.7, (b) 0.3/1.7, (c) 0.5/1.7, (d) 0.8/1.7, and (e) 1.5/1.7, respectively.	166
10.7 XRD patterns of PVDF in the electrospun hollow fibers prepared at different core/shell feed rates (mL/h) at (a) 0.1/1.7, (b) 0.3/1.7, (c) 0.5/1.7, (d) 0.8/1.7, and (e) 1.5/1.7, respectively.	166
11.1 Randomly oriented electrospun fibers are modeled as a network of randomly distributed fibers. Each fiber is considered as a connection of multiple beads (reprinted with permission from Inderscience) [228].	173

LIST OF TABLES

Table	Page
2.1 Existing fibrous dry adhesives fabrication technology.....	19
6.1 The slopes of w_0 - a and P - w_0 curves.....	95
6.2 Comparison of elastic moduli between SLBT and tensile tests.....	99
7.1 Solution preparation methods of Sample A-F.	104
7.2 Summary of materials properties determined in this study.	115
7.3 Adhesion experimental data P/w_0 , w_0/a from SLBT tests, and the work of adhesion (W) calculated for membranes with different thickness.	118
9.1 The slopes of w_0/a and P/w_0 curves.....	146
11.1 Comparison of adhesion energy with literature.....	172

CHAPTER I

INTRODUCTION

1.1 State of Problems

Recent understanding of gecko-like dry adhesives attracts much attention from researchers [1-2]. Gecko's extraordinary climbing ability has been attributed to the van der Waals force between gecko foot hairs and different surface [3]. There are efforts made by researchers to create dry adhesives which can exploit the effect. Many nano-size materials are found to possess good adhesion properties under nano-scale, like micro-cast polymer fiber [4], carbon nanotube etc.[5]. Typically the high adhesion strength is evaluated by atomic force microscopy. However, when the research is extended to macroscopic scale, a patch of nanofibers or nanotubes cannot exhibit adhesion properties as good as in microscopic scale [6]. Future research needs to be done to bridge the micro-adhesion and macro-adhesion [6].

Nano-scale adhesive materials always have low self-support characteristic [6]. Good adhesion property can be achieved if the adhesives can initiate an intimate contact area, where the contact distance is closer than cut off distance of van der Waals attractive force. However, when the adhesives are forced to detach, cohesion failure may happen before the adhesion failure. The schematic of cohesion failure and adhesion failure is shown in Figure 1.1. Cohesion failure causes a materials damage, which prevent the adhesives for

re-use. A material which is flexible enough to make intimate contact, and also possess high cohesion strength, is desired for further dry adhesive application.

Another problem is lack of effective method to evaluate adhesion properties for the materials in intermediate size. Materials in the size of few nanometer are conveniently examined by AFM, and adhesion properties can also be determined by contacting with AFM tips [6-7]. Adhesion properties of bulk materials can be evaluated by the standard ASTM adhesion tests, which are already well addressed for a long time. However, adhesion properties of materials which scale is in the range of micrometer are not well addressed. These materials always have nano-size feature, but beyond the range of AFM measurement. Classical adhesion tests are hard to apply, because the low volume of materials or the low sensitivity of the tests.

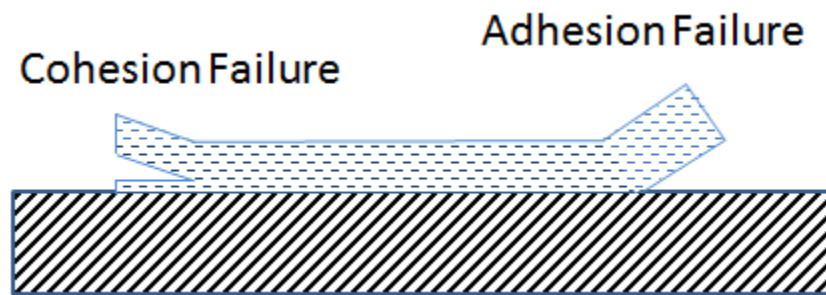


Figure 1.1 Schematic of cohesion failure and adhesion failure. Cohesion failure causes a material damage, and adhesive failure is an interfacial delamination.

1.2 Scope of Research

Electrospun fiber's extraordinary adhesion properties are demonstrated by Wong and co-workers [8]. Stickiness between electrospun polymer membranes and rigid substrates is an area of continuing interest. The desired substrates include inorganic surface, such as glass, metal, and organic surface such as wall and ceiling covered with paint. This dissertation aims to discuss the adhesion properties between electrospun fibrous membrane and rigid substrate. In this dissertation, two polymer materials are examined to understand their adhesion properties for different future applications.

Poly(vinylidene fluoride) (PVDF) is chosen as one of the electrospinning materials. PVDF is well known as a chemically inert "tough" polymer with a high dielectric constant [9]. A β -zigzag molecular conformation with the preferential orientation of the CF_2 dipoles in uniaxial orientation is useful for generating piezoelectricity [10-12]. The obtained PVDF fibers could possess flexible and piezoelectric properties at the same time. Piezoelectricity is a key characteristic to build manipulator which can mimic gecko's locomotion. Therefore, adhesion property of PVDF will be presented in this dissertation.

Polycaprolactone (PCL) is a semi-crystal liner aliphatic polyester, which possess low glass transition temperature (~ -60 °C) and low melting temperature (~ 60 °C). PCL is attractive because of its biodegradable and bioresorbable properties. PCL is widely used for biomedical applications, including drug delivery, wound healing, tissue scaffold etc. Adhesion property is an important property of PCL, and needs to be well understood.

Electrospinning technology can produce fibrous structures which are high porous, flexible, and also possess good mechanical properties. High porosity can increase the

contact areas with other object. Flexibility can ensure the contact is intimated enough. Good mechanical properties can prevent cohesion failure. Without doubt, electrospun fibers are a good candidate for high performance dry and reusable adhesives.

An effective and accurate adhesion test method for electrospun fibers also needs to be developed urgently. In this study, blister test is adopted and modified for adhesion properties measurement of electrospun fibers. In order to make the adhesion properties of electrospun fibers controllable, more study on the mechanisms between fibers and substrates need to be conducted. The effects of fibers' diameter and thickness will be investigated throughout the experimental and theoretical study. Influence of substrate's roughness and materials properties is also comprehensively addressed in this dissertation. An understanding of the adhesion properties mechanisms between polymer fibrous and different substrates will present fruitful insights in fabricating bio-mimicking dry adhesives in future work.

CHAPTER II

LITERATURE REVIEW

In chapter II, research topics related to this study are reviewed. A comprehensive understanding of existing adhesives technologies is needed. Mechanisms of major commercial adhesives are investigated and reviewed. Recent research on dry adhesives is also included, namely gecko-inspired dry adhesives. The bonding mechanism of gecko-inspired dry adhesives are discussed specifically. Adhesion mechanics and classical adhesion models are reviewed in the next, followed by existing adhesion testing technologies for macro-size adhesives. Electrospinning technology is the fiber producing technology used in the dissertation, electrospinning process is discussed, and the key parameters are studied to control fiber quality. PVDF and PCL are the polymer materials used in the study, therefore their distinctive physical properties are reviewed respectively. Finally, previous adhesion study on single electrospun fiber, which has been done by Wong and co-workers, is reviewed.

2.1 Existing Adhesives Technologies

An adhesive is a kind of material, which can bond items together. The adhesives are typically liquid or semi-liquid. A study of history shows the first evidence of glue using by human being dates back to 4000 BC [13]. Earliest adhesives were made of natural

materials, such as tree sap, beeswax, tar and etc. With the emergence of chemical industry and polymer synthetic industry, more and more adhesives formulations exploded. Today's adhesives can be classified in many different ways. In this dissertation, adhesives will be classified by their bonding mechanism. Three major catalogs of adhesives will be reviewed, physically hardening adhesives, chemically curing adhesives and pressure sensitive adhesives.

2.1.1 Physically Hardening Adhesives

Physically hardening adhesives are non-reactive adhesives, and they are in their final chemical state before applying to surface. Only polymers that can be liquefied, either melt or dissolved, can be used for physical hardening adhesives. Physically hardening adhesives provide a wide range of adhesive properties, generally good bond flexibility, and are used in a variety of applications. There are three major types of hardening adhesives: hot melts, solvent based adhesives and polymer dispersion adhesives [14].

Most of the hot melt adhesives are thermoplastics, which can be applied in molten form in the range of 65 °C -180 °C [14]. They can be solidified in room temperature to form strong bonding with various materials. Ethylene-vinyl acetate (EVA) is a particularly popular hot melt adhesive for crafts. EVA possesses good physical properties, such as good clarity, low-temperature toughness, stress-crack resistance, water resistance, UV resistance etc. EVA also has little odor, and is competitive with other safe adhesives.

Solvent based adhesives build strength through the evaporation of the solvent. The performance of solvent-based adhesives is largely determined by the polymer system in the formulation. The choice of adhesive type depends on the specific substrates and environmental resistance needed – temperature resistance, oil and plasticizer resistance, etc. Most solvent based adhesives contain flammable solvents which require proper precautions for safe handling. In addition, many Solvent based adhesives contain significant levels of volatile organic compounds (VOCs), which are often subject to regulations across the United States and worldwide.

Polymer dispersion adhesives are typically formulated from compounds including vinyl acetate polymers and copolymers (PVAC), ethylene vinyl acetate (EVA), acrylics, styrene-butadiene rubber (SBR), natural rubber latex and synthetic elastomers, and polyurethane (PUR). These adhesives are heterogeneous systems comprising a solid polymer phase dispersed in an aqueous phase. One of the major advantages is the absence of VOCs. For many water based adhesives, it is a requirement that at least one of the substrates be permeable to allow water to escape from the system. It is not surprising, then, that these materials have found wide use in bonding wood, paper, fabrics, leather and other porous substrates.

2.1.2 Chemically Curing Adhesives

Chemically curing adhesives are reactive materials that require chemical reaction to convert them from liquid to solid. Generally they can be classified into single component adhesives and two component adhesives. Single component adhesives have pre-mixed

adhesive components which are blocked normally. Only when the required condition was met, they will activate the hardener. These condition could be heat, moisture radiation etc. Two component adhesives have two reactive components which can form solid systems after mixing them. The most widely used two component adhesives include Epoxies, methyl methacrylates (MMA), silicones etc.

Anaerobic adhesives are a group of widely used single component adhesives. When the adhesive is placed in oxygen restricted space, cure proceeds quite rapidly. The mechanism of anaerobic adhesives is shown in Figure 2.1. The adhesives must remain in contact with oxygen until the time it is used, as shown in Figure 2.1 (a). The adhesive is liquid-like, and the monomers are connected by the peroxide molecules. Once the adhesive is applied to an oxygen restricted space as shown in Figure 2.1 (b), such as the joint gap during a bolt-nut assembly, the peroxides changes to free radicals rapidly, especially under the catalytic effect of metal ions. Polymerization of monomers happens as shown in Figure 2.1 (c), and thermoset polymer is formed with very high adhesion strength. The most important application of anaerobic adhesives is as liquid lock washers for screws and bolts. Because of their strong penetrating ability, they can be applied either before or after assembly.

Cyanoacrylates are known for their “instant” bonding to most surfaces. When a drop of cyanoacrylate adhesive is put on the surface of a part, the acid stabilizer molecules react with the water molecules present on the surface of the part from the relative humidity in the air. The reaction of the water and acid causes the acid stabilizer to be neutralized. The cyanoacrylate molecules then react with each other and form

polymer chains without cross-linking. Cyanoacrylates can bond most types of glass, plastics and metals, and has broad application in optics, microelectronics, transportations and medical technologies etc.

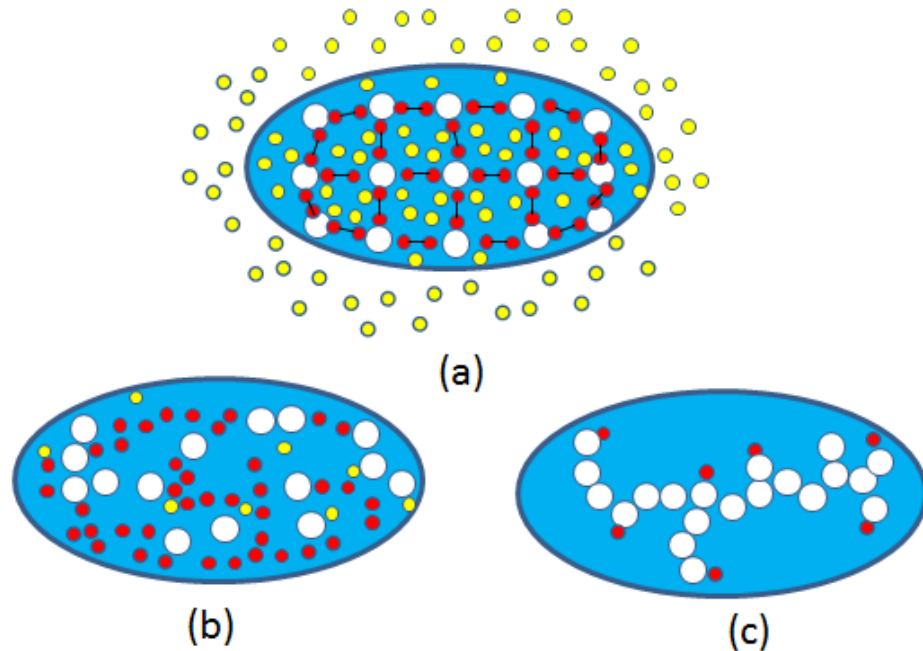


Figure 2.1 A schematic to illustrate the mechanism of anaerobic adhesives. Yellow circles represent oxygen, white circles represent the monomers, and the red circles represent peroxide molecules. (a) In the oxygen-rich condition, the monomers are connected by the peroxide molecules, remain in liquid state. (b) Once the oxygen is limited, the peroxides change to free radicals. (c) Monomers begin to form monomer chains, and a macro-molecule is finally formed.

Besides of anaerobic adhesives and cyanoacrylates, heat cure is one of the particular popular single component adhesives. Different from hot melt adhesives, heat cure adhesives initiate chemical reaction and cross-linking under heat. Cured adhesives are hard and rigid, with excellent chemical and heat resistance. Heat cured adhesives are

used very broad. They are used to bond body component and structures in automotive industry and aerospace industry, and used to bond electronics components in consumer electronics. Polyurethane and epoxy resin are the most widely used single component heat cure adhesives.

Single-component epoxy adhesives include solvent-free liquid resins, solutions in solvent, liquid resin pastes, fusible powders, sticks, pellets and paste, supported and unsupported films, and preformed shapes to fit a particular joint. Two-component epoxy adhesives are usually composed of the resin and the curing agent, which are mixed just prior to use. The components may be liquids, putties, or liquid and hardener powder. They may also contain plasticizers, reactive diluents, fillers, and resinous modifiers. The processing conditions are determined by the curing agent employed. Typical cure conditions range from 3 h at 60 °C to 20 min at 100 °C [15]. Epoxy adhesives have excellent chemical resistance and good elevated temperature capabilities. Epoxy adhesives form strong bonds to most materials, in addition to excellent cohesive strength. Epoxies yield good to excellent bonds to steel, aluminum, brass, copper, and most other metals. Similar results are obtained with thermosetting and thermoplastic plastics, as well as with glass, wood, concrete, paper, cloth, and ceramics. The adherends to which epoxy is being bonded usually determine the adhesive formulation.

2.1.3 Pressure Sensitive Adhesives

Pressure sensitive adhesives (PSAs) are most used in tape and label industry. PSAs are typically formulated from natural rubber, certain synthetic rubbers, and

polyacrylates [14-15]. PSAs form a bond simply by the application of pressure to marry the adhesive with the adherend. Once the adhesive and the adherend are in proximity, there are also molecular interactions such as van der Waals forces involved in the bond, which contribute significantly to the ultimate bond strength. PSAs exhibit viscoelastic (viscous and elastic) properties, both of which are used for proper bonding. Pressure sensitive adhesives are designed with a balance between flow and resistance to flow. The bond forms because the adhesive is soft enough to flow the adherend. The bond has strength because the adhesive is hard enough to resist flow when stress is applied to the bond. Since these adhesives are not true solids, the strength of pressure sensitive adhesives decreases when the temperature is increased. PSAs also exhibit a tendency to undergo creep when subjected to loads.

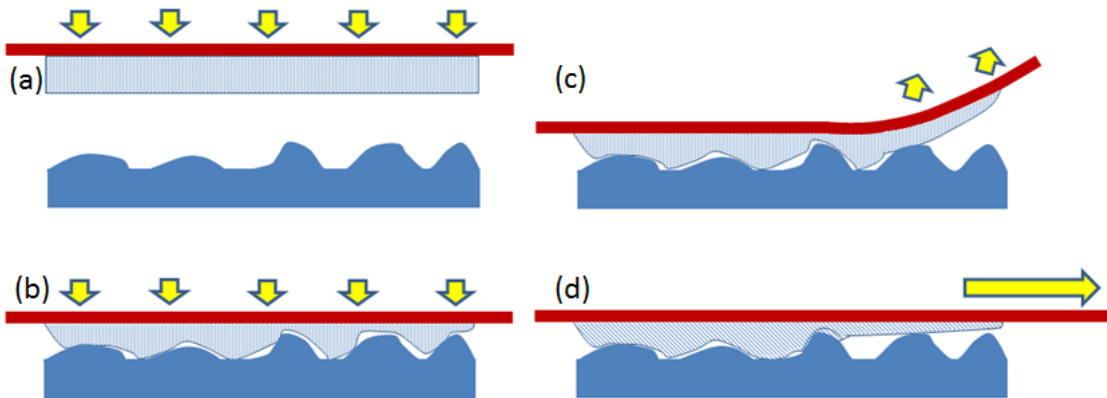


Figure 2.2 Mechanism of PSA. For figure (a)-(d), red layer on the top represents the back of PSAs, the light blue layer in the middle represents the functional polymer adhesive layer, and the dark blue layer underneath is the adherend. (a) Before contacting with adherend, the polymer adhesive layer is undeformed. (b) Adhesive layer deformed to occupy the space among the asperities of the adherend. Larger applied pressure will cause more intimate contact with adherend, and the bonding strength is enhanced. (c) Due to

the high normal and shear adhesion strength, Peeling is the easiest way to release PSA from adherend. (d) A novel PSA can be released by stretching. Horizontal elongation of adhesive layer suspends the adhesion layer from the adherend.

2.2 Gecko-Inspired Dry Adhesives

Gecko has remarkable ability to climb wall, and attach/detach easily. The adhesive strategy of the gecko relies on foot pads composed of specialized keratinous foot-hairs called seta [1-5], which are subdivided into terminal spatulae of approximately 200 nm. Millions of the microfibers on the toe form a self-cleaning dry adhesive. The adhesive force measurement of single gecko seta was firstly performed by Autumn and co-workers [1, 3]. Autumn and co-workers [3] also demonstrate the gecko's amazing climbing ability is contributed by the weak molecular attractive forces, named van der Waals forces. The detail discussion of the mechanism is reviewed in the section 2.2.1. In order to mimic gecko's setae structure, many researchers made their effort to synthetic gecko adhesives [16-31], the list of synthesis methodologies can be found in Table 2.1. Polymer fibrous array, carbon nanotube array and directed self-assembly fibers are three major categories of gecko inspired adhesives, which will be review in the section 2.2.2. Our electrospun polymer fibers are also one approach to synthetic gecko-like dry adhesives.

2.2.1 Mechanism of Gecko Adhesive

First direct measurement of single seta force is reported by Autumn and co-workers [3]. They hypothesized the seta is operated by van der Waals forces, and

supported the hypothesis by experimental adhesion value. Gecko seta is soft, and then is able to deform sufficiently for intimate contact with surface. Intimate contact enables van der Waals attractive forces between seta and contacted surface. Because of the small size and large amount of seta, a relatively large contact area is achieved, and sufficient van der Waals forces are provided.

More evidence of van der Waals adhesion in gecko seta is accomplished by Autumn and co-workers [3, 32-36]. Capillary force contributes to adhesion in many insects. But for gecko, Autumn and co-workers [3, 32] made effort to prove van der Waals adhesion is the primary mechanism of adhesion. Van der Waals mechanism implies the adhesion force is not strongly affected by surface chemistry. Van der Waals adhesion depends on the size and the shape of the seta. In order to prove the existence of van der Waals, gecko adhesive tests are performed on two polarizable semi-conductor surfaces which are strongly hydrophobic and hydrophilic representatively. If the adhesion mechanism is capillary adhesion, predicted adhesion strength of hydrophilic surface will be significantly larger than the adhesion strength of hydrophobic surface. However, under van der Waals adhesion mechanism, the adhesion strength will have no significant difference between hydrophilic and hydrophobic surface. Adhesion force between gecko seta and SiO₂ wafer, which is a highly hydrophilic surface, is 0.218 ± 0.008 N/mm². And adhesion force between gecko seta and GaAs wafer, which is a highly hydrophobic surface, is 0.213 ± 0.007 N/mm². The experimental results show no significant difference between the two adhesion forces, and van der Waals adhesion is supported by the results.

The van der Waals force of round end contact with surface can be theoretically estimated by [3]:

$$F_{vdw} = HR/6d_0^2 \quad \text{Equation 2.1}$$

where d_0 is the cutoff distance, H is the Hamaker constant, and R is the tip radius.

The geometrical adhesion theories predict adhesion force by Johnson-Kendall-Roberts model can be calculated by:

$$F = 3/2\pi RW \quad \text{Equation 2.2}$$

where $W = \sqrt{\gamma_1\gamma_2}$, and γ_1, γ_2 are the surface energies of two contact materials. By predicting adhesion force from two different approaches, F_{vdw} contribute 47-63% of total the adhesion force. Therefore mechanism of van der Waals adhesion is verified.

2.2.2 Types of Gecko-Inspired Adhesives

In previous section, the van der Waals force is inversely proportional to the square of the distance between two surfaces. Based on adhesion mechanism of gecko foot hair, attempts are made by researchers to develop gecko-inspired dry adhesives, which are proposal to be high bonding strength, easy-detachable and self-cleaning etc. Benefiting from micro-fabrication technology, fibrillar structure can be fabricated in the similar size as gecko's hierarchical structure [36-39].

Polymer Fibrous Arrays

One of the simplest approaches is to mold liquid polymer by using of a master template to create fibrillar structure. Sitti and co-workers [40] made effort to create a set of dimples on a wax surface by using of AFM tips. These dimples were worked as a mold to fabricate polymer micro pillars. Adhesion measurement results showed a large adhesion force for each pillar. But the whole structure failed to show adhesion in a macro-scale. The reason was explained by lack of flexibility in the pillars.

The technologies of lithography and etching were employed by Geim and co-workers [25] to create polyimide nanofibers array. Eletron-beam lithography, thermal evaporation is adopted to prepare an array of nano-scale aluminum disks. These patterns were transferred to a polyimide film by dry etching to create polyimide nanohairs, as shown in Figure 2.3. 1 cm² sample was tested, and the adhesion force in ~3N, which is 1/3 the adhesive strength of a gecko. However, bunching of the nanohairs exists, as shown in Figure 2.3. Polymer nanohairs are lack of self-support ability. Bunching happens after using for times. Bunching would significantly reduce adhesion strength and reusability. Angled microfiber arrays were created by researchers using photolithography technology [26-27, 38]. Aksak and co-workers [26] reported that angled fibers array exhibited lower adhesion compared with similar vertical fibers array, because of a peeling moment. However, in biological attachment systems, angled fibers are preferred.

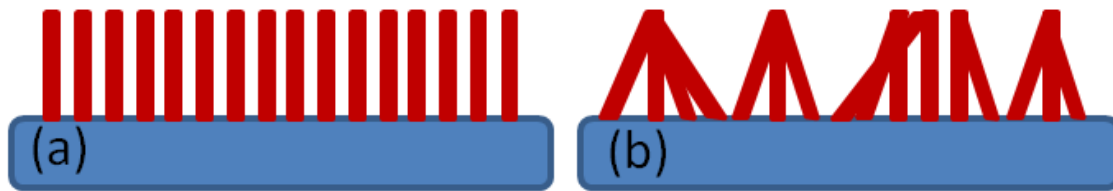


Figure 2.3 A schematic to present the bunching issue of nanohairs (a) An array of polyimide nanohairs and (b) due to the lack of self-support ability, bunching of the nanohairs happened after testing, leads to a reduction in adhesive force.

Carbon Nanotube Arrays

Yurdumakan and co-workers [41] grew vertical aligned multi-walled carbon nanotubes (MWCNT) by using of chemical vapor deposition (CVD). The vertical MWCNT are 50-100 μm in length as shown in Figure 2.4(a). The sample with MWCNT was then dipped in to methyl methacrylate solution. Poly (methyl methacrylate) (PMMA) - MWCNT is formed after polymerization. The PMMA-MWCNT sheets were peeled off from silicon substrate, as shown in Figure 2.4(b). The PMMA-MWCNT sheets can achieve adhesion forces two orders of magnitude greater than gecko foot hairs on the nano-scale. Ge and co-workers [29] had fabricated vertically aligned MWCNT arrays on polymer tape. They reported adhesion strength is also high on macro-scale. Qu and co-workers [22, 23] reported high adhesion on nano-scale by testing adhesion on vertical aligned MWCNT array on silicon substrate.

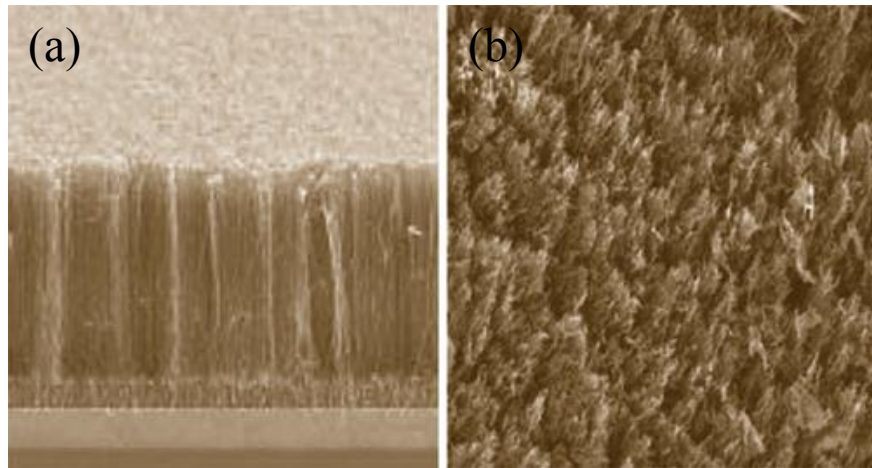


Figure 2.4 Multiwall carbon nanotube structures: (a) grown on silicon by chemical vapor deposition, (b) transferred into a PMMA matrix and then exposed on the surface after solvent etching [41].

Directed Self-Assembly Fibers

Sitti and co-workers [30-31] proposed a method of directed self-assembly to produce aligned fibers. A thin liquid polymer film was coated on a conductive substrate. The other paralleled conductive plate was used to apply a DC electric field to the bottom substrate. Static electrical force will drive liquid polymer to grow up until they reach the upper plate. Then aligned pillars will be formed spontaneously. The methodology is shown in Figure 2.5. Similarly, electrospinning is another electrical powered fiber fabrication technology, and is a potential low-cost technology to fabricated gecko-inspired adhesives.

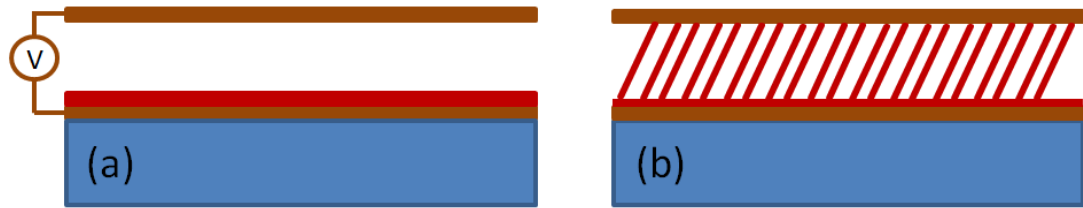


Figure 2.5 Directed self-assembly-based method of producing high-aspect-ratio micro/nanofibers. (a) A layer of polymer solution (in red) lays upon a conductive plate (in yellow), and a voltage is applied to two parallel plates (in yellow). (b) aligned pillars are formed between parallel plates.

In summary, researchers show great interest in creating gecko-inspired adhesives. Nano-indentation, lithography, MWCNT arrays and self-assembly are some of the major methods used to create fibrillar structures. During the fibrillar structure design, the fibers need to be compliant enough to deform easily to make intimate contact with surface's roughness profile, and also need to be rigid enough not to collapse easily. Also the space between fibers needs to be considered well during structure design. Small spacing will lead to bunching, which will decrease adhesion strength dramatically, and also adhesion strength will not be sufficient if spacing is too large.

Table 2.1 Existing fibrous dry adhesives fabrication technology

Materials	Fabrication technology	Remarkable achievement	Issues	Investigators and References
HDPE/PE	Molding PE film into a filter, Etching filter to free the fibers	Repeated-use for 300 cycles	Repeatability still low, below gecko feet's 30000 cycles	Gilles et al. [16]
Polypropylene	Same as above	Stiff fibers, self-cleaning	Did not self-clean larger particles	Lee et al. [17-19]
PUA	Replica molding with an UV-curable polymer and angled etching of polySi substrate	Hierarchical structure	N/A	Jeong et al. [20-21]
Carbon nanotubes	Low pressure CVD on wafer	10 times the adhesion force of gecko feet	N/A	Qu et al.[22-23]
PGSA	Nanomolding, and surface modification	Biocompatible and biodegradable	N/A	Mahdavi, et al. [24]
Polyimide on Scotch tape	Electron-beam lithography	Successfully mimic gecko feet hair, carrying capacity >100 g	Stick to each other, durability is poor	Geim et al. [25]
SU-8 photoresist	Lithography	Directional adhesion	Resolution is low, fiber size is large	Sitti et al.[26-27]
PMMA	Stretching of a polymer film	Cost-effective	N/A	Jeong et al [28]
Carbon Nanotubes	Photolithography, catalyst deposition, and a chemical vapor deposition process.	Dry conductive reversible adhesive, hierarchical structures	N/A	Ge et al. [29]
Polystyrene	Stretch by static electrical force	Low cost, scalable	Can't mimic gecko feet effectively	Sitti et al.[30-31]

2.3 Mechanism of Adhesion

The tendency of dissimilar particles or surfaces to cling to one another is named adhesion. Generally, five mechanisms of adhesion have been proposed to explain the adhesion: physical adsorption, diffusion, electrostatic, mechanical interlocking and weak boundary layer theories [42]. However, no single theory explains adhesion in a general and comprehensive way. As all adhesive bonds involve molecules in intimate contact, physical adsorption must always contribute first. Physical adsorption plays a dominant role in gecko-inspired adhesives, namely van-der Waals dispersive force, as mentioned in section 2.2. Acid-base interaction is a kind of physical adsorption, which is the dominant mechanism of pressure sensitive adhesives. Mechanical interlocking is observed when liquid adhesives are applied. The liquid adhesives can fill the voids or pores of the adherends, and hold the adherends together by mechanical interlocking. When both materials are soluble into each other, diffusion adhesion theory possesses the primary mechanism. Electrostatic adhesion happens mostly between conductive materials. Weak boundary theory explained the reason of weak adhesion between adherends.

2.3.1 Physical Adsorption

The physical adsorption theory states that adhesion results from intimate intermolecular contact between two materials, and involves surface forces that develop between the atoms in the two surfaces. This theory is believed to be one of the most important mechanisms in achieving adhesion [43]. The most common surface force that forms at the adhesive-adherend interface is the van der Waals force. In addition, acid-base interactions and hydrogen bonds, which are generally considered as a type of acid-

base interaction, may also contribute to intrinsic adhesion forces and have been studied in depth by Fowkes and co-workers [44-46]. Research conducted by many other investigators [47-49] experimentally demonstrated that the mechanism of adhesion in many adhesive joints only involves interfacial secondary forces. It has also been noted that the calculated attractive forces between two surfaces are considerably higher than the experimentally measured strength of adhesive joints. This discrepancy between theoretical and experimental strength values has been attributed to voids, defects or other geometric irregularities which may cause stress concentrations during loading [50].

To obtain good adsorption, intimate contact must be reached such that van der Waals interaction or the acid-base interaction or both could take place; hence good wetting is essential. According to Young's equation, the surface tensions (liquid/vapor γ_{lv} , solid/liquid γ_{sl} and solid/vapor γ_{sv}) at the three phase contact point are related to the equilibrium contact angle θ through:

$$\gamma_{sv} = \gamma_{sl} + \gamma_{lv} \cos \theta \quad \text{Equation 2.3}$$

Sharpe and Schonhorn [49] have proposed that one important factor that influences the adhesive joint strength is the adhesive's ability to spread spontaneously on the substrate when the joint is initially formed. For spontaneous wetting to occur,

$$\gamma_{sv} > \gamma_{sl} + \gamma_{lv} \quad \text{Equation 2.4}$$

By ignoring the interfacial free energy, Sharpe and Schonhorn have further proposed the following criteria:

For good wetting: $\gamma_{sv} > \gamma_{lv}$; for poor wetting: $\gamma_{sv} < \gamma_{lv}$

According to Fowkes [46], the total work of adhesion W_A is the sum of the van der Waals interaction W_A^{LW} and the acid-base interaction W_A^{a-b} , as:

$$W_A = W_A^{LW} + W_A^{a-b} \quad \text{Equation 2.5}$$

Fowkes also suggested that the van der Waals W_A^{LW} and the acid-base interactions W_A^{a-b} could be respectively expressed as follows:

$$W_A^{LW} \cong W_{12}^d = 2(\gamma_1^d \gamma_2^d)^{1/2} \quad \text{Equation 2.6}$$

and

$$W_A^{a-b} = -fn^{a-b} \Delta H^{a-b} \quad \text{Equation 2.7}$$

where, γ_1^d and γ_2^d are the dispersion force components of phases 1 and 2, respectively, f is an enthalpy-to-free-energy correction factor, n^{a-b} is the surface fraction of the acid-base pair per unit area, and ΔH^{a-b} is the enthalpy required for the formation of an acid-base pair.

2.3.2 Mechanical Interlocking

If a substrate has an irregular surface, then the adhesive may enter the irregularities prior to hardening. This simple idea gives the mechanical interlocking theory, which contributes to adhesive bonds with porous materials such as wood and textiles. However, the attainment of good adhesion between smooth adherend surfaces in many studies suggests that the interlocking may help promote adhesion, but is not an adhesion mechanism with general applicability. Clearfield and coworkers [47] reviewed

several common pretreatment methods applied on aluminum surfaces, such as the Forest Product Laboratory (FPL) etching procedure, phosphoric acid anodization (PAA) and chromic acid anodization (CAA). He summarized that these pretreatments result in micro-roughness on the adherend surface that can improve bond strength and durability by providing the mechanical interlocking. Other factors like formation of a larger surface, improved kinetics of wetting, and increased plastic deformation of the adhesive benefit the enhancement of adhesive joints strength as well [48].

Gent and co-workers [50] have done adhesion modeling research of mechanical interlocking. A flat surface containing deep cylindrical holes which the adhesive fills is considered as the rough substrate. Then the strands of adhesive are assumed to pull out of the holes. If the adhesives strands are stretched and pull out from the holes, the apparent work of adhesion (W) can be predicted by:

$$W = W_0 \left[1 + n\pi a^2 \left(\frac{4l}{a} - 1 \right) \right] \quad \text{Equation 2.8}$$

where W_0 is the characteristic work of adhesion, n is the numbers of the holes, l is the depth of the hole or the length of the adhesive strands, and a is the radius of the hole. For deep holes, with $l/a \gg 1$, the apparent work of adhesion W will be much greater than W_0 . It can easily exceed the work of fracture, and a cohesive failure will be expected. It is also notable, only work expended in stretching the strands is considered in the model, the work of adhesion in the overlayer is neglected, and therefore, the real work of adhesion may be larger than predicted by the model.

2.3.3 Diffusion

The diffusion theory takes the view that polymers in contact may inter-diffuse so that the initial boundary is eventually removed. Such inter-diffusion will occur only if the polymer chains are mobile (i.e. the temperature must be above the glass transition temperatures) and compatible. As most polymers, including those with very similar chemical structures such as polyethylene and polypropylene are incompatible, the theory is generally only applicable in bonding rubbery polymers, as might occur when surfaces coated with contact adhesives are pressed together, and in welding of thermoplastics, by the auto-adhesion process. Since Voyutskii [51] proposed the diffusion theory, several other related theories have been proposed to describe the self-diffusion phenomenon of polymers, including entanglement coupling, cooperativity, and reptation model.

2.3.4 Electrostatic Interactions

The electrostatic theory originated in the proposal that if two metals are placed in contact, electrons will be transferred from one to the other so forming an electrical double layer, which gives a force of attraction. As polymers are insulators, it seems difficult to apply this theory to adhesives.

Some controversies have arisen meanwhile. For example, Roberts [52] has indicated in his studies of rubber adhesion that the electrostatic component contributes less than 10%, usually 0.1-1% of the total adhesion. Possart [53] has also revealed that the energy required to peel the LDPE film from the aluminum foil is about 600 times that of the stored electrostatic energy due to the electrical double layer.

2.3.5 Weak Boundary Layer

The weak boundary layer theory, proposed by Bikerman [54-55], is that clean surfaces can give strong bonds to adhesives, but some contaminants such as rust and oils or greases give a layer which is cohesively weak. According to Bikerman, the true interfacial failure rarely occurs in the breaking of joint by purely mechanical means, and the main reason is the cohesive failure of the weak boundary layer. However not all contaminants will form weak boundary layers, as in some circumstances they will be dissolved by the adhesive, for instance, acrylic structural adhesives are superior to epoxides because of their ability to dissolve oils and greases [56].

2.4 Existing Models for Adhesive Contact

2.4.1 The Work of Adhesion

From classic thermodynamic prospects of view, the work of adhesion is used to describe the propensity of polymer adhesion by the concept of surface energy. The work of adhesion, W , is defined as the energy change per unit area due to the creation of a new interface, and the elimination of two bare surfaces, as expressed below. The work of adhesion distinguished two states, the contact and separation.

$$W = \gamma_1 + \gamma_2 - \gamma_{12} \quad \text{Equation 2.9}$$

where γ_1 and γ_2 are the surface energies of the two bare surface, γ_{12} is the interfacial energy. If the the surface are the same materials, which means: $\gamma_1 = \gamma_2$, and $\gamma_{12} = 0$, then W is called the work of cohesion.

When two smooth polymer surfaces contact intimately with each other, within a few nanometer distance, intermolecular attractive interactions dominate the work of adhesion [57-58] The van der Waals dispersive force is the major intermolecular interactions. Other types of intermolecular interactions include polar interactions, hydrogen bonding, acid-base interactions etc. If other types of intermolecular interactions can be neglected, the work of adhesion could be estimated from the van der Waals forces [57],

$$W = \frac{A_{12}}{12\pi D_0^2} \quad \text{Equation 2.10}$$

where A_{12} is the Hamaker constant, which only depends on the surface chemistry of the materials. D_0 is the separation distance.

2.4.2 Adhesion Model for Adhesive Contact

The work of adhesion described adhesion properties from the aspect of thermodynamics. Theory of contact mechanics is another theory framework for adhesion research. Considering elastic adhesive contact specifically, contact mechanics has several widely cited mathematical models. An early model, Hertzian Theory, only considered the geometrical effects, contact adhesive interactions are totally neglected. Bradley model considered van der Waals interaction between two contact surface, and find the adhesive force from the Lennard-Jones potential. However, Bradley model has not considered materials properties yet. In order to incorporate adhesion effect into geometrical effect, Johnson, Kendall and Roberts developed the

JKR theory incorporating the Bradley model and Herizian model. As an alternative model, Derjaguin-Muller-Toporov (DMT) model [59-60] considers van der Waals attractive interactions outside the elastics contact regime, which is slightly different from JKR model. JKR considers adhesion force also from the elastic contact area. The comparisons among these models are shown in Figure 2.6.

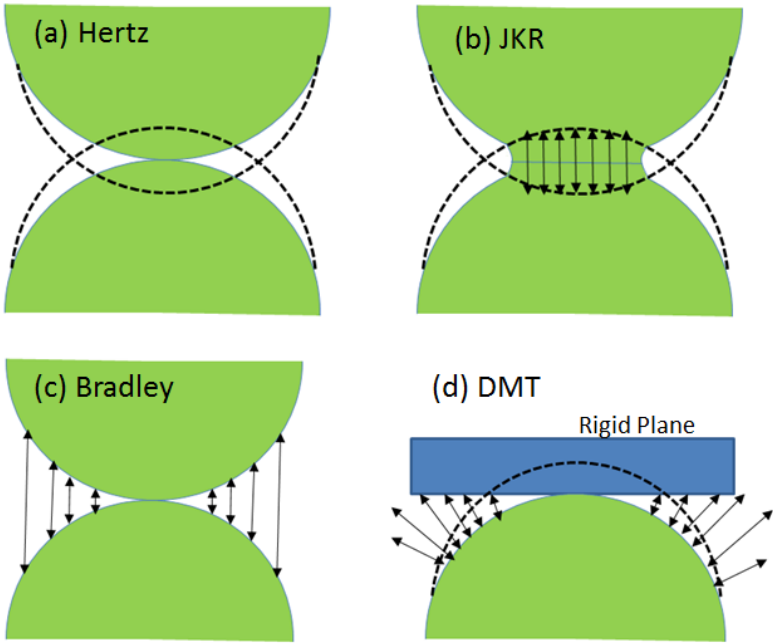


Figure 2.6 Contact Mechanical models, Hertz, JKR, Brandly and DMT.

Johnson-Kendall-Roberts (JKR) Theory

JKR theory [61] is the most widely cited theory to describe the adhesion behavior of polymeric elastomers. JKR theory incorporates the effect of adhesion in Hertzian contact, the effect of contact pressure and the effect of attractive force inside the area of contact. For an elastic sphere of radius R when pressed by a load L against a flat surface

of the same material of effective elastic modulus K and the work of adhesion W , there is a flat contact area of radius a given by [61]:

$$a = \sqrt[3]{\frac{R}{K} [L + 3\pi RW + \sqrt{6\pi RWL + (3\pi RW)^2}]} \quad \text{Equation 2.11}$$

The adhesion force, “pull-off” force, is given by:

$$F_{JKR} = \frac{3}{2}\pi RW \quad \text{Equation 2.12}$$

Extensive experimental study on JKR theory has been done by many researchers [62-64]. JKR theory has been proved to work well for “ideal” (clean, smooth and elastic) surfaces, and the value of surface energy γ can be predicted within an error of 10%.

Derjaguin-Muller-Toporov (DMT) Model

The Derjaguin-Muller-Toporov (DMT) model [59] is an alternative model for adhesive contact which assumes that the contact profile remains the same as in Hertzian contact but with additional attractive interactions outside the area of contact. The area of contact between two spheres is expressed by [60]:

$$a = \sqrt[3]{\frac{3R}{4K} [L + 4\pi RW]} \quad \text{Equation 2.13}$$

The adhesion force, “pull-off” force, is given by:

$$F_{DMT} = 4\pi RW \quad \text{Equation 2.14}$$

JKR model and DMT model dominate the world of contact mechanics. JKR model is always applied to elastic solids, and DMT model is good for stiff solids. The transition

between the two models was analysed by Tabor and Maugis [65-67]. Tabor's parameter μ is given by

$$\mu = \frac{R^{1/3}W^{2/3}}{(K^*)^{2/3}\epsilon} \quad \text{Equation 2.15}$$

where R is the contacting radius, W is the work of adhesion. K^* is the reduced modulus of the contacting solids, and $K^* = 1/[(1 - \nu_1^2)/K_1 + (1 - \nu_2^2)/K_2]$, where K_1 and K_2 are the elastic modulus of materials 1 and 2, ν_1 and ν_2 are the Poisson's ratios of materials 1 and 2. ϵ is the interatomic distance at the closest contact point. By using of Tabor's parameter, DMT is applicable for $\mu \leq 3$. That means DMT model will be favored by the comparatively high modulus materials.

2.5 Methods of Adhesion Measurement

Adhesion property of bulk materials can be tested in various ways. Adhesion testing techniques have been discussed by researchers frequently [68-70]. In this section, advantages and disadvantages of the most cited adhesion tests, pull-off test, indentation test, peel test and blister test, will be reviewed.

2.5.1 Direct Pull-Off Test

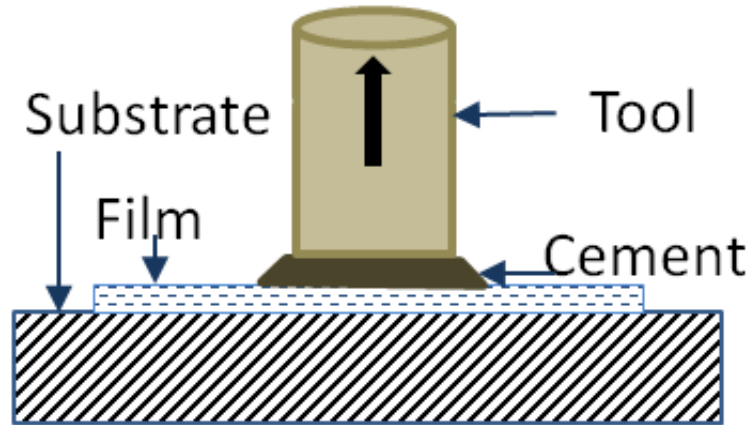


Figure 2.7 A schematic of direct pull-off test.

Pull-off test is the most direct way to determine the adhesion strength between film and substrate [71]. Figure 2.7 is a schematic of direct pull-off test. The tested film is adhered to rigid substrate, and film is glued to a pull tool by cement. The force required to detach the film is measured. Similar pull off tests can also be performed between sphere and plane or between cylinder and cylinder etc. If the contact is considered as an elastic contact, which means the deformation of the film during the test can be fully recovered, JKR model can be applied to analyze the work of adhesion.

However, pull-off testing results are highly dependent on the deformation of the tested film. Large and local applied force may cause non-uniform deformation of the film, and local plastic deformation becomes possible. The cohesive strength is also a concern if thin film is tested, local cohesion failure is easier to achieve than global adhesion failure.

2.5.2 Indentation Adhesion Test

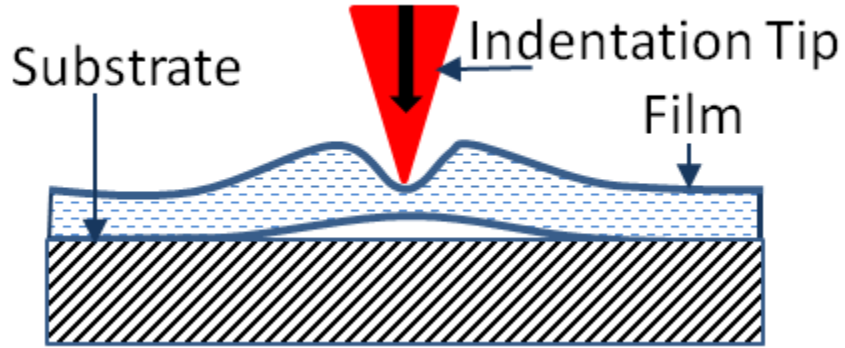


Figure 2.8 A schematic of indentation adhesion test

Indentation adhesion test always consists a rigid indentation tip, which is built from diamond or other high stiffness materials [72]. In most cases, the film is a layer of coating on substrate, and a high adhesion strength is expected. By applying a high force on the film via the tip, the film is expected to deform, and delaminate. The load and displacement data can be used to determine film's mechanical properties, like elastic modulus, hardness, fracture toughness etc. The mechanical energy release rate, which is the practical work of adhesion, can also be calculated based on the size of the delamination [73]. Macro scale test can be performed on a Rockwell hardness machine. Recent years micro-size indentation tests can be performed by using of nano-indenter or even atomic force microscopy [74]. Indentation test is a non-recoverable test, and the data obtained is only a local property.

2.5.3 Peel Test

Peel test is a widely used method to test the adhesion property for thin films or membranes. Peel test is a test method to pull a thin and flexible strip away from the substrate at some angle. Although the peel test offers simple test geometry for measuring bond fracture strength, it still suffers from several problems. Several studies [75-76] have shown the peel test is an accurate measurement method only under the condition, $\frac{6EP}{h\sigma_y^2} < 1$, where E is the elastic modulus, P is the peel force, h is the thickness and σ_y is the yield stress of the adhered film. For Cu films on polyimide substrate, this condition requires a Cu film thickness of ~ 1 cm, but the typical used Cu film is only $10 \mu\text{m}$ which is three orders of magnitude less [76]. For polyimide films on metal, this condition required several hundred microns in thickness, which is still much thicker than the films in industrial applications. Films would suffer far-field plastic deformation during testing, if this condition does not be satisfied, then the measurement of the work of adhesion would not be accurate. In spite of the weakness of the peel test, the ease of sample construction and test execution has contributed to its rapid spread.

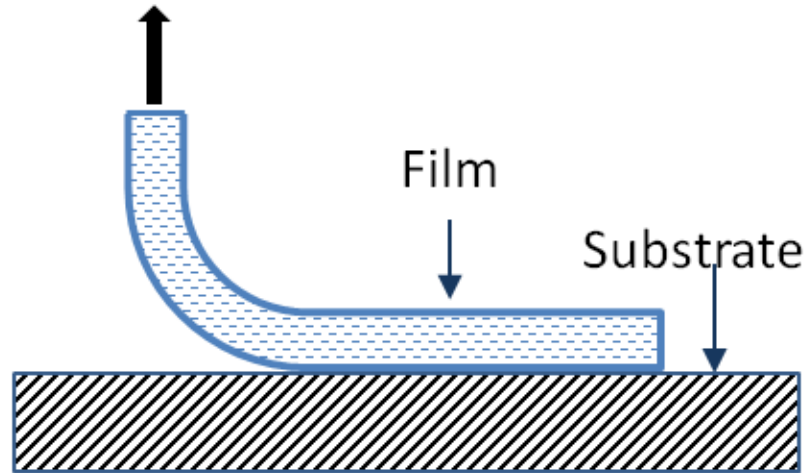


Figure 2.9 A schematic of peel test

2.5.4 Blister Test

The blister test requires no external tractions for debonding, and the peel angle is low relative to other methods. The stand blister test (SBT), as shown in Figure 2.10(a), was first introduced by Dannenberg [77] at 1961. In the standard blister test, either a liquid or gas is applied under pressure through a hole in the substrate, forcing the adhered membrane or coating to debond. The strain energy release rate can be calculated from the relationship between the pressure, blister radius, and blister height.

Many improvements and refinements have been made. Williams and co-workers [78-80] applied the concepts of continuum mechanics to the blister geometry to relate experimental variables, such as critical pressure to the work of adhesion. Hinkley [81] assumed that the shape of deformed membranes is a spherical cap, which can be described by membrane theory. His work is based on elasticity behavior of the membrane,

and the fracture criterion was derived from the way of energy balance. The shape of the inflated blister is described by Gent and co-workers [82].

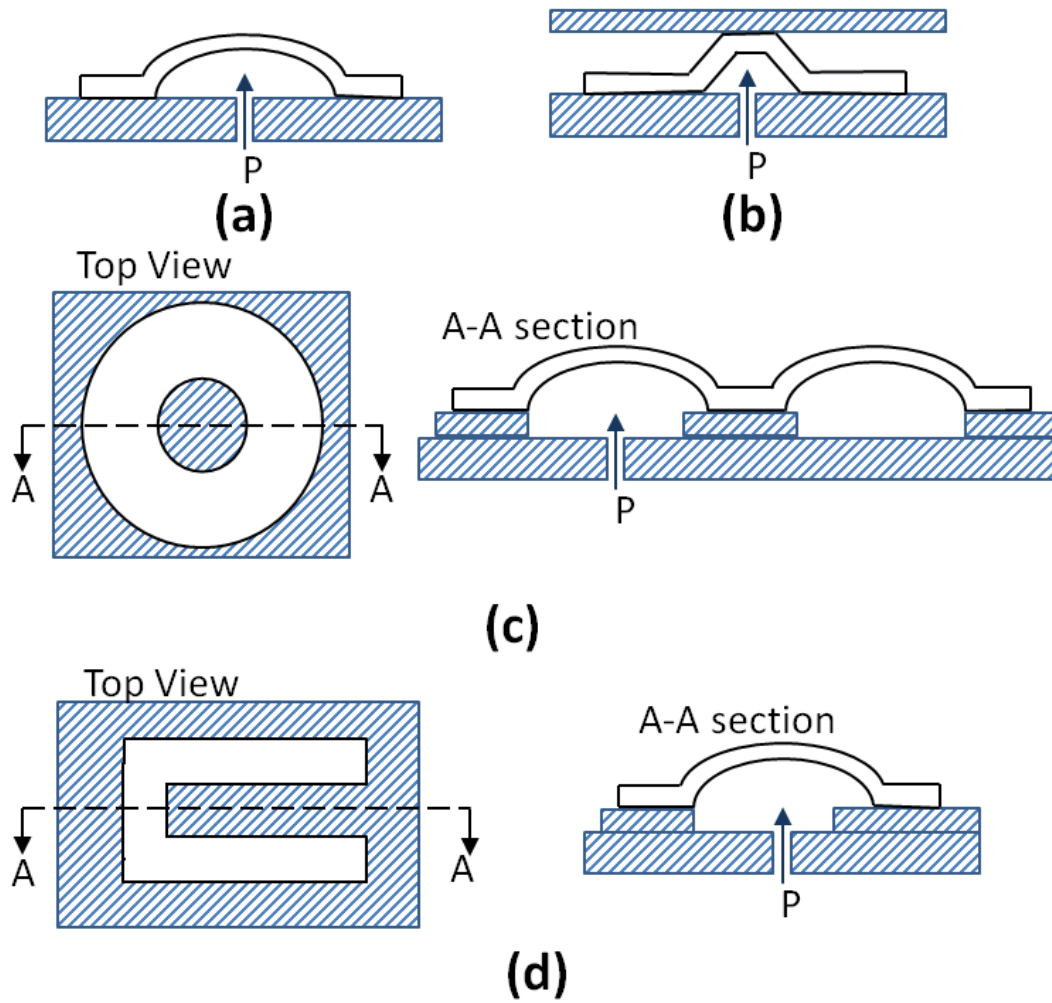


Figure 2.10 Schematics of the geometries of various blister tests: (a) standard blister test; (b) constrained blister test; (c) island blister test and (d) peninsula blister test.

Constrained blister test (CBT) has the similar geometry as SBT with a plate positioned parallel to the substrate in order to restrict the vertical deflection of the film, as shown in Figure 2.10 (b). Compared with SBT geometry, which has the maximum stress in the center of the blister [83], the CBT reduces the stress in the center to minimize the risk of film rupture before delamination. Rate effects and viscoelastic behavior in the vicinity of the crack tip is incorporated by Napolitano and co-workers [84]. Chang and co-workers [85] applied the CBT method to test a pressure-sensitive adhesive tape on polycarbonate system, and found the work of adhesion is dependent on the rate of the test. Lai and Dillard [86-88] evaluated the adhesion of a thick aluminum film by using elementary plate theory analytically, and finite element analysis is also performed numerically. Their results show the strain energy release rate remains constant as the debonding proceeds. Agreement between the two methods is also reached.

An island blister test [IBT] is suggested by Allen and Senturia [89-92], which applied to measure thin polymer films on metal or on polymer, as shown in Figure 2.10 (c). The advantages of the IBT include its ability to account for residual stress in the film, thin well-adhered films can be tested without tearing them, and less dissipative energy in the measurement compared with SBT or peel test.

Dillard and co-workers [93-94] developed the peninsula blister test (PBT) based on the IBT concept, which replaces the axisymmetric island with a peninsula, as shown in Figure 2.10 (d). Addition to the advantages of the IBT, PBT offers even lower stresses at the crack tip during debonding, and a constant strain energy release rate. Dillard and Bao [94] demonstrated the PBT is the most efficient blister test followed by the IBT and the

SBT, based on a normalized bond dimension and a normalized strain energy release rate. For a given materials system, the PBT stresses the file least during debonding. This merit is particularly important for ductile, well-adhered system. However the PBT has a peninsula geometry which renders modeling more difficult than axisymmetric system. Liechiti and co-workers [95] suggests gross plasticity in the adhered film is difficult to avoid in the case of copper films delaminating from polyimide adherends, even in the PBT. Their effort focused on attempting to define an optimal geometry to minimize dissipative effects, assuming adhesion energy of 100 J/m^2 .

2.6 Electrospinning Technology

Electrospinning has been recognized as an efficient technique for the fabrication of polymer nanofibers. Electrospinning is a simple technique, which uses high static voltage to electrically charge the polymer solution for producing ultra-fine fibers [96]. It has more advantages over the conventional spinning method, such as a simple apparatus, the flexibility in material selection. In addition, the unique properties of electrospun nanofibers make them attractive for a number of applications, including filtration, composite reinforcement and tissue engineering, etc.

An electrospinning station essentially consists of a syringe filled with polymer solutions. High voltage source and a grounded conductive collector screen. A custom made electrospinning station is shown in Figure 2.11 (a). In addition, a metering syringe pump can be used to control the flow rate of the polymer solution. The needle of the syringe typically serves as an electrode to electrically charge the polymer solution and the

counter-electrode is connected to the conductive collector screen. The types of collector could be different, in order to meet different fiber collection requirement. Figure 2.11 (b) shows a SEM image of electrospun nonwoven, which consists random arranged ultra-fine fibers. Rotating drum collector, rotation disk collector, static parallel collector are the most widely used collector to collect aligned fibers.

Electrospinning fibers display different crystal structures compare to bulk materials. During the fiber formation process, a fraction of the chains crystallizes to form lamellae consisting of small crystals and the remaining fraction forms the amorphous phase [97-99]. Due to the shear forces experienced by the jet during electrospinning, the chain orientation aligns along the fiber axis [100], as shown in Figure 2.12.

Both the shape and the morphology of electrospun fibers are important to the end-use applications. Fibers with circular cross sections have most commonly been observed in electrospinning process. Besides, a variety of cross-sectional shapes have been reported, such as branched fibers, flat ribbons, ribbons with other cross-section shapes [101-102]. In addition, fibers with wrinkled or porous surfaces were reported by researchers [103]. The observation of these different cross-sectional shapes from electrospun fibers indicates that fluid mechanical effects, electrical charge within the jet, evaporation of the solvent and the experimental environment all contributes to the formation of the fibers [104-106].

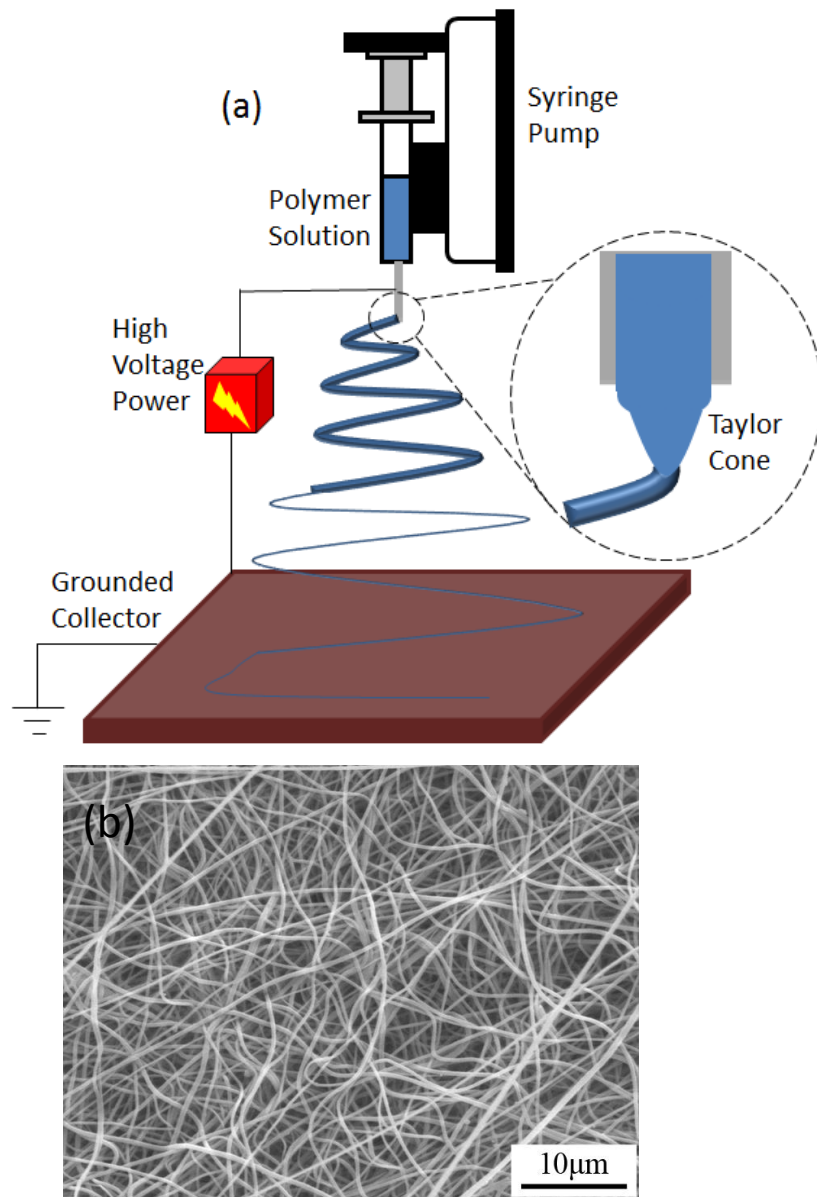


Figure 2. 11 (a) A schematic of electrospinning station; (b) polymer nonwoven produced by electrospinning.

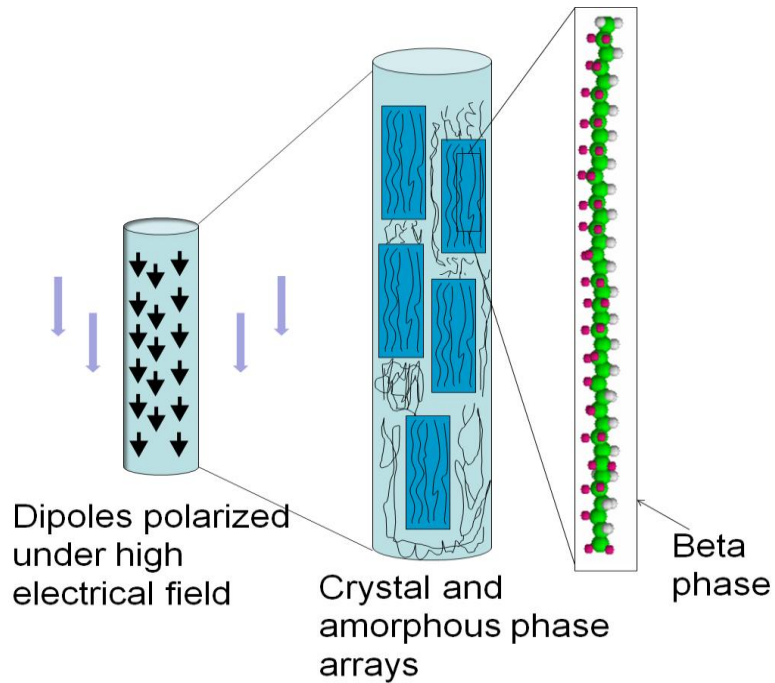


Figure 2.12 A schematic representation of the orientation of molecular chain inside the PVDF electrospun fiber, and also the conformation of the helical structure of the chain.

The extreme elongation of electrospinning liquid jets contributes to this structure characterization of the electrospun fibers. During the electrospinning process, polymer fluid jet experiences a high ratio of stretching (the draw rate is over 106/s), which leads to the alignment of polymer molecules along the fiber axis and a high degree of molecular orientations [100]. The chain orientation could be analyzed by Transmission electron microscopy (TEM), Raman spectroscopy and X-ray diffraction analysis [107]. For semi-crystalline polymers, solidification also impacts the formation of crystals. In the electrospinning process, the solvent evaporates much faster, which leads to the rapid solidification of electrospinning jet and results in the imperfect crystallites in electrospun fibers [108].

Many researchers made effort on controlling the fiber diameter and the morphology of the fibers by controlling the electrospinning parameters [109-111]. Major factors that control the diameter of the fibers are: (1) concentration of polymer in the solution, (2) type of solvent used, (3) conductivity of the solution, and (4) feeding rate of the solution.

2.6.1 Key Parameters of electrospinning

There are a number of factors, which affect the production of electrospun fibers during the electrospinning process: (a) The polymer solution properties, such as viscosity, elasticity, conductivity, and surface tension; (b) The process parameters, such as the gap distance between the capillary tip and the collector, applied voltage, and hydrostatic pressure in the solution container; and (c) The Environmental effects, such as temperature, humidity, and air flow.

Solution Concentration

The formation of electrospun fibers is primarily based on the viscosity and surface tension of the polymer solution. Different polymers require different solution concentrations to be electrospun. For example, it was found that the suitable solution for electrospinning of aqueous polyethylene oxide dissolved in the solvent mixture (ethanol and water) had the viscosity in the range, 1-20 poises, and surface tension between 35 and 55 dynes/cm [112]. At viscosities above 20 poises, electrospinning was not possible because of the instability of flow caused by the high cohesiveness of the solution.

Droplets were formed when the viscosity was too low (<1 poise). One of the most important parameters in electrospinning is the fiber diameter. A higher solution viscosity (higher solution concentration) results in a larger fiber diameter [112-114].

Another problem encountered in electrospinning is the formation of defects such as beads and pores, which may occur in polymer electrospun fibers. It has been found that the polymer concentration also affects the formation of the beads. Fong [115] recognized that higher polymer concentration resulted in fewer beads. At higher concentration, the bead diameter, if any, was larger. The shape of the beads changed from spherical to spindle like, when the polymer concentration varied from low to high levels [116].

Conductivity

The charge ions in the polymer solution greatly influence fiber formation. As the charges carried by the jet increase, higher elongation forces are imposed to the jet under the electrical field, resulting in smaller bead and thinner fiber diameters. Zong and co-workers [117] reported that with 1 wt% salt addition in biodegradable poly-l-lactic acid polymer solution, the resulting nanofibers were bead-free, with relatively smaller diameters in the range of 200-1000 nm.

Evaporation of Solvent

Solvent vapor pressure plays an important role in evaporation rate, drying time, and the morphology of electrospun fibers. Bognitzki and co-workers [116] used highly volatile solvents to produce PLLA fibers and obtained electrospun fibers with pore sizes

of 100 nm in width and 250 nm in length along the fiber axis. Lee and co-workers [118] studied the effect of volume ratio of the solvent on the fiber diameter and morphology of PVC fibers. They found that as the amount of DMF in the THF/DMF mixed solvent increased, the average fiber diameter decreased.

Applied Voltage

In electrospinning, the applied electrical voltage affects the jet stability and the fiber morphology to a remarkable degree. In general, an increase in the applied voltage causes high deposition rate due to large amount of mass flow from the needle tip. For the polyethylene oxide-water system, it was observed that the fiber morphology changed from a defect free fiber at an electrical potential of 5.5 kV to a highly beaded structure at 9.0 kV [119]. Megelski and co-workers [120] determined the dependence of the fiber diameter of polystyrene fibers on voltage, and showed that the fiber size decreased more or less from 20 mm to 10 mm without a dramatic change in the pore size distribution when the voltage was increased from 5 kV to 12 kV.

Capillary Tip–Collector Distance

The gap distance between the capillary tip and the collector influences the fiber deposition time, the evaporation rate, and the whipping or instability interval, which subsequently affect the fiber characteristics. An aqueous polymer solution needs longer gap distance for drying than a system that uses highly volatile solvent. Megelski and co-workers [120] showed that beaded polystyrene fibers with ribbon shaped morphology were produced upon decreasing the nozzle to collector distance. They also demonstrated

that shorter nozzle-collector distance yielded wet and beaded fibers, while the morphology changed from round to flat shape.

Flow Rate

Megelski and co-workers [120] found that the flow rate of polymer solution affects the jet velocity and the material transfer rate with enhanced pore and fiber sizes and beaded structures, as well with an increase in the polymer flow rate in case of polystyrene fibers.

2.7 Polyvinylidene fluoride (PVDF)

PVDF is a specialty plastic material in the fluoropolymer family; it is used generally in applications requiring the highest purity, strength, and resistance to solvents, acids, bases and heat and low smoke generation during a fire event. Compared to other fluoropolymers, it has an easier melt process because of its relatively low melting point of around 177 °C [121].

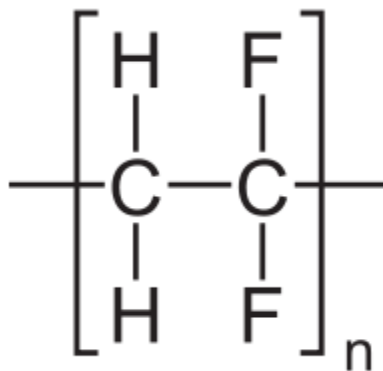


Figure 2.13 Repeat unite of polyvinylidene fluoride

Electrospinning of PVDF is widely studied by researchers [122-124]. Current research is mainly focused on controlling these internal parameters, as these represent the most important factors for determining the physical properties of the electrospun fibers and their membranes [125-126]. A systematic parameter study has been reported by Costa and co-workers [122]. The solvents used to dissolve PVDF were N,N-dimethylformamide (DMF) and acetone. Solutions were prepared at different concentrations. Yee and co-workers [127] studied the influence of PVDF solution concentration on fiber morphology. The ratio of mixture DMF and acetone was selected at 3:1 v/v, because they produce thinner and more homogeneous nanofibers in the electrospinning process. The lowest concentration of 5 wt% PVDF could not form stable electrospinning, beads of PVDF are formed due to the electrospay. Fibers can be successful electrospun by the solution from 7-15 wt%, and the average fiber diameter increases with the concentration of PVDF increase.

The PVDF is known as piezoelectric materials and it is well-known that proper mechanical stretching and electrical poling are necessary to achieve good piezoelectricity. Electrospinning processes can construct PVDF fibers with simultaneous in situ mechanical stretch and electrical poling [127-130]. A direct-write electrospinning technique by means of near-field electrospinning (NFES) [131-132] has been developed to produce orientation controllable depositions of piezoelectric PVDF fibers.

Chang and co-workers [133] studied crystal structure of PVDF electrospun fibers besides of physical properties, including surface morphology, average fiber diameter,

pore size etc. From X-ray diffraction and FT-Raman data, the PVdF membranes were found to have mixed-crystal structure of Form II (β -type) and Form III (γ -type).

Figure 2.14 shows the X-ray diffraction (XRD) patterns of the PVdF raw material, the electrospun PVdF membrane, and the resulting polymer electrolyte in 1 M LiPF₆-EC/DMC/DEC (1/1/1). It is well-known that PVdF adopts one of the following three crystalline structures, depending on the preparation conditions: Form I (α -type crystal with planar zigzag conformation, orthorhombic), Form II (β -type crystal with TGTG , monoclinic), and Form III (γ -type crystal with TTTGTTTG , Monoclinic) [134-135]. The PVdF raw material and the electrospun PVdF membrane have similar crystal structures, including two major peaks around 18 and 21°, and three minor peaks around 27, 36, and 57°. Most of the peaks are observed for all three crystalline forms of PVdF, whereas the peak at 27° is observed only for PVdF of Form II (β -type).

FT-Raman spectra of the PVdF raw material and the resulting electrospun membrane are shown in Figure 2.15. In the FT-Raman spectrum, most of the bands corresponded to the Form II (β -type), whereas others were not assignable to this crystal structure. In particular, the weak bands at 490 and 1273 cm⁻¹ corresponded to Form I and Form III, whereas the band at 839 cm⁻¹ corresponded to Form III [136-137] On the basis of these findings, it is suggested that the electrospun PVdF membrane is a mixed-crystal structure comprising both Form II (β -type) and Form III (γ -type), with Form III (γ -type) possibly being enhanced during either the preparation of the polymer solution or electrospinning.

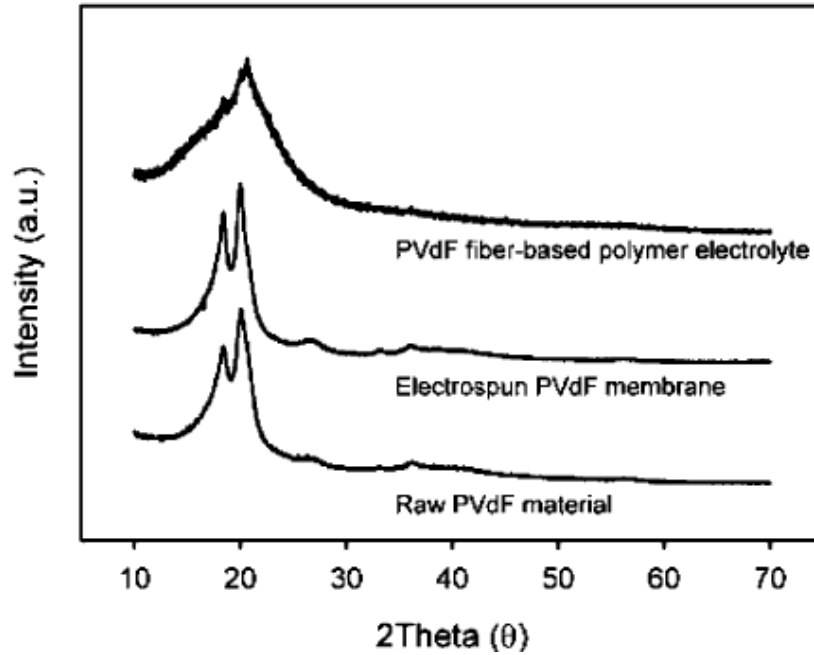


Figure 2.14 XRD spectra for the raw PVdF material, and the corresponding electrospun PVdF membrane and PVdF fiber-based polymer electrolyte [135].

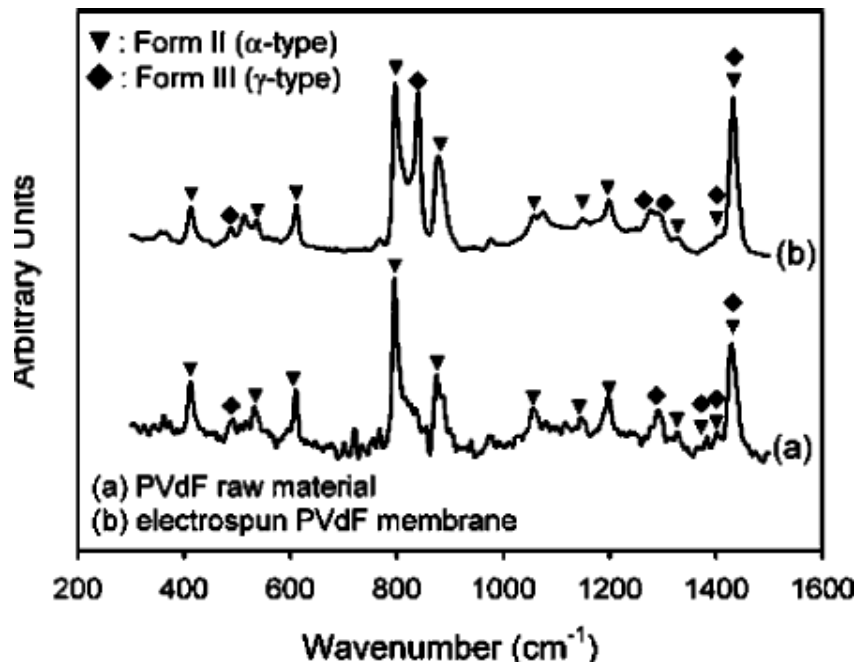


Figure 2.15 FT-Raman spectra for the raw PVdF material, and the corresponding electrospun PVdF membrane [135].

2.8 Polycaprolactone (PCL)

Polycaprolactone (PCL) [138] is a biodegradable polyester with a low melting point of around 60°C and a glass transition temperature of about -60°C. The most common use of polycaprolactone is in the manufacture of speciality polyurethanes. Polycaprolactones impart good water, oil, solvent and chlorine resistance to the polyurethane produced.

PCL is degraded by hydrolysis of its ester linkages in physiological conditions (such as in the human body) and has therefore received a great deal of attention for use as an implantable biomaterial. In particular it is especially interesting for the preparation of long term implantable devices, owing to its degradation which is even slower than that of polylactide.

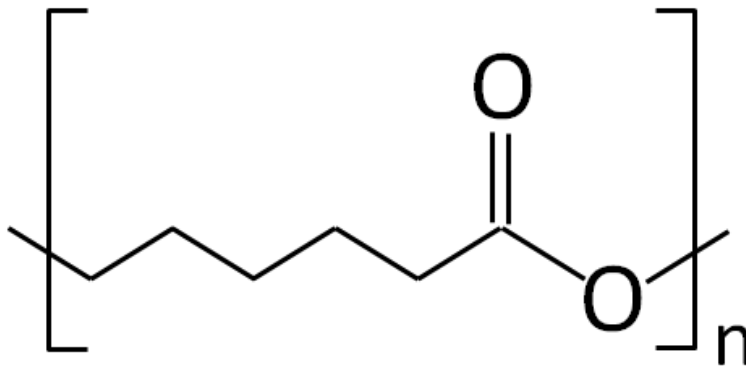


Figure 2.16 Repeat unit of PCL

Electrospinning of PCL is well studied by researchers. Electrospinning of PCL is governed by polymer solution properties, process parameters and ambient conditions and these parameters and effects on the morphology are widely recognized within the electrospinning literature [139-141].

Kim and co-workers [142] reported the water contact angle (WCA) of randomly deposited and uniaxially oriented PCL web structures has difference. As shown in Figure 2.17, the WCA for the uniaxially aligned PCL fibers was compared to that of the randomly distributed PCL fiber mat (129° after 5 min). The WCA of the PCL web aligned in the direction of the moving collector was 78° after 5 min. The WCA of the uniaxially aligned PCL web was smaller than that of the pure PCL web, indicating that the hydrophilicity of the structured mats was improved by the alignment of spun fibers.

Morphology of electrospun PCL fibers is systemically studied by Lee and co-workers [143], as dissolved in three types of solvent. One is methylene chloride (MC) only, and the second is mixing solvent with MC/DMF ratios of 100/0, 85/15, 75/25, and 40/60 (v/v), the third is mixing solvent having MC/toluene ratios of 85/15 and 40/60 (v/v). PCL solutions were prepared with concentration ranging from 10 to 15 wt% using each three type of solvent. For the MC/DMF systems, as increasing DMF volume fraction, spinning was dramatically enhanced and splaying and splitting observed. Also the diameter of electrospun PCL fibers decreased conspicuously.

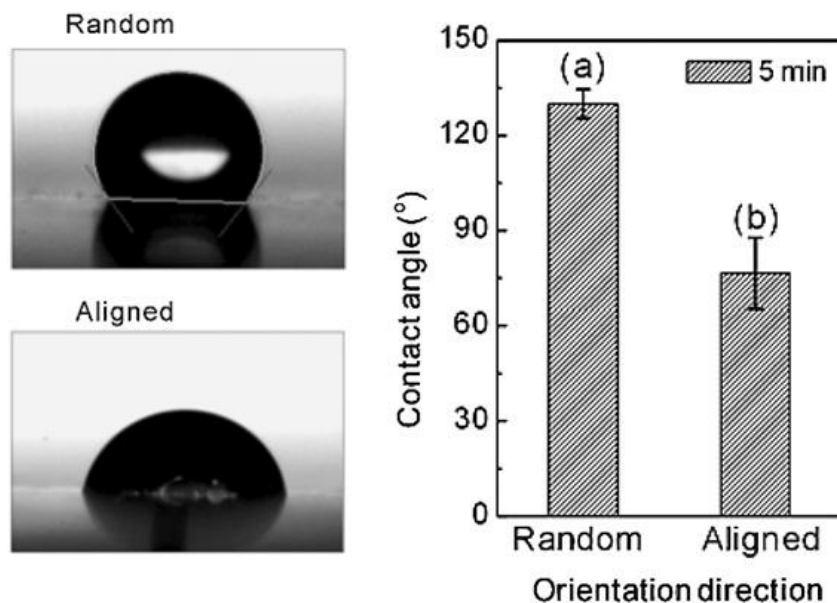


Figure 2.17 WCAs of (a) random and (b) uniaxially aligned PCL webs. Comparison of WCA measurements taken at 5 min for two differently oriented fiber mats [142].

To analyze the effect of fiber diameter on the mechanical properties, Wong and co-workers [144] tried to use two linear arrayed electrodes to collect single fiber, and then move to cardboard. Only one fiber is kept, all others will be trimmed under microscope. Figure 2.18 shows some representative stress–strain curves obtained from single fiber testing using the nanoforce tensile tester.

Figure 2.19 and Figure 2.20 are derived from the stress–strain curves produced by the sensitive nanoforce tensile tester. The modulus and strength of the fibers increase as the fiber diameter decreases. However, an abrupt change in tensile modulus and strength can be clearly seen in the proximity of ~ 700 nm in diameter. The abrupt shift in tensile properties was conjectured to arise from enhanced orderliness of the amorphous phase and crystalline morphology, or the presence of supramolecular structures. The fiber

diameter at which the abrupt shift in tensile properties occurs should be a characteristic of molecules examined.

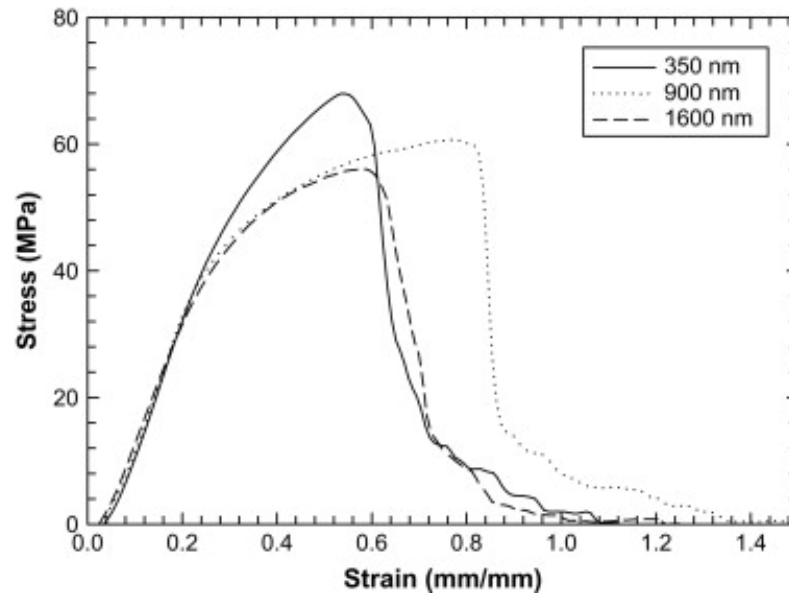


Figure 2.18 Representative stress–strain curves of single fibers obtained from tensile tests. Fibers with small diameters are seen to have higher modulus and strength [144].

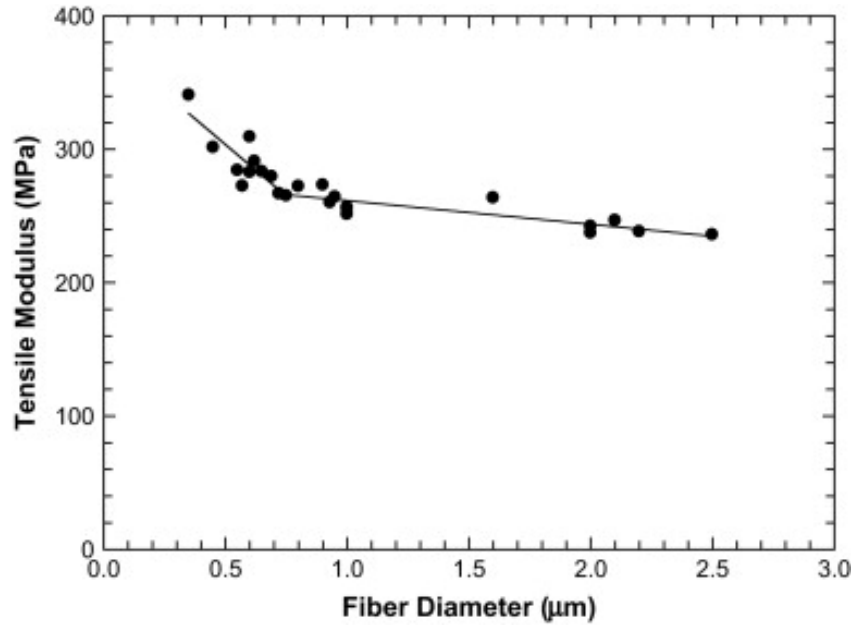


Figure 2.19 Plot of tensile modulus vs. fiber diameter. Tensile modulus increases with a decrease in fiber diameter [144].

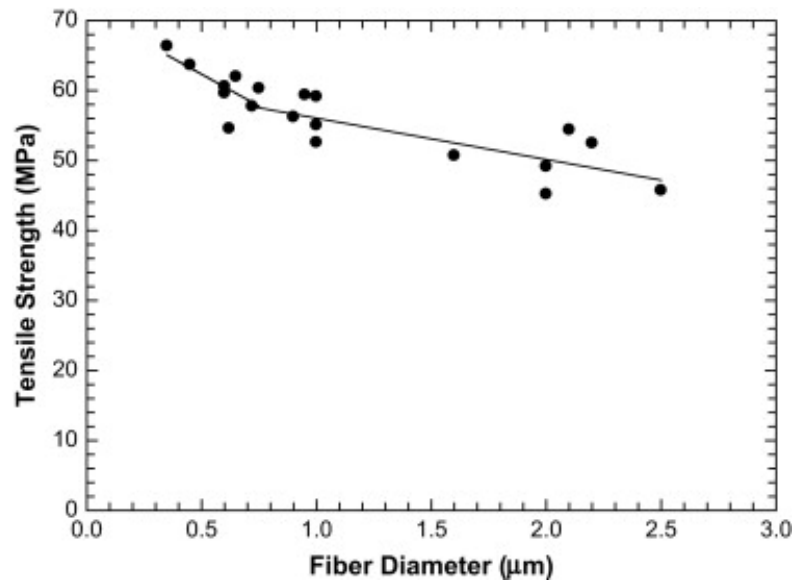


Figure 2.20 Plot of tensile strength vs. fiber diameter. Tensile strength increases with a decrease in fiber diameter [144].

2.9 Wong and Coworkers' Recent Work on Adhesion between Electrospun Fibers

Recently research on adhesion properties between single electrospun fiber is conducted by Wong and coworkers [8]. Direct pull-off adhesion test is performed by using of high resolution (50 nN/10nm) nanoforce tensile tester (MTS Nano Bionix). The single electrospun fibers are collated and carefully moved to cardboard frame, then fixed to the frame by high strength glue. The frame is cut into U shape as shown in Figure 2.21 (a). Two free-standing fibers are moved to tensile tester, and the frame is fixed by upper and lower grips separately, as shown in Figure 2.21(b). The fibers are arranged orthogonal to each other, in order to ensure the contact area is a circle, as shown is Figure 2.21 (c).

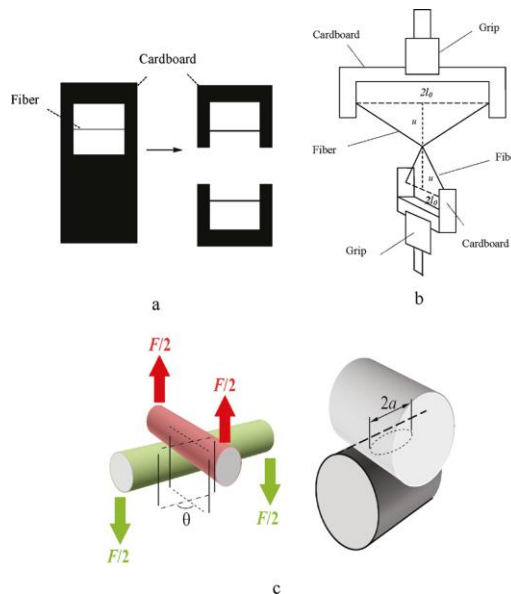


Figure 2.21 Schematic of the dry adhesion test. (a) The cardboards are cut into U shapes and mounted on the nanoforce tensile tester (b) Two fibers are arranged in the cross-cylinder geometry, and the contact circle has a diameter of $2a$ (c). Vertical compressive load deforms the two fibers into V-shapes [8].

The mechanical response under a constant loading speed is recorded, as shown in Figure 2.22. The entire cures contact elastic linear stretching region, followed a stable plateau, then a precipitous drop exhibited. The pull-off force is obtained from the stable plateau region. The relationship between pull-off force and fiber diameter is shown in Figure 2.23, a monotonic increase in log-log plot is shown, and confirmed with JKR model.

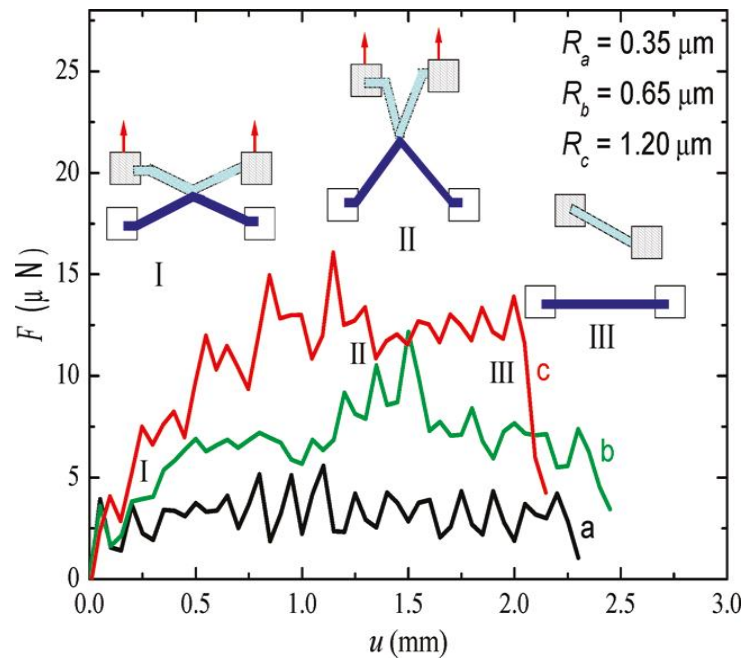


Figure 2.22 Applied external load F measured as a function of crosshead displacement u for PCL fibers of three different radii [8].

The adhesion strength is the pull-off force per unit area. JKR model is adopted to calculate the actual contact area between two single fibers. The relationship between

adhesion strength and fiber diameter can be obtained from Equation 2.16 , as shown below [8],

$$\frac{F^*}{s} = \left(\frac{2}{3}WE^2\right)^{1/3}R^{-1/3} \quad \text{Equation 2.16}$$

where E is the elastic modulus and W is the adhesion energy. Figure 2.24 shows the relationship between adhesion strength and fiber diameter. Adhesion strength is increasing in a consistent slop with the fiber diameter increasing.

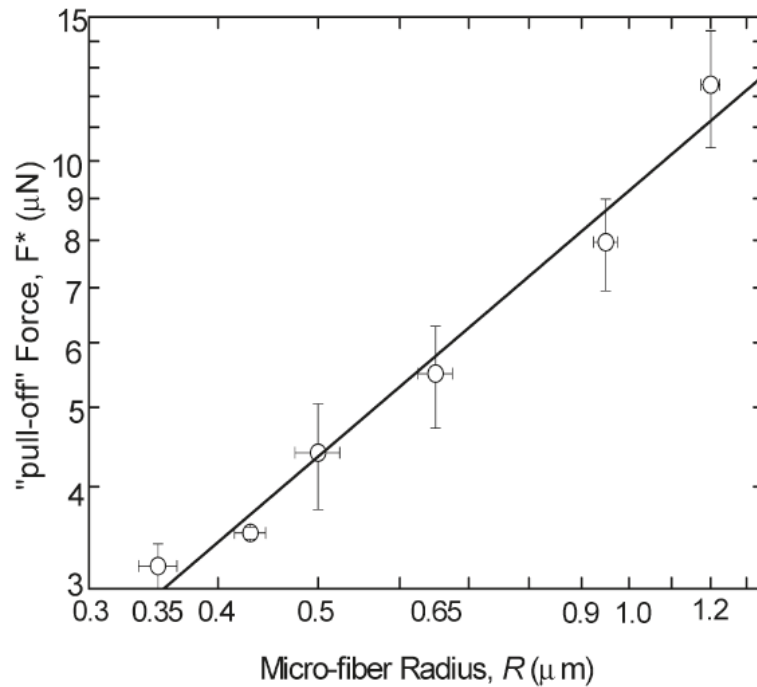


Figure 2.23 Measured “pull-off” force as a function of fiber radius. Data are fitted to a linear relationship according to the JKR theory [8].

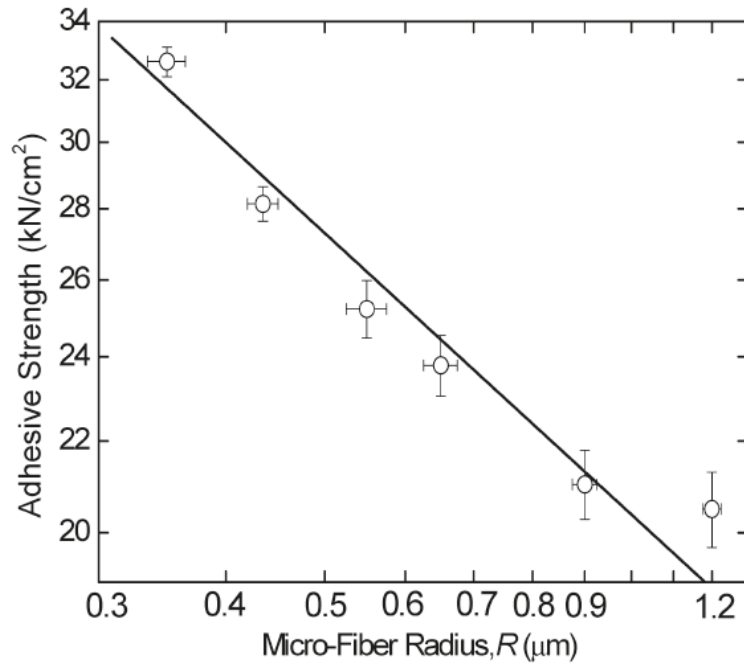


Figure 2.24 Adhesive strength as a function of fiber radius. The adhesion strength increases with decreasing fiber radius [8].

Pull-off speed is also considered as an important parameter [145]. Pull-off force substantially increased when the pull-off speed increase from 0.1mm/s to 1mm/s, as shown in Figure 2.25. They attribute the speed feect to the nonequilibrium state of fiber surface, which caused by the process of electrospinning. Viscoelasticity is also considered to be a factor to affect pull-off force, because the viscoelasticity is a rate dependent parameter.

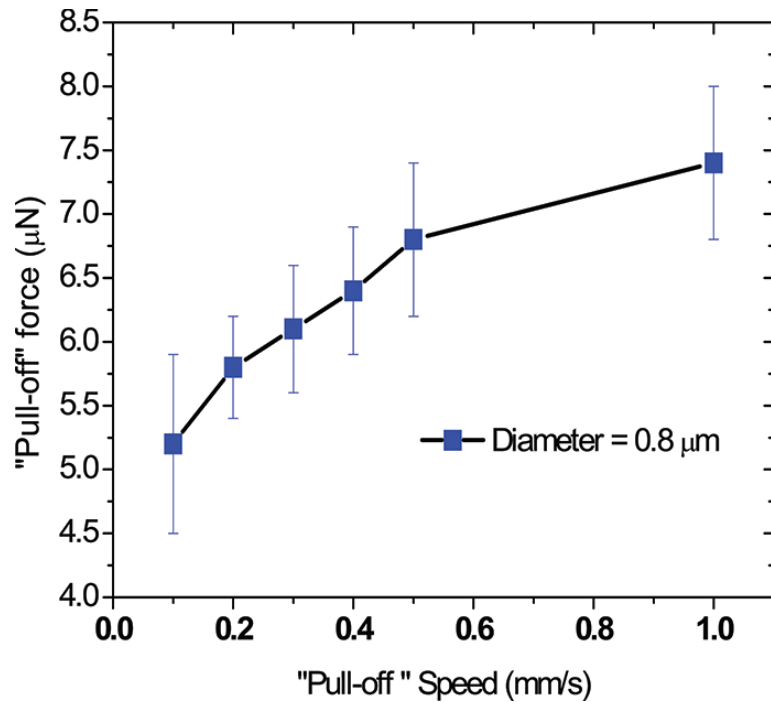


Figure 2.25 Adhesive force as a function of pull-off speed [145].

Temperature effect is also considered by Shi and co-workers [145], as shown in Figure 2.26. They observed an abrupt adhesion energy increase at around 30 oC. The transition of surface properties or the internal structure change of electrospun fibers may be the explanation for that. Irregular surface of electrospun fiber may cause a point contact rather than an area contact. And temperature increase may soften the fiber, and initial a better area contact. Roughness data characterized by AFM under different temperature confirmed high temperature can cause a decrease of surface roughness.

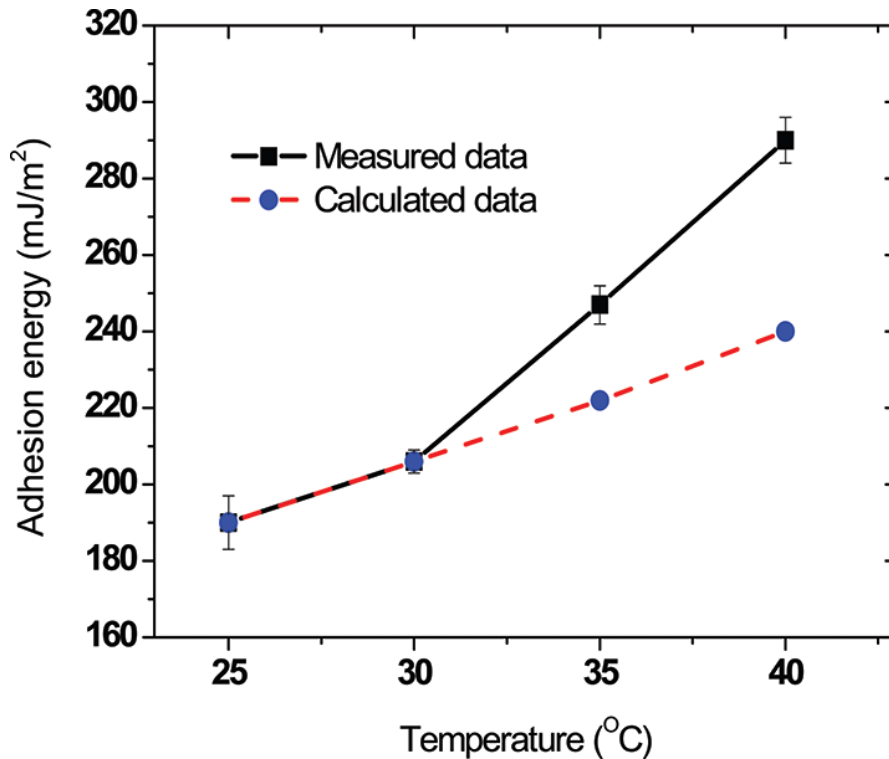


Figure 2.26 Comparison of adhesion energies between measured and theoretical data [145].

The polymer chain mobility is also considered as an impotent factor to affect the adhesion energy under different temperature [146-147]. The mobility of polymer chain is confined within the narrow space, and extended along the longitudinal direction. Temperature increasing may increase the probability of interdiffusion and interaction between polymer chains. Hence, the polymer chain mobility in the surface is increased coordinately. The degree of molecular orientation decreases with temperature decreases, as observed from XRD results, confirmed the increasing of polymer chain mobility. Therefore enhanced chain mobility can be expected at the interface.

CHAPTER III

RATIONALES OF THE DISSERTATION

By studying existing adhesives technology, researchers shown highly interested in gecko-inspired dry adhesives which are one of the most emerging adhesives technology. Gecko-inspired dry adhesives have several functional advantages, like high pull-off force, materials independence, self-cleaning, non-sticky default state etc. Existing gecko inspired adhesives are mainly produced by micro-fabrication, as reviewed in Chapter II. Electrospinning is firstly proposed by Shi and co-workers [8] to produce nano scale fibers which possess similar dry adhesives properties as gecko foot hairs.

Researchers believe, the spatial constraint applied to polymers by electrospinning restricts polymer segmental motion and hence enhances mechanical properties. However there is lack of research in adhesion mechanism of electrospun fibers. Polymer fibers from electrospinning have fiber diameter same as gecko foot hair, and are as flexible as gecko foot hair. Evidence [148] shows electrospun fibers exhibit significant improvement in adhesion strength and adhesion energy compare to bulk materials.

After that, the author conducted a series of adhesion experimental studies on adhesion energy of electrospun membranes. The contact mechanism of electrospun membranes is not well addressed in macro scale. The contact theory could be a combination of several different contact modes. The theoretical study is also carried by

the author to explain the adhesion phenomenon. Therefore theoretical and experimental study on adhesion property of electrospun fibers become the topic of the dissertation, and will be addressed in following chapters.

3.1 Hypothesis

In order to fully understand the adhesion phenomenon between electrospun fibers and different substrate, adhesion mechanics and classical theories of adhesion are reviewed. Since the adhesion energy between single polymer fibers is comparatively high [8], the electrospun fibrous membrane will have the potential to show high adhesion energy in macro scale if it was fabricated and analyzed in a proper way.

The first problem needs to be solved is establishing a proper adhesion test method for electrospun membrane. There are several existing methods to test adhesion between polymer film and substrate. However, test method of membrane adhesion is not well developed. Electrospun membrane is thin and flexible, the self-support ability is poor. The existing peel test and direct pull-off test always cause a cohesive failure of the membrane before adhesive failure, and then adhesion property cannot be well addressed. Blister test is one of the popular test methods for film adhesion test. A shaft loaded blister test (SLBT) is firstly developed from classical blister test by Wan and co-workers [149]. In this dissertation, SLBT is first time adopted to test membrane adhesion.

Several gecko-inspire adhesives succeed to show proven adhesion strength in nano scale, but fail to demonstrate adhesion strength in macro scale [6]. In macro scale, adhesion is affected by various factors. Although van der Waals force is well studied in

molecular scale, the dry adhesion property can be dominated by more factors other than van der Waals force. The author will use SLBT test to systematically study the adhesion phenomenon between electrospun membrane and different substrates, and try to establish an adhesion theory for electrospun materials.

3.2 Validation

In Chapter V, SLBT test will be proved by the theory of contact mechanics. A mathematical derivation will be showed to derive the governing equation of SLBT test. In the following Chapter VI, SLBT test will be applied to test the work of adhesion between PVDF electrospun membrane and inorganic rigid substrate. FEA modeling will be adopted to verify the results.

After validating SLBT as an effective test method to measure adhesion energy of electrospun membrane, key parameters which could affect adhesion property of electrospun membrane will be studied. Fiber diameter plays the most critical role in fiber's mechanical performance. Fiber diameter may also affect the van der Waals attractive force by influencing contacting distance and surface property. The relationship between fiber diameter and macro scale adhesion property is discussed comprehensively in Chapter VII. The thickness effect is also discussed by varying the thickness of the electrospun membrane.

Adhesion property is a matter of two contact bodies. After studying the influent parameter of electrospun membrane, the effect of substrate also needs to be considered. If the substrate material keeps unchanged, the changing of surface morphology may cause a difference on adhesion performance. SiC surface with different roughness are used to

evaluate the work of adhesion. The mechanism of rough contacting is also discussed and the experimental results are explainable by contact mechanics. By replacing the substrate with different materials, the work of adhesion is considered to have a change correspondingly. Cast PCL substrate and electrospun PCL substrate are chosen to evaluate the substrate effect.

After understanding of the adhesion mechanism of electrospun membranes, an effort is made to apply the electrospun material to smart adhesive applications. In order to manipulate electrospun fibers like gecko, the action of the fiber can be controlled by filling in electrorheological fluid which can reversibly change its state from liquid to solid rapidly under electrical field. The fundamental study is the fabrication and testing of hollow electrospun fibers. In Chapter X, hollow PVDF fibers are fabricated in a single one-step collecting method, and the adhesion property of hollow PVDF fibers are measured, and compared with solid PVDF fibers.

Overall, this dissertation systemically addresses the adhesion mechanisms of electrospun membranes experimentally and theoretically. Contribution will be made in adhesion energy characterization of electrospun membranes. The adhesion mechanisms will be analyzed and summarized from the experimental results. Fruitful insights could be gained from this study in future adhesion characterization of electrospun membrane.

CHAPTER IV

EXPERIMENTAL METHODS

In Chapter IV, electrospinning technology to prepare tested samples will be introduced. The test method and instrument of shaft loaded blister test (SLBT) will be presented. A number of characterization technologies, which are adopted in the dissertation will be discussed at the end, including the micro-scale imaging (SEM, AFM), tensile testing, differential scanning calorimetry (DSC), Wide-angle X-ray diffraction (WXRd) and Fourier transform infrared spectroscopy (FTIR).

4.1 Fabrication of Electrospun Nonwoven

PVDF is dissolved in DMF and acetone with a volume ratio of 7:3 at 40-50 °C for 2 h, yielding a 0.17 g/mL solution as reagent. Solution with different concentration is also prepared for further test, for example 0.15 g/mL and 0.20 g/mL. The PVDF solution is then electrospun into fibrous nonwovens by using a single syringe setup under ~10 kV, as shown in Figure 4.1. The nonwovens are subsequently treated and described as a membrane in the dissertation.

A grounded custom-made rotating roller collector wrapped around by aluminum foil collects the fibers. Solution feed rate is adjusted to 0.3 mL/h and the needle is

positioned 8-9 cm from the collector. Ultrafine fibers are collected to form a non-woven random mesh. After 10 h, a 10 μm thick PVDF membrane is made. The thickness is measured by a micrometer with 0.1 μm resolution. The sample membrane is then peeled off from the aluminum foil and dried in vacuum oven at 50 $^{\circ}\text{C}$ for 12 h.

PCL is electrospun in a similar way with different solvents of CHCl_3 and DMF. Collected PCL membrane needs to be dried in vacuum oven at 50 $^{\circ}\text{C}$ for 12 h. After drying, PCL need to be kept in a dry box all the time before testing, due to its hydrophilic character.

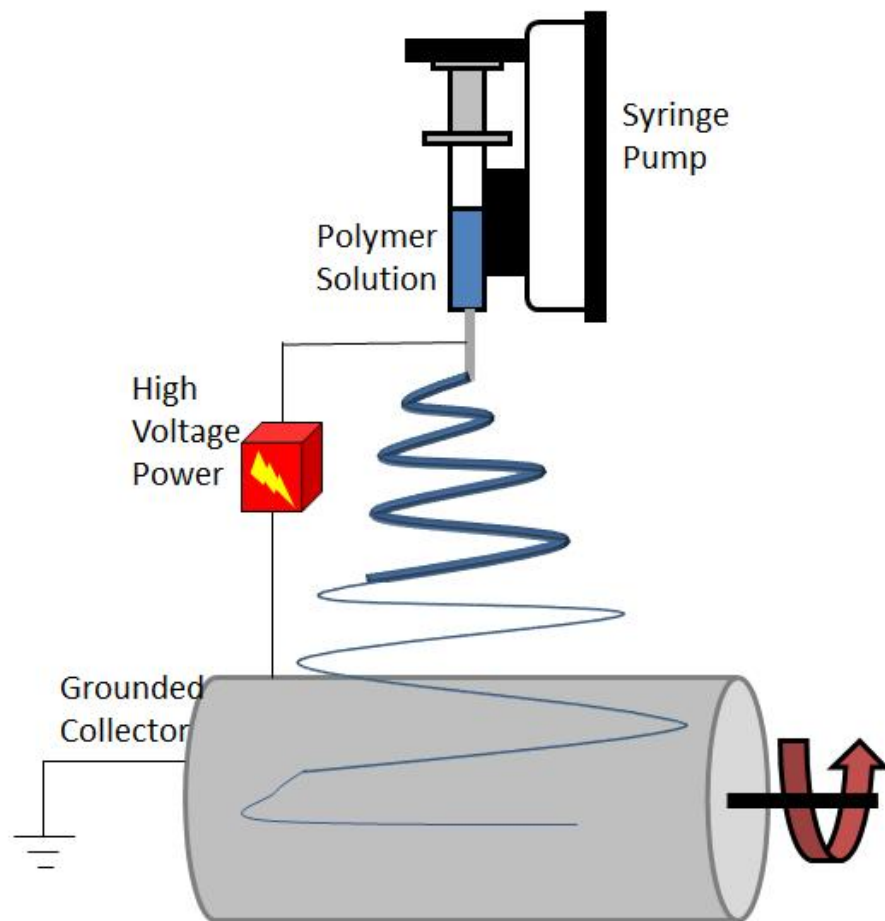


Figure 4.1 A schematic of electrospinning station. A syringe pump is used to control solution feeding rate, and a 10 KV voltage is applied to the needle. A costume-made rotate collector is used to collect fibers. After collecting, fibrous membrane will be peeled from the collector.

4.2 Polymer Film Casting

For comparison of surface morphology, the PVDF solution same as the one for electrospinning is cast onto a smooth glass slide. The slide together with PVDF solution is heated at 50-60 °C on a hot plate. Following solvent evaporation, PVDF is solidified and a PVDF film is formed and removed from the glass slide.

PCL solution is also cast in a similar way. 0.12 g/mL PCL solution is poured onto the top surface of a smooth glass slide and kept in air at room temperature for 5 h. With the solvent evaporation, cast PCL film is formed from PCL solution. Then the glass slide together with the cast PCL film is located on a hot plate (VWR scientific) at 50-60 °C for 2-3 h. Until the solvents are completely evaporated, ~10 μm cast PCL film is prepared and then removed from the glass slide.

4.3 Setup for SLBT Adhesion Measurement

SLBT adhesion test is the primary test method in the dissertation. SLBT adhesion test consists of two tested materials, which are the adhesion supplier. In the dissertation, electrospun membrane from different polymers and substrates from different materials are the two components of the tested materials.

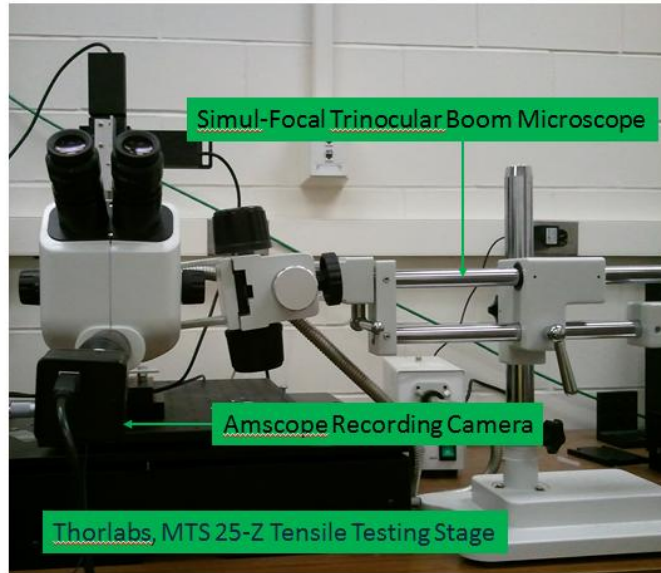


Figure 4.2 Digital image of tensile testing stage, microscope, and recording camera.

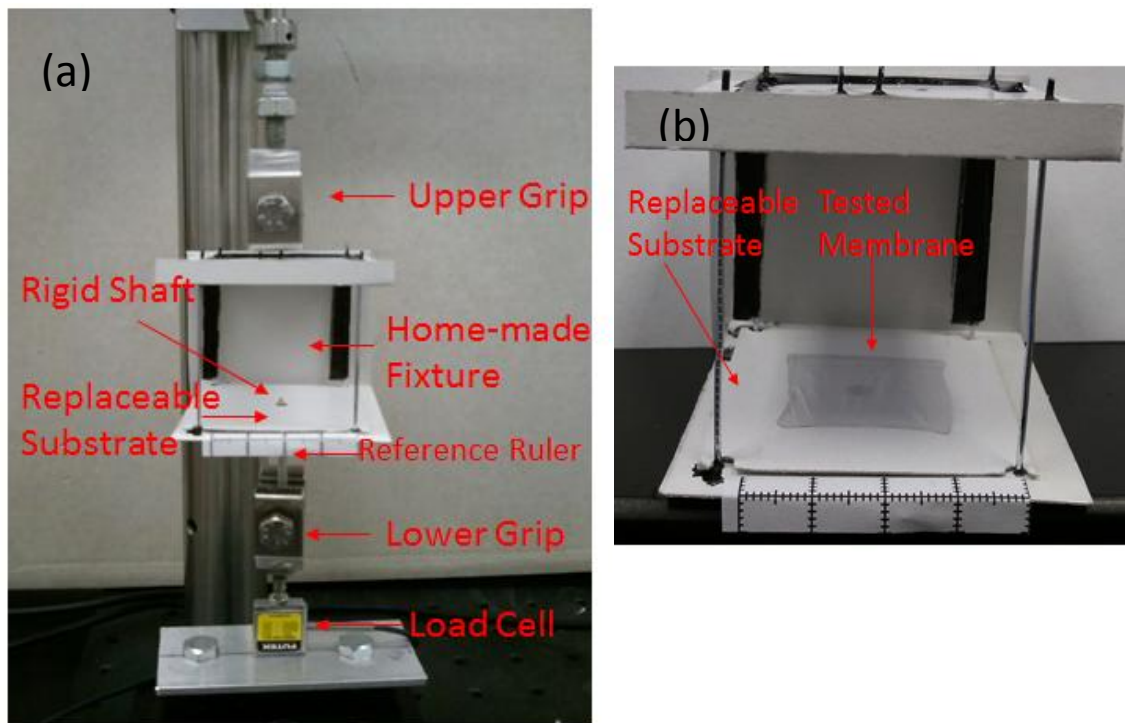


Figure 4.3 (a) Setup of SLBT adhesion test, including the load cell, lower/upper grip, home-made fixture, reference ruler, replaceable substrate and rigid shaft. (b) A close view of home-made fixture, a tested membrane is attached to the replaceable substrate.

Figure 4.2 and Figure 4.3 present the setup of SLBT tests. Electrospun membrane is cut to square of 30mm by 30mm for measurement. Rigid substrate is cleaned and fixed to the customer fixer, which is illustrated in Figure 4.4(a). Figure 4.4(a) shows a schematic of SLBT tests. Electrospun membrane is flattened onto the rigid substrate. A rigid shaft with spherical cap ($R=0.35\text{mm}$) is used to apply force (P) to membrane. In the test, the shaft is fixed, and the substrate moves down in a consistent speed at 20 mm/min. Before the test, the shaft is set to contact with the membrane, but no debonding between membrane and substrate happens, as shown in Figure 4.4(a). When test begins, initial vertical displacement does not cause delamination, but leads to a deformation of the local area where close to the shaft end. Blister debonding happens when the applied load exceeds a critical threshold.

During the SLBT test, applied load P is recorded by a 1N load cell (Futek Advanced Sensor Tech) simultaneously. The whole test is monitored by 7X-45X Simul-Focal Trinocular Boom Microscope, and recorded by a 3M camera (AMscope), as shown in Figure 4.2. Video captures are analyzed by ImageJ 1.45s to obtain in-situ deformation profile. Therefore, the relationship between delamination radius (a) and central deflection (w_0) can be obtained. For adhesion tests with different substrates, test substrates are prepared by adhering desired substrate on top surface of a rigid paper cardboard by super glue.

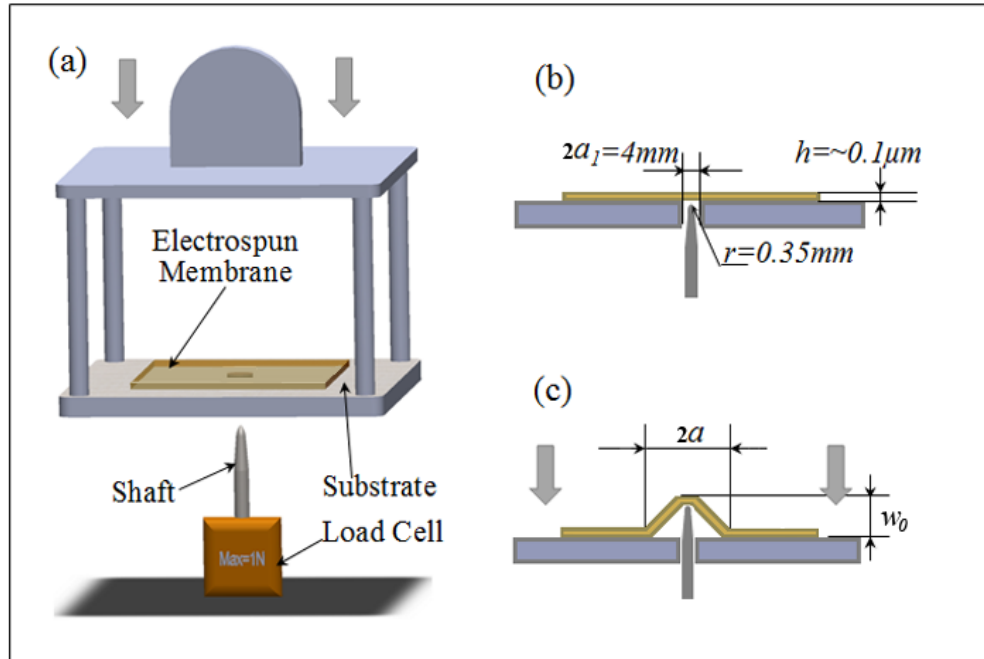


Figure 4.4 A schematic illustrating the apparatus and process of the shaft-load blister test. The apparatus is shown in (a) rigid substrate with a round hole bored through its center and clamped by a fixture. Electrospun PVDF attaches onto the top surface of the rigid substrate. Central shaft with a spherical cap located below the center of the hole offers an external load. Adhesion tests are motorized by 1" travel stage imperial (Thorlabs, MTS 25-Z) and the debonding forces are recorded by 1 N load cell (Futek Advanced Sensor Tech). The detailed dimensions of the apparatus are described in (b). Both (b) and (c) exhibit the formation of a blister and debonding between the membrane and rigid substrate with a testing speed at 20 mm/min.

4.4 Scanning Electron Microscopy (SEM) characterization

SEM is the most direct way to analyze the morphology of micro-size sample. The most common used signals of SEM are second electrons and back-scattered electrons. Second electron imaging (SEI) generates image from interactions of the electron beam with atoms at or near the surface of the sample. SEI can always achieve very high resolution, such as less than 1 nm. The magnification can be changed in a wide range from 10X to more than 500,000X. Back-scattered imaging (BEI) generates image from reflected electrons from sample by elastic scattering. BEI can provide information about the distribution of different elements other than imaging the surface.

In this dissertation, morphology of electrospun membranes is characterized by SEM (JEOL JSM-6510LV) by using second electrons. Before imaging, samples are coated with argentineum by sputter coater (K575x, Emitech) for 1.5 min at 55 A. Average fiber diameter and fiber density are determined from SEM micrographs by software ImageJ 1.45s. For each sample, five images are used for calculation. Total 100 fibers are measured for average diameter calculation. Nominal fibrous surface area is calculated by measuring the total area occupied by electrospun fibers in SEM micrographs.



Figure 4.5 Scanning electron microscopy (JEOL JSM-6510LV).

4.6 Atomic Force Microscopy (AFM) Measurement

AFM is a very high resolution scanning probe microscope. An AFM consists of a cantilever with a tip. The tip will be tapping to examine the surface. AFM can be operated in a number of modes. The most common operation modes are contact mode, non-contact mode and tapping mode. In contact mode, the tip is statically snap-in and drag to scan the surface. The tip does not contact with the sample surface in non-contact mode. The tip is oscillated near its resonant frequency with a few nanometers amplitude. Tapping mode, also named intermittent contact mode, makes the tip oscillate near its resonance frequency with an amplitude around 100-200 nm. The relatively large

amplitude gives the tip a chance to contact with the sample surface intermittently, and the damage of the tip is less compared with contact mode.

AFM (Ntegra Spectra, NT-MDT). with a HA_NC/15 probe is used to characterize the surface topography under ambient conditions. Tapping mode is adopted for image scanning. Images are taken with the scan sizes of $10 \times 10 \mu\text{m}$ by using the tapping mode. Membrane surfaces are imaged prior to and after the adhesion tests. Cast film is also imaged, for purposes of morphology comparison between electrospun membrane and cast film.

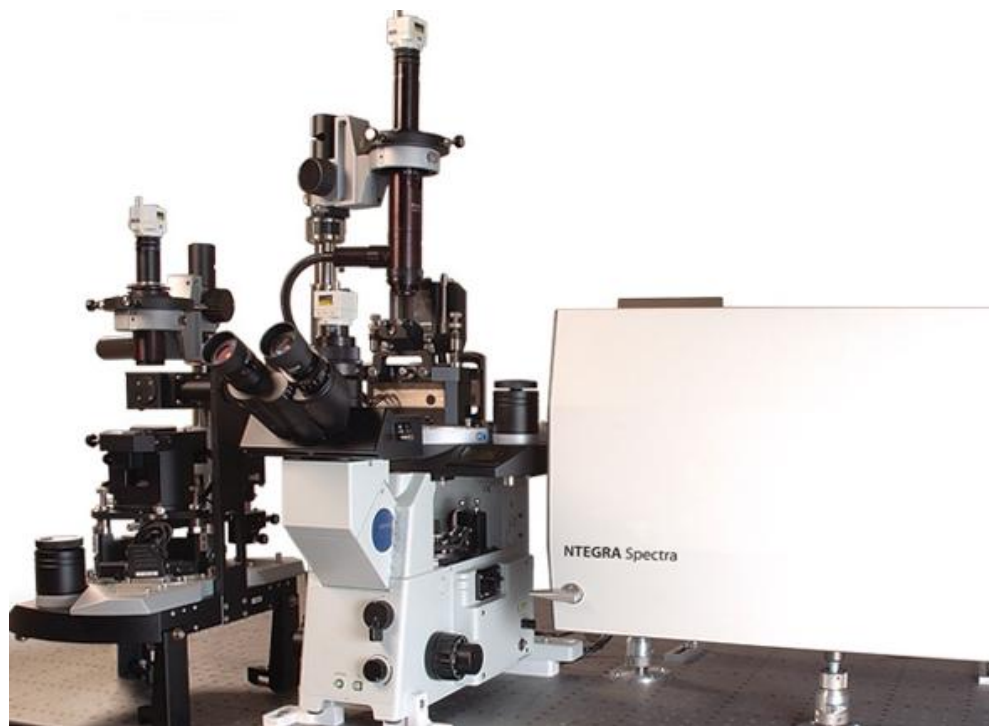


Figure 4.6 Atomic force microscopy (Ntegra Spectra, NT-MDT).

4.7 Tensile Test

Tensile testing is the most common method to understand materials; mechanical properties, including elastic modulus, Poisson's ratio, yielding strength, strain-hardening etc. Electrospun membrane tested by a universal tensile tester (Thorlabs, MTS 25-Z). 10- μm thick sample membranes are cut into $40 \times 10 \text{ mm}^2$ with a gauge length of 20 mm. PVDF membrane is clamped by a tensile fixture which is controlled by 1" travel stage, which is the one shown in Figure 4.2, at the speed of 5 mm/min. Tensile test is carried out by using a 45 N load cell (Futek Advanced Sensor Tech) at room temperature, and is repeated 5 times to obtain an average value.

Though elastic modulus can be obtained in the SLBT measurement, additional standard tensile test is performed to ensure consistency. Fiber diameter effect on mechanical properties of electrospun membrane is also evaluated by tensile test.

4.8 Differential Scanning Calorimetry (DSC)

DSC is a thermoanalytical tool to understand the heat capacity over a range of temperature. DSC measures the temperatures and heat flows associated with transitions in materials as a function of time and temperature in a controlled atmosphere. These measurements provide quantitative and qualitative information about physical and chemical changes that involve endothermic or exothermic processes, or changes in heat capacity. Therefore, crystallization, glass transition, fusion can be observed during the temperature scanning.

In this work, DSC is used to determine the melting point of polymers, and the crystallinity of polymers calculated from DSC curves by integrating the peak of crystallization. .

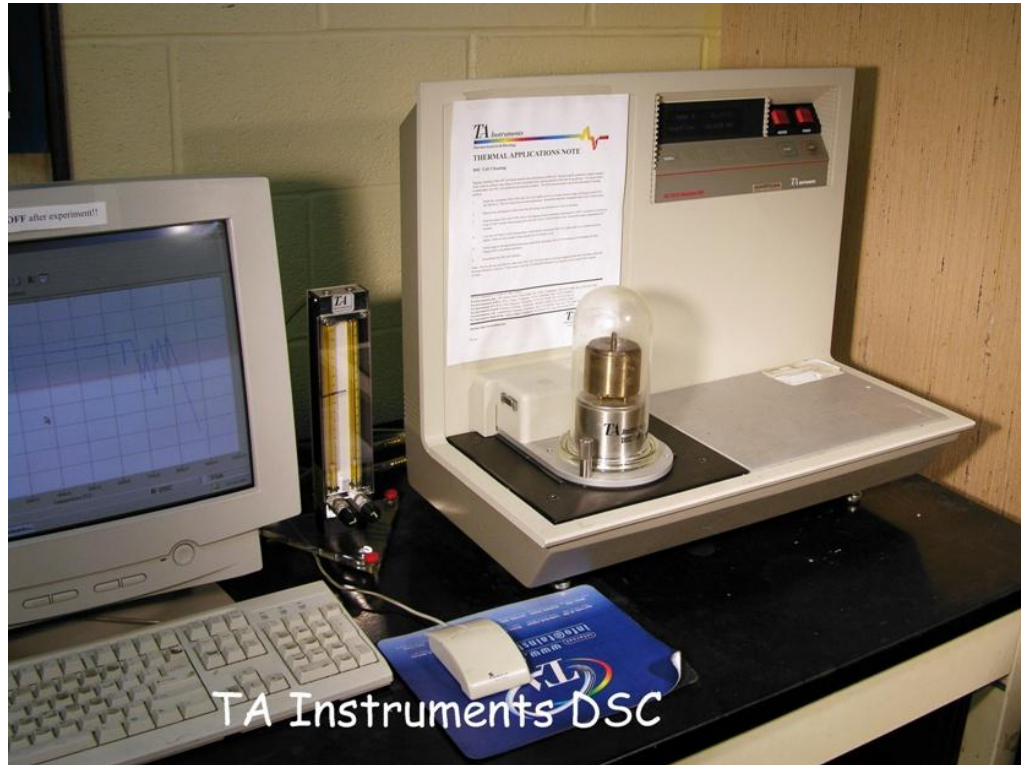


Figure 4.7 Digital image of TA DSC

4.9 Wide-Angle X-ray Diffraction (WAXD)

When X-rays are directed in solids they will scatter in predictable patterns based upon the internal structure of the solid. A crystalline solid consists of regularly spaced atoms (electrons) that can be described by imaginary planes. The distance between these planes is called the d-spacing. The intensity of the d-spacing pattern is directly proportional to the number of electrons (atoms) that are found in the imaginary planes.

Every crystalline solid will have a unique pattern of d-spacing (known as the powder pattern), which is a “finger print” for that solid. In fact solids with the same chemical composition but different phases can be identified by their pattern of d-spacing. Small-angle X-ray diffraction (SAXD) is based on the same principle. Only the distant from the sample to the X-ray detector is shorter, and then diffraction at larger angles can be observed.

In this work, crystal structure of polymers are examined by WAXD. XRD patterns of hollow fibers are obtained from an X-ray diffractometer (AXS D8 Discovery, Bruker) with Cu K α radiation ($\lambda=1.5405\text{nm}$).

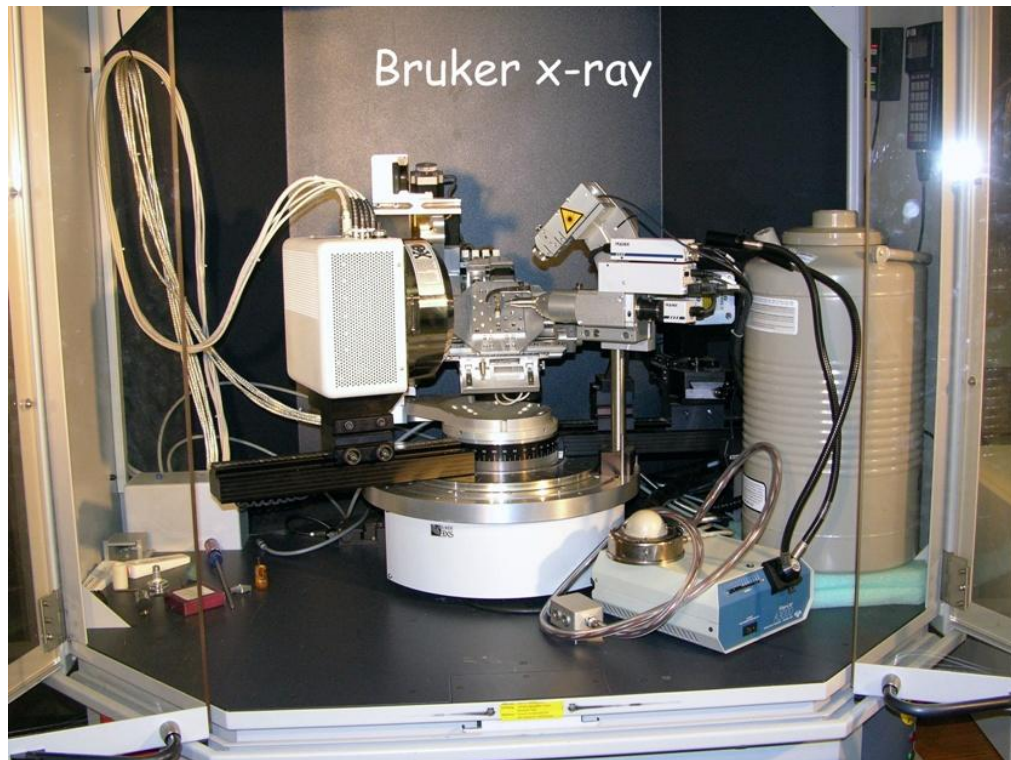


Figure 4.8 Digital image of Bruker WAXD equipment

4.10 Fourier transform infrared spectroscopy (FTIR)

Principle of Fourier Transform-Infrared Spectroscopy (FTIR) is to measure the sample's capacity of light absorption at each wavelength. Firstly the FTIR machine shines a beam containing many frequencies of light at once, and measures how much of that beam is absorbed by the sample. Next, the beam is modified to contain a different combination of frequencies, giving a second data point. This process is repeated many times, for our experiment, it repeated for 32 times. Afterwards, a computer takes all these data and works backwards to infer what the absorption is at each wavelength. The infrared absorption bands can identify molecular components and structures. As a widely used analytical technique, FTIR is always used to identify organic (and in some cases inorganic) materials. For this work, FTIR (Nicolet 380) is used for crystal structure Identification. The samples are placed on top of an attenuated total reflection set and scanned from 650 to 4000 cm^{-1} .

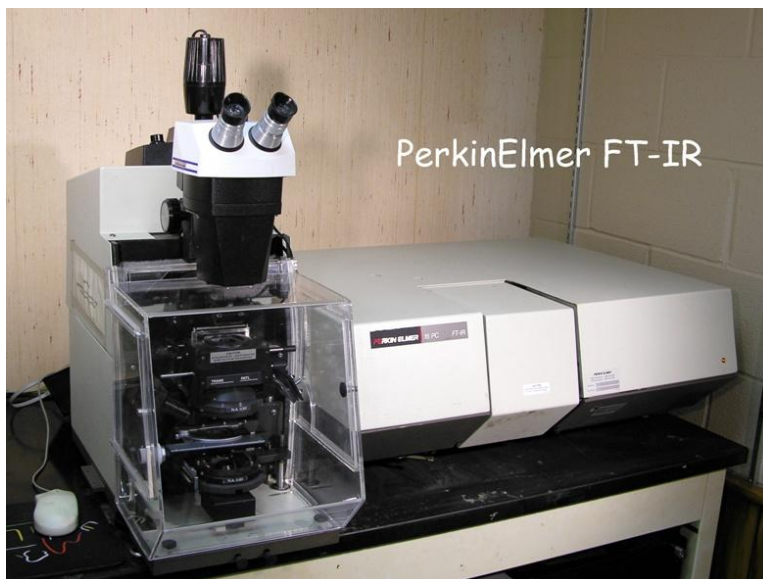


Figure 4.9 Digital image of PerkinElmer FT-IR

CHAPTER V

THEORETICAL STUDY BASED ON SLBT TEST

5.1 Governing Equation of SLBT Test

The setup of the SLBT (Shaft Loaded Blister Test) test is shown in Figure 5.1. A round hole is bored through the rigid substrate prior to the adhesion of sample fibrous membrane. An external load, P , is applied to the membrane center via a shaft with a spherical cap of radius, R . In SLBT test, the tested membrane is thin and flexible, no bending moment is considered during test. The contact between shaft end and membrane is considered as a point contact, therefore the radius of the shaft end needs to be small enough to be neglected, (in this case $R=0.7$ mm). The deformation process is considered as elastic deformation at the beginning, and only the liner elastic range is used for further evaluation.

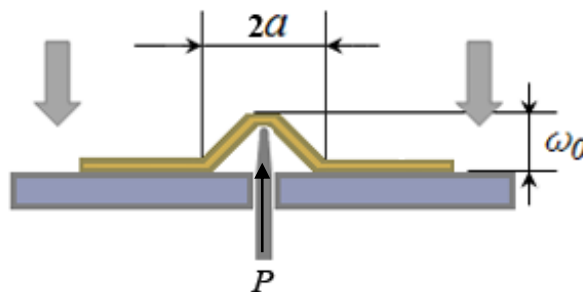


Figure 5.1 A schematic of SLBT test

The radial strain ε_r and the tangential strain ε_t can be expressed by [150]:

$$\varepsilon_r = \frac{du}{dr} + \frac{1}{2} \left(\frac{dw}{dr} \right)^2 \quad \text{Equation 5.1}$$

$$\varepsilon_t = \frac{u}{r} \quad \text{Equation 5.2}$$

where u is the radial displacement and w is the deflection of the membrane from the substrate surface. Substituting Equation 5.2 into Equation 5.1,

$$\varepsilon_r = \frac{u}{r} + r \frac{d}{dr} \left(\frac{u}{r} \right) + \frac{1}{2} \left(\frac{dw}{dr} \right)^2 \quad \text{Equation 5.3}$$

For a circular membrane with large central deflection, the radial stress N_r and tangential stress N_t are constrained by [150]

$$N_r - N_t + r \frac{dN_r}{dr} = 0 \quad \text{Equation 5.4}$$

The relationships between stress (N_r, N_t) and strain ($\varepsilon_r, \varepsilon_t$) can be expressed by:

$$\varepsilon_r = \frac{1}{Eh} (N_r - \nu N_t) \quad \text{Equation 5.5}$$

$$\varepsilon_t = \frac{1}{Eh} (N_t - \nu N_r) \quad \text{Equation 5.6}$$

where E is the elastic modulus, h is the thickness of the membrane and ν is the Poisson's ratio of the membrane. Substituting Equation 5.5 and Equation 5.6 into Equation 5.3, and using Equation 5.4, the following equation can be obtained:

$$\frac{d}{dr} (\nabla^2 f) + \frac{Eh}{2r} \left(\frac{dw}{dr} \right)^2 = 0 \quad \text{Equation 5.7}$$

where f is the stress function defining

$$N_r = \frac{1}{r} \left(\frac{df}{dr} \right) \quad \text{Equation 5.8}$$

$$N_t = \frac{d^2 f}{dr^2} \quad \text{Equation 5.9}$$

By adopting the principle of virtual work, energy balance can be expressed as [150]

$$2\pi \int_0^a [\psi \frac{d}{dr}(\delta\omega) + (N_r \delta\varepsilon_r + N_t \delta\varepsilon_t)] r dr = 0 \quad \text{Equation 5.10}$$

Equation 5.10 can be re-arranged as below:

$$2\pi \int_0^a (\psi + \frac{1}{r} \frac{df}{dr} \frac{d\omega}{dr}) \frac{d\omega}{dr} r dr = 0 \quad \text{Equation 5.11}$$

where ψ is the load function, for a point blister [150], we have $\psi = \frac{P}{2\pi r}$

The blister profile is expressed by a summation of series in the form of $\omega(r) = \sum a_i \phi_i(r)$, and it can be approximated to be conical, if the central deflection is small.

$$\omega(r) = \omega_0 (1 - \frac{r}{a}) \quad \text{Equation 5.12}$$

Therefore, substituting $\frac{d\omega}{dr} = -\frac{\omega_0}{a}$ into Equation 5.7,

$$\frac{df}{dr} = \frac{Eh\omega_0^2}{4a^2} r (C_1 - \log r) + \frac{C_2}{r} \quad \text{Equation 5.13}$$

where C_1 and C_2 are integration constants. If we consider two boundary conditions as below:

$$P = 2\pi a N_r |_{r=a} \sin \theta \quad \text{Equation 5.14}$$

$$(df/dr)_{r=0} = 0 \quad \text{Equation 5.15}$$

where $\theta = \tan^{-1} \omega_0/a$

Therefore, $C_1 = P/2\pi\omega_0 \cos \theta$, $C_2 = 0$, then Equation 5.13 can be written as:

$$\frac{df}{dr} = \frac{Eh\omega_0^2}{4a^2} [r (\log \frac{a}{r}) + \frac{Pr}{2\pi\omega_0 \cos \theta}] \quad \text{Equation 5.16}$$

Substituting Equation 5.16 into Equation 5.11, a relationship can be established:

$$\frac{\pi Eh\omega_0^2}{8Pa^2} = k_{el}(\theta) = 1 - \frac{1}{2 \cos \theta} \quad \text{Equation 5.17}$$

If $\theta < 25^\circ$, we can consider $\cos \theta \approx 1$, therefore $k_{el}(\theta) \approx 0.5$, and the interrelationship between the three measurable quantities, P - w_0 - a , can be obtained as below:

$$P = \frac{\pi E h \omega_0^3}{4 a^2} \quad \text{Equation 5.18}$$

Equation 5.18 is the governing equation for the SLBT test, and the interrelationship can be used for further adhesion energy calculation.

5.2 Adhesion Energy Calculation

According to linear fracture mechanics, the the potential energy of external load U_{PE} , the elastic energy stored in the elastic membrane U_{EL} and the surface energy creating a debonding area U_S are given by:

$$U_{PE} = -P\omega_0 = -2\left(\frac{k_{el}P^4a^2}{\pi Eh}\right)^{1/3} \quad \text{Equation 5. 19}$$

$$U_{EL} = \int P(\omega_0)d\omega_0|_a \approx \frac{1}{2}\left(\frac{k_{el}P^4a^2}{\pi Eh}\right)^{1/3} \quad \text{Equation 5. 20}$$

$$U_S = \pi a^2 W \quad \text{Equation 5. 21}$$

The total mechanical energy of the system is given by:

$$U_M = U_{PE} + U_{EL} \approx -\frac{3}{2}\left(\frac{k_{el}P^4a^2}{\pi Eh}\right)^{1/3} \quad \text{Equation 5. 22}$$

At mechanical equilibrium, we have:

$$\delta U_M + \delta U_S = 0 \quad \text{Equation 5. 23}$$

By using Equation 5.21 and Equation 5.23, and the adhesion energy between membrane and substrate can be expressed as below, by adopting governing equation (Equation 5.18), it can also be express as:

$$W = -\frac{1}{2\pi a} \frac{dU_m}{da} = \left(\frac{k_{el}}{8\pi^4 Eh}\right)^{1/3} \left(\frac{P}{a}\right)^{4/3} \approx \frac{1}{4\pi} \left(\frac{P}{\omega_0}\right) \left(\frac{\omega_0}{a}\right)^2 \quad \text{Equation 5.24}$$

Adhesion measurement can be carried out by two distinct modes. In displacement-controlled configuration, where the shaft is forced to move a vertical displacement of w_0 while P and a are measured simultaneously. Substitutions of Equation 5.18 into Equation 5.24 yield,

$$W = \frac{Eh}{16} \left(\frac{w_0}{a}\right)^4 \quad \text{Equation 5.25}$$

A linear $w_0(a)$ relation is expected. In case of strong adhesion or large W , plastic yielding becomes inevitable at the membrane center where the highest membrane stress is present. The excessively large w_0 renders Equation 5.25 invalid. Alternatively, under a force control with fixed P ,

$$W = \left(\frac{1}{16\pi^4 Eh}\right)^{1/3} \left(\frac{P}{a}\right)^{4/3} \quad \text{Equation 5.26}$$

where a linear $P(w_0)$ relation is expected. Here, provided deformation at the blister edge or delamination front is elastic, Equation 5.26 remains valid even in the presence of plastic deformation. Equation 5.24, Equation 5.25 and Equation 5.26 present a mechanics-rigorous methodology for measuring adhesion work and elastic modulus using the SLBT.

5.3 Evaluation by Numerical Method

5.3.1 Problem Formulation

After analytical consideration, a numerical model has been developed to evaluate the SLBT test. In order to evaluate the SLBT test, the adhesion energy from experimental work is used as a known parameter. By given material properties, FEA model is used to verify the inter-relationship between applied force (P) central deflection (w_0) and debonding radius (a). The fibrous structure will not be illustrated in the model, and electrospun membrane is treated as a smooth thin layer of elastic materials.

By referring numerical studies of crack growth at an interface [151-154], the traction-separation relation is introduced to model the delamination between electrospun membrane and rigid substrate. Figure 5.2 shows the traction-separation law, where δ_n and δ_t donate the normal and tangential components of the relative displacement of the crack across the interface. The critical value of δ_n and δ_t are represented by δ_n^c and δ_t^c . Therefore, a single non-dimensional parameter can be defined as:

$$\lambda = \sqrt{\left(\frac{\delta_n}{\delta_n^c}\right)^2 + \left(\frac{\delta_t}{\delta_t^c}\right)^2} \quad \text{Equation 5.27}$$

when δ_n equals to δ_n^c and δ_t equals δ_t^c respectively, the separation happens, where $\lambda=1$. From Figure 5.2, an interfacial potential energy can be derived from the traction-separation law,

$$\phi(\delta_n, \delta_t) = \delta_n^c \int_0^\lambda \sigma(\lambda') d\lambda' \quad \text{Equation 5.28}$$

The normal and shear component of the traction across the interface in the crack can be derived from Equation 5. 28 by:

$$T_n = \frac{\partial \phi}{\partial \delta_n} = \frac{\sigma(\lambda)}{\lambda \delta_n^c} \delta_n ; T_t = \frac{\partial \phi}{\partial \delta_t} = \frac{\sigma(\lambda) \delta_t \delta_n^c}{\lambda \delta_t^c \delta_n^c} \quad \text{Equation 5.29}$$

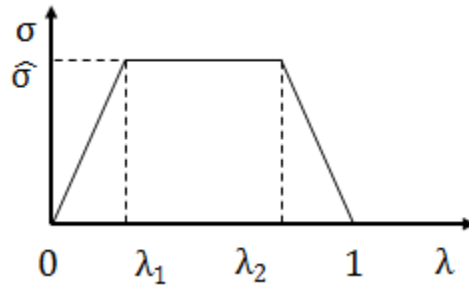


Figure 5.2 Traction-separation law

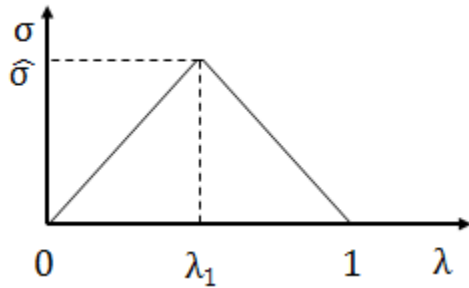


Figure 5.3 Simplified triangular traction-separation law.

In Figure 5.2, λ_1 and λ_2 are shape parameters. As discussed in literatures [153-154], the shape parameters only marginally influence the results. Therefore, the traction-separation law can be simplified to triangular shape. In a recent version of ABAQUS, the built-in cohesive element can be readily used, which is defined by triangular traction-separation

law. Therefore, the work of separation per unit area (Γ_0) can be obtained from Equation 5.28, at $\lambda=1$,

$$\Gamma_0 = \frac{1}{2} \hat{\sigma} \delta_n^c \quad \text{Equation 5.30}$$

Γ_0 is an important parameters during the delamination process, in our case, Γ_0 equals the adhesion energy between the electrospun membrane and substrate. The material is considered as elastic-plastic materials. The tensile property can be specified by:

$$\varepsilon = \begin{cases} \frac{\sigma}{E} & \sigma \leq \sigma_y \\ \frac{\sigma_y}{E} \left(\frac{\sigma}{\sigma_y}\right)^{1/N} & \sigma > \sigma_y \end{cases} \quad \text{Equation 5.31}$$

where σ_y is the yield stress, N is the power hardening exponent and E is the Young's modulus, respectively.

5.3.2 Numerical modeling

The finite element analysis is carried out using commercial finite element software ABAQUS. The base is simulated as a rigid body. Due to symmetry, only half of the membrane is considered. Young's modulus is obtained from tensile tests, as 23.04 MPa, and Poisson's ratio is 0.3. Thickness of the membrane is 10 μm . The built-in cohesive element is adopted to describe the adhesion characteristic between membrane and substrate. The cohesive layer obeys triangular traction-separation law as shown in Figure 5.3. The work of separation per unit area (Γ_0) is defined from the experimental, adhesive strength of the cohesive element $\hat{\sigma}$ is defined by $\hat{\sigma} / \sigma_{y1} = 3.0$ [155], and thus

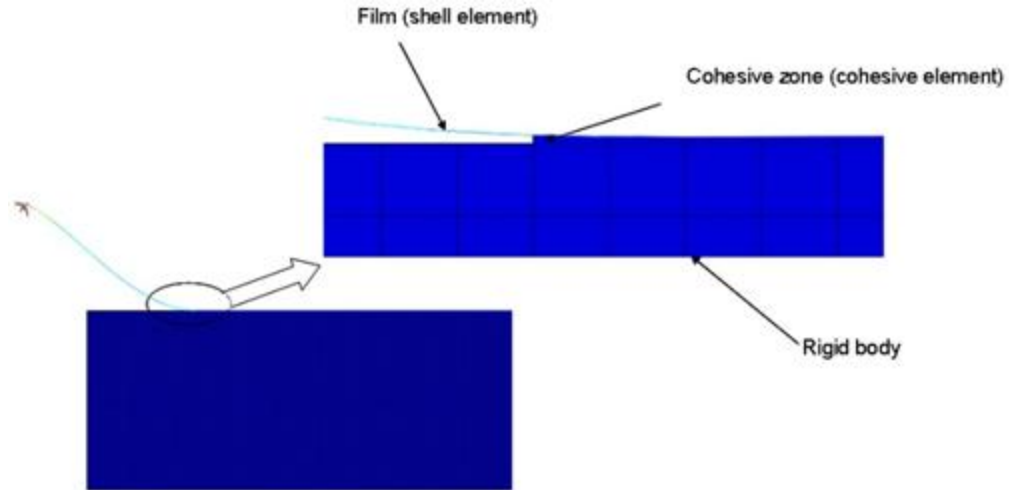


Figure 5.5 A configuration of membrane and substrate after testing.

In order to reach convergence, the element size of cohesive layer is critical. A parameter study is carried on the element size. Element sizes, ranging from 0.1 mm to 2 mm, are used for computation. The results are shown in Figure 5.6, no significant difference can be observed when element size increases from 0.1mm to 1mm. The slope, when element size is 0.1 mm, is calculated as 0.0305 N/mm. The slope only increases 10.8% to 0.0338 N/mm, when the element size increases from 0.1mm to 1 mm. However, if the element size enlarged to 2mm, the slope has 101.6% increase, and the value of slope reaches 0.0615 N/mm. Therefore, the critical element size is estimated to be 1mm. Hellerborg and co-workers [156] give estimation on critical length of element (L_c) in the case of plane stress consideration, by analysis the crack formation and crack propagation. The suggested critical length can be calculated from:

$$L_c = E \frac{G_c}{(\sigma_{max})^2} \quad \text{Equation 5.32}$$

where G_C is the critical strain energy release rate (N/mm), E is the elastic modulus (MPa), σ_{max} is the interfacial strength (MPa).

When element size is below 1.25mm, all of the curves reach a plateau after linear increasing. However, the results trends to diverge in the plateau for element size larger than 1.25mm. Without doubt, a fine mesh will give more accurate computation, but the computation time will also become longer. Finding the critical element size is helpful for further time-saving computation.

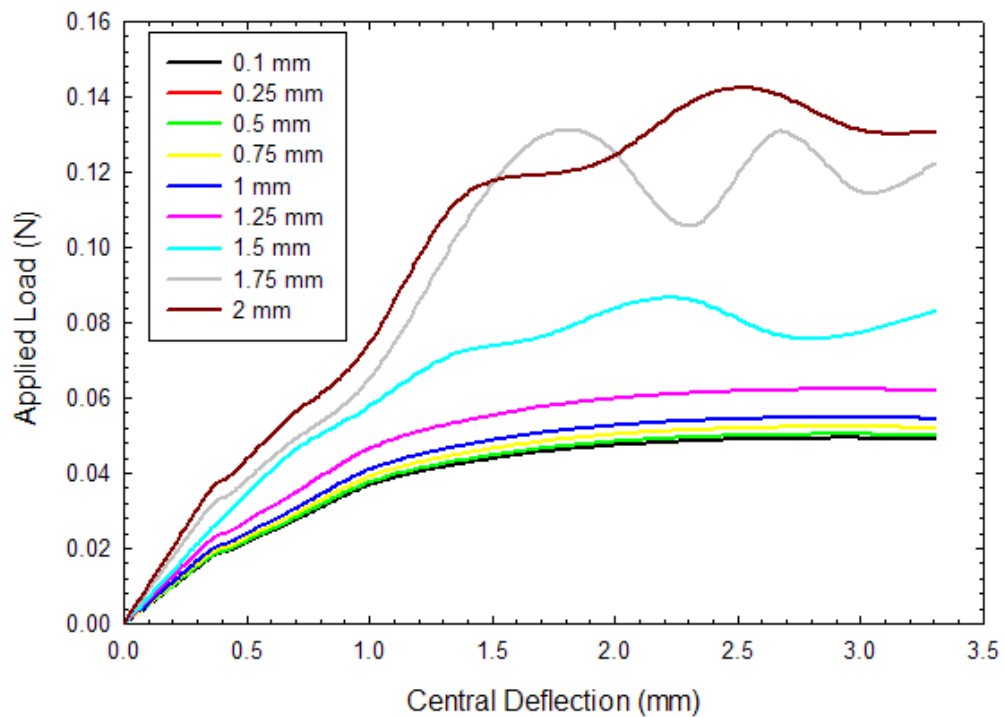


Figure 5.6 FEA results on element size study. Element size varies from 0.1 mm to 2 mm, and the relationship between central deflection and applied load is established.

CHAPTER VI

MEASUREMENT OF ADHESION WORK BETWEEN ELECTROSPUN MEMBRANE AND RIGID SUBSTRATE

6.1 Introduction

Recent understanding of naturally occurring dry adhesives [1-3] presents new frontiers in research for fabricating synthetic equivalents made of polymer fibers [8, 157-163]. One unique feature of polymer nanofibers is that they can be made flexible, mimicking muscular contraction and extension, in comparison to other rigid fiber structures [23]. Electrospinning offers a perfect tool to produce polymer nano and micro-fibers that can be imparted a high degree of flexibility with piezoelectricity [132,164] and magnetostrictive [165] mechanisms. To accomplish this, it is important to gain an understanding of the dry adhesion between polymer fibers and rigid substrates. Previously, we reported measuring the adhesion between two electrospun single fibers in cross-cylinder geometry [8]. In this chapter, we evaluate the adhesion work of electrospun membranes with rigid substrates. The objective aims to elucidate the mechanics that can be exploited in fabricating dry adhesives using polymer fibrous structures.

6.2 Sample Preparation

Polymer reagent PVDF (Kynar 761) from Arkema Inc. is used for electrospinning. Reagent grade solvents N,N-dimethylformamide (DMF) and acetone from Fisher Scientific are used as fiber precursors. The model substrate is a high-quality White Back Duplex Board (Expo India Agencies). The top surface of the cardboard is covered with a coating which includes high percentage nano-scale inorganic materials such as Kaolin, calcium oxide, calcium carbonate, etc. Nano-scale inorganic materials are usually used as the filler in exterior wall paint. So the cardboard could provide a lightweight and rigid substrate. Furthermore, it can mimic the flat model composed by inorganic materials.

PVDF nonwoven is prepared by electrospinning process. DMF and acetone with a volume ratio of 7:3 are used as solvent. PVDF solution is prepared by 0.17 g/mL. After 10 h, a 10 μm thick PVDF membrane is made for further adhesion tests.

Electrospun membrane is cut to square of 30mm by 30mm for measurement. Rigid substrate is prepared from cardboard with inorganic coating. The arithmetic average roughness (R_a) is approximately 128 nm. In order to make good contact, a lightweight plastic roller ($w \approx 100\text{g}$) was used to roll over the membrane onto the substrate to squeeze air bubbles between membrane and substrate.

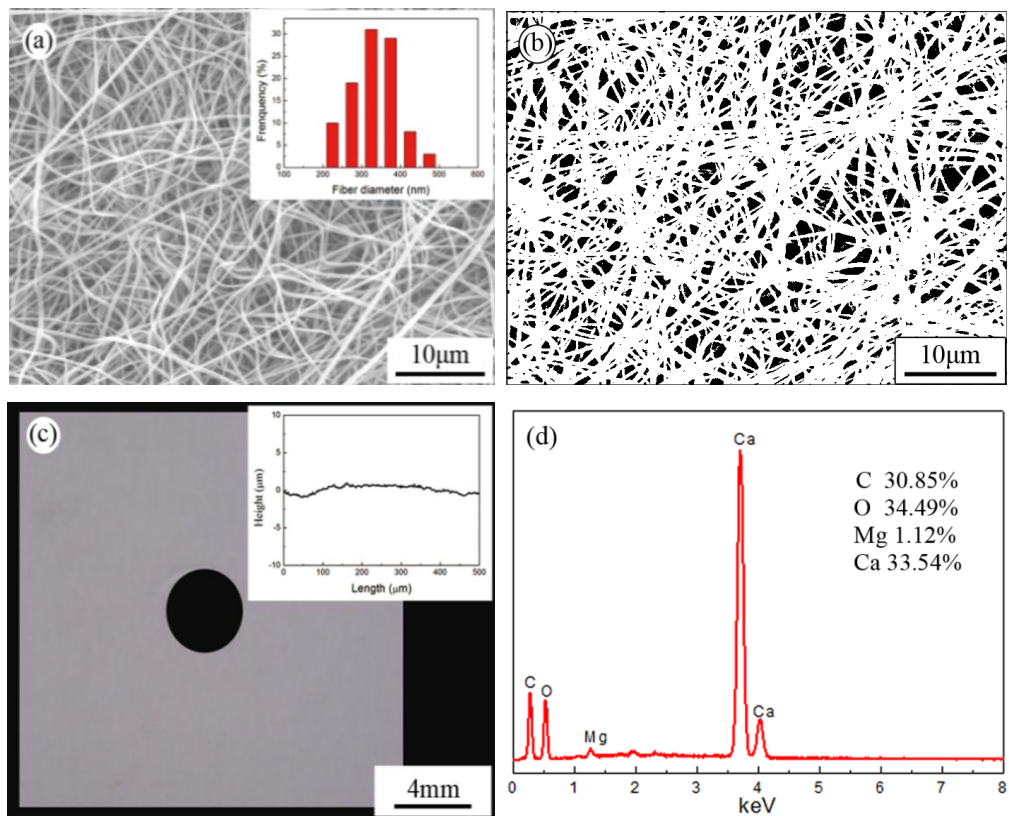


Figure 6.1 The morphology of the contact surface of electrospun PVDF (a, b) and surface composition of the rigid substrate (rigid cardboard) (c, d). SEM image of PVDF membrane (a) shows the fiber diameters fall in around 300-400 nm and the average diameter is 333 ± 59 nm (measured by Photoshop 9.0). In order to estimate the surface area occupied by fibers, electrospun fiber in the image is adjusted to bright field. And the background is changed into dark field. Bright area in (b) occupies 76.97 ± 2.05 % of the total area which shows the projected area fraction at the contact surface about 77 %. The top surface of the rigid cardboard is scanned by surface profiler. Calculated from the scanning curve (c), the valley depth is around 100-600 nm. Elemental analysis (d) of the cardboard surface shows contents of inorganic materials coating. The percentage of Ca, C and O are 33.54 wt%, 30.85 wt% and 34.49 wt%, respectively.

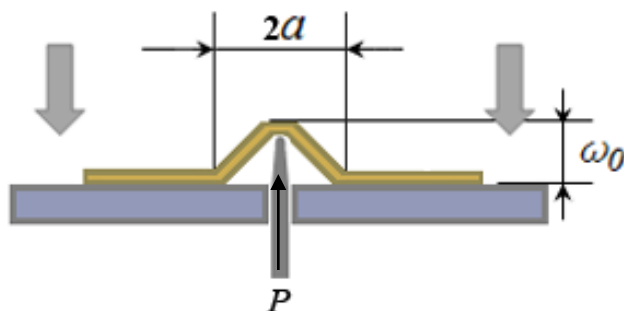


Figure 6. 2 A schematic of SLBT adhesion test.

6.3 Morphology of Electrospun PVDF Membrane and Rigid Substrate

Figure 6.1 (a) shows an SEM micrograph of electrospun PVDF membrane. The constituting fibers possess a diameter in the range of 333 ± 59 nm and are quite uniform in quality in the sample mesh. Fiber diameter is measured from SEM micrograph by Photoshop 9.0. Though forward light scattering [166] and spectral interferometry [167] were also used in fiber diameter measurements, SEM is the most direct and simplest way to assess the electrospun fiber diameter. Fiber fraction of electrospun PVDF membrane is measured from a SEM micrograph. There are about 1.81 fibers per μm on the surface. Image of fibers shown in Figure 6.1 (b) is adjusted to a bright against dark background by Photoshop and measured by ImageJ 1.44b. Fiber occupied area fraction at the contact surface is roughly 77 % and is fairly constant over the surface area. Here the fraction is the projected area fraction (PAF). PAF is only used to estimate the projected surface occupation, and not used for any further calculation. Figure 6.1(c) shows the surface of a cardboard substrate. The top surface is examined by the surface profiler (Dektak150, Bruker). Profile scan [Figure 6.1(c)] shows the peak to valley depth around 100-600 nm and

an arithmetic average roughness, $R_a \sim 128$ nm. The substrate surface is coated by inorganic materials and thus provides a plane for membrane adhesion. Energy dispersive spectroscopy (EDS) integrated with the SEM is used to analyze the elements of cardboard, see Figure 6.1(d). These elements include calcium (Ca), oxygen (O), carbon (C) and a small trace of magnesium. The percentage of Ca is 33.54 wt%. O₂ and C constitute 30.85 wt% and 34.49 wt% of the sample, respectively. The results of elemental analysis yield the high content of Ca at the surface of the cardboard. It shows the inorganic coating exists on the top surface. The SEM and EDS data indicate the cardboard is an ideal rigid substrate for dry adhesion examination.

6.4 Evaluation of the Adhesion Energy

The setup of SLBT test, as discussed in section 4.3, is sketched in Figure 6.2. The debonding in the first 12s of loading is recorded by video. The central deflection is simultaneously recorded and the debonding blister radius measured. Figure 6.3 shows a monotonic increase of $w_0(a)$ along with the side view of a blister. The plots (w_0, a) are summarized in right side of Figure 6.3. From 0 mm to 2 mm of central deflection, it shows a linear elastic behavior and yields a slope of (w_0/a) . The data justify the assumption of linear elastic deformation. And the transition point from linear elasticity to plastic deformation is marked on Figure 6.3. The data beyond the 2 mm central deflection are not used for calculation of adhesion energy.

An average of 10 measurements is taken for each sample, and the results are summarized in Table 6.1. Figure 6.4 shows the simultaneously applied force as a function of shaft displacement. At the beginning part of $P(w_0)$ curves, it shows a straight linear trend and justifies linear elastic deformation of electrospun membrane. The central deflection exhibits a linear increase with the increase of external load. At about $w_0=2.0$ mm, the curves show a “yield point”. Because of the particular fibrous structure of electrospun PVDF membrane, the fibers could produce a slight slip at membrane center under large applied load. It results in the “yielding” effect. At initial loading with $w_0 < 0.8$ mm, a consistent linear $P(w_0)$ is shown in the consecutive measurements. It is however noted that no obvious permanent deformation is observed in the video recorded. Values of the slope (P/w_0) are summarized in Table 6.1.

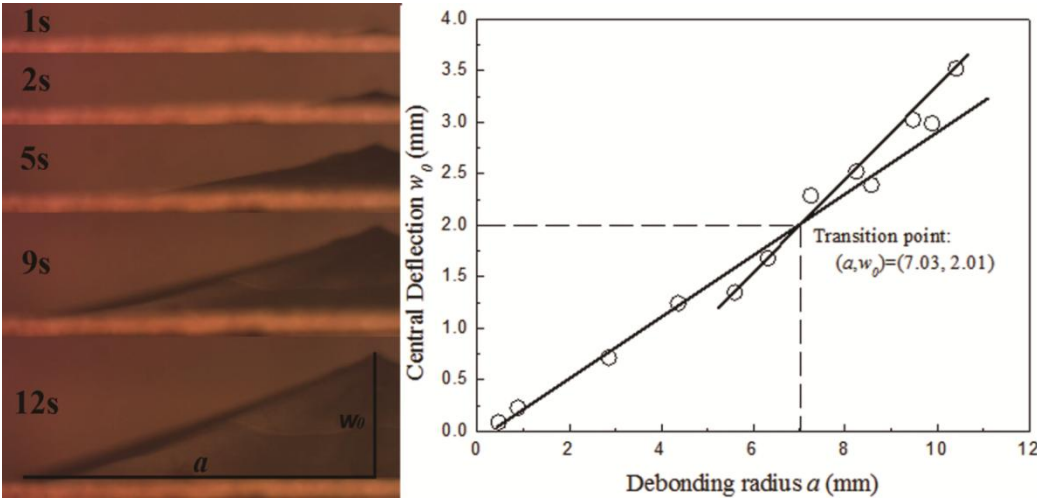


Figure 6.3 Debonding between electrospun PVDF membrane and rigid substrate in SLBT. The debonding is observed by optical microscope. An approximate single conical blister of electrospun membrane is formed in testing and it shows that the elastic response of the membrane appears in the tests [left side of the Figure]. The central deflection and debonding radius of the electrospun membrane blister within 10 s are measured by video

recording and analyzed by Photoshop 9.0 to get the slope of w_0/a curve [right side of the Figure].

Combining the data from Figure 6.3 and Figure 6.4, the instantaneous P - w_0 - a relation is obtained, which is used to determine the work of adhesion using Equation 5.24. and $W = 206 \pm 26$ mJ/m², as shown in Figure 6.5. In Equation 6.1, the strain energy release rate G takes into full account of the strained fibers, the elastic energy associated with stretching and the fiber orientation. This is how the thermodynamic energy balance of the SLBT is formulated in our earlier work [149]: input energy comes from the applied load multiplied by the shaft displacement, $F \cdot \delta y$, and the output energy comprises membrane stretching, $\sigma \cdot \delta \varepsilon$ and creation of new surface (i.e. delamination), $\gamma \cdot \delta A$, i.e.

$$F \cdot \delta y = \sigma \cdot \delta \varepsilon + \gamma \cdot \delta A \quad \text{Equation 6.1}$$

Our experiments do not show any hysteresis in loading-unloading-reloading in the multiple delaminations in the same sample, see Figure 6.3. Therefore the adhesion-delamination is purely elastic without any plastic yielding or energy absorption by fiber orientation. When the circular delamination front proceeds in a quasi-static manner, electrospun fibers remain stretched throughout. $G = W$ reflects the true adhesion at the film-substrate interface. Before this research, no other adhesion methodology for electrospun polymers was reported. This analysis provides fruitful insights in characterizing the adhesion energy of electrospun fiber membrane. It complements our earlier work on measuring the adhesion work and strength between two electrospun single fibers in a cross-cylinder geometry.

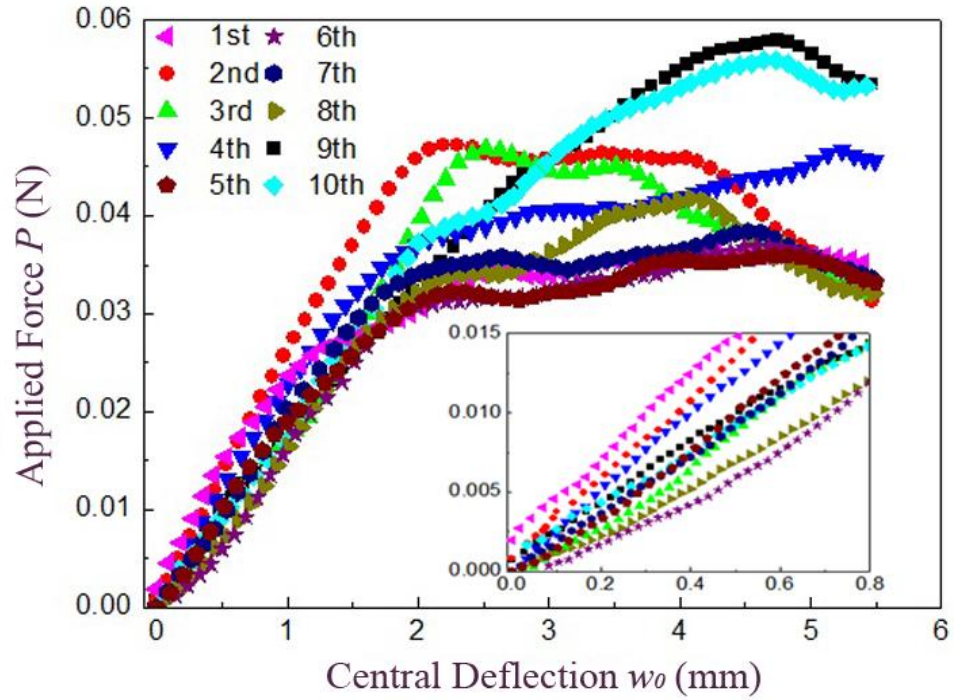


Figure 6.4 Externally applied force plotted as a function of blister central deflection for electrospun PVDF membrane. An average of 10 measurements is taken in sequence to show the relations between applied force and central deflection. The initial parts of P-w0 curves exhibit a stable debonding between PVDF membrane and rigid substrate.

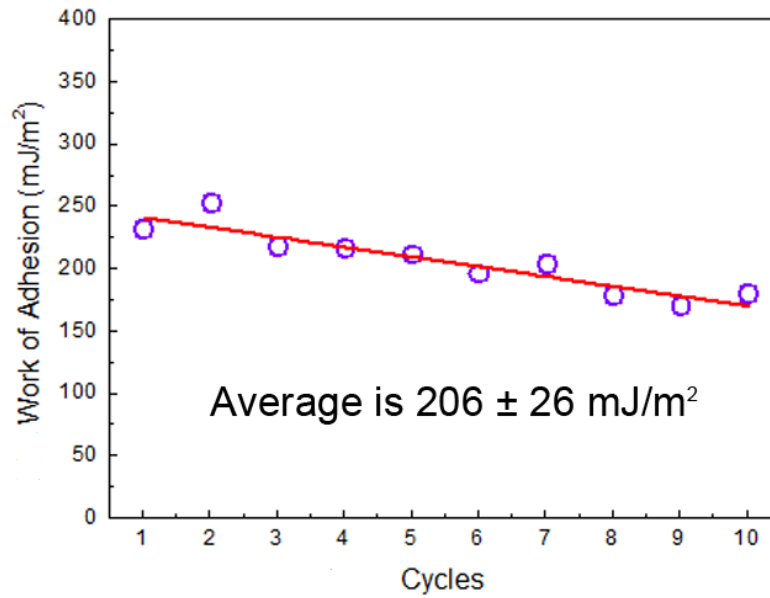


Fig .6.5 The work of adhesion between electrospun membrane and rigid substrate. The adhesion energy shows a slight decrease through SLBT. The average of adhesion energy between electrospun PVDF and rigid cardboard is 206 ± 26 mJ/m².

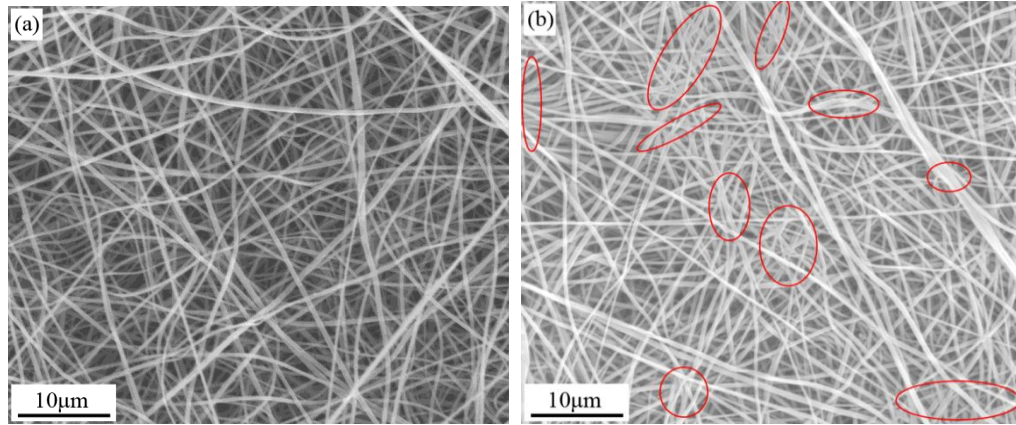


Figure 6.6 SEM micrographs of PVDF membranes before (a) and after (b) blister tests. Before blister tests, uniform fiber could be observed at the surface of electrospun PVDF membrane (a). After the blister test, some fibers are flattened slightly and fuse together at the intersections (b, circled by red ellipses). A roller was utilized to fix the PVDF membranes onto cardboard papers. After ten measurements, the fiber morphology changes slightly due to excessive pressure. It leads to slight decrease in adhesion energy of the PVDF membrane.

In Figure 6.5, gradual degradation of the adhesion energy is observed. After 10 trials in blister tests, the work of adhesion slightly decreases by 17.4% in comparison to the average value. In the blister test, a steel roller is used to press the PVDF membrane onto the rigid cardboard. This is to assure that fibrous membrane attach more completely onto the top surface of the substrate. After repeated pressings, some fibers are squashed to slight deformation. Some fibers fuse together, as circled in Figure 6.6(b). The change in fiber morphology leads to reduced surface area for adhesion work.

Table 6. 1 The slopes of w_0 - a and P - w_0 curves.

Number of cycles	Thickness h (mm)	P/w_0 (N/m)	w_0/a (m/m)
1	0.01	18.8	0.337
2	0.01	25.7	0.352
3	0.01	22.5	0.349
4	0.01	22.8	0.345
5	0.01	17.9	0.355
6	0.01	24.6	0.344
7	0.01	19.1	0.344
8	0.01	22.0	0.341
9	0.01	22.0	0.335
10	0.01	22.6	0.3431

Figure 6.7 compares the electrospun PVDF membrane with cast PVDF film based on 3-D AFM topographic imaging data and surface profiling. Evidently, the electrospun PVDF membrane exhibits an uneven surface morphology with highs and lows as indicated by Figure 6.7(a). In contrast, in Figure 6.7(b) the cast PVDF film is significantly smoother. When cast PVDF film is used in SLBT, the adhesion energy is low and hard to be recorded with the given load cell sensitivity. The value is 10-30 mJ/m², which is almost the same as the standard deviation of the adhesion energy observed in membranes. The low adhesion energy between cast film and rigid substrate is consistent

with the low value reported in literature [168]. The adhesion energy of cast poly(vinylidene fluoride-trifluoroethylene) copolymer (PVDF-TrFE) film against mica sheet reported by Benz and coworkers is only $\sim 20 \text{ mJ/m}^2$.

The main reason for the relatively high adhesion energy of electrospun membrane in comparison to cast film is an actual contact area increase and an additional interlocking effect. Electrospun fibrous materials are composed by ultrafine polymer fibers. Because of the small diameter and excellent flexibility, electrospun fibers can easily meander around surface asperities to provide effectively large area of contact [169]. Due to the high fiber flexibility, high adhesion energy was assessed between electrospun fibers in Wong and co-workers' previous work [169]. Flexible fiber morphology provides a rough surface of electrospun membrane.

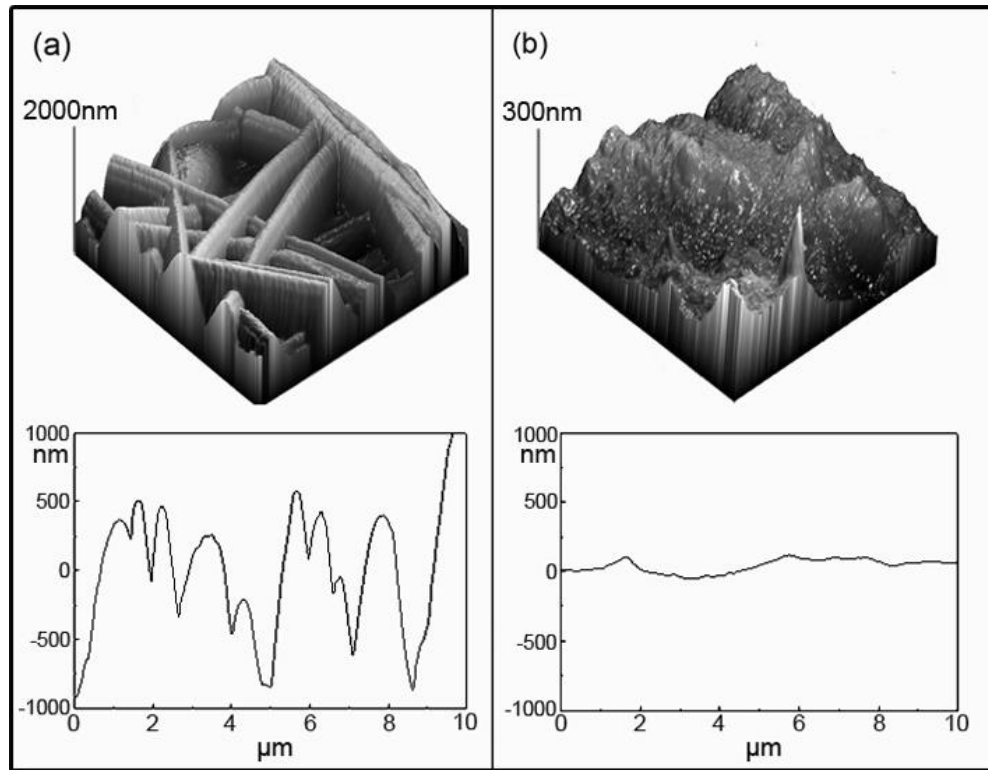


Figure 6.7 3-D AFM topographic imaging and surface profiling of (a) electrospun PVDF membrane and (b) a cast PVDF film . Electrospun PVDF membrane exhibits fiber morphology and a uneven surface. The membrane produces additional cylindrical contact area against the rigid substrate thereby enhancing adhesion energy. The cast film only shows a relatively smooth and featureless surface in comparison to the membrane. The actual contact area between cast film and the rigid substrate is lower.

The surface roughness could form an effective interlocking effect with the substrate to induce high adhesion energy [169]. The interlocking effect, which includes "debonding" and "pull-out" energies, is additional to fiber stretching, bending and surface delamination, and contributes to the overall adhesion energy that is, by definition, normalized against the planar surface area, in accordance with Equation 6.1. These additional mechanisms are not substantially observed in adhesion between single fibers. All the previous results [8] show the adhesion energy of electrospun membrane against substrate could be several hundred mJ/m^2 and much higher than the adhesion energy

derived from cast films. In our experiment, the adhesion energy between electrospun PVDF membrane and rigid substrate is found to be $206 \pm 26 \text{ mJ/m}^2$. On the contrary, cast film does not have fibrous structures. The smooth and rigid surface of cast films leads to a lower contact area, little fiber stretching and bending, and thus low adhesion energy.

Stein and co-workers [170] utilized parallel micro-scale grooves to increase the interfacial adhesion between two polymer plates. The custom-made grooves on one of the polymer plates produced a rough surface, which greatly enhances adhesion. When the other polymer plate was made in contact with the rough surface, the contact area between the two polymer plates was increased. As a result, interfacial adhesion was significantly increased. In Stein's work, the increase of interfacial toughness was used to show the increase of interfacial adhesion. The value of interfacial toughness increased from 8 J/m^2 to $145\text{-}170 \text{ J/m}^2$, which is an 18-fold increase, by use of the grooved surface. Their work evidences the notion that a fibrous morphology, which provides membrane surface rugosity, enhances interfacial adhesion.

6.5 Comparison of Elastic Modulus

Elastic modulus is deduced using the P - w_0 - a data and is found to be $E = 23.42 \pm 2.69 \text{ MPa}$ using Equation s 3.24 and 3.25 [see Table 6.2]. Standard tensile tests yields consistent values, $E = 23.04 \pm 3.70 \text{ MPa}$. The results exhibit convincing evidence to the effect of elastic response of PVDF membrane taken place in SLBT. It can be concluded that the elastic analysis presented herewith is reasonable to obtain the value of adhesion energy. To verify the elastic modulus, we compare the values obtained from SLBT to

those from standard tensile tests. The results are highly comparable as indicated in Table 6.2. This consistency evidences the validity of Equation 5.24 and thus the mechanics and mechanisms assessed by SLBT reported herewith.

Table 6.2 Comparison of elastic moduli between SLBT and tensile tests.

Shaft-Loaded Blister Test			Tensile Test		
Number of cycles	Elastic modulus (MPa)	Average (MPa)	Samples	Elastic modulus (MPa)	Average (MPa)
1	21.1		1	22.76	
2	26.5				
3	23.6		2	26.69	
4	24.3				
5	18.1	23.42±2.69	3	17.72	23.04±3.70
6	26.5				
7	20.6		4	21.63	
8	24.0				
9	25.0		5	26.38	
10	24.5				

6.6 FEA Results Comparison

The numerical model as discussed in Chapter IV is used to evaluate the SLBT results. The adhesion energy is given as 206 mJ/m^2 , which is obtained from the experimental work. The relationship of applied load (P) vs central deflection (w_0) is plotted in Figure 6.8. The hollow black circles in Figure 6.8. illustrate the numerical data computed from FEA model. The trend for the FEA data matches the trend of

experimental data. The applied force linearly increases at the beginning, and then reach a stale plateau. The transition point locates at ~ 2 mm central deflection. The ratio of applied load to central deflection (P/w_0), 22.81 N/m, appear larger than experimental data which is 21.8 ± 2.51 N/m. The slight difference can be attributed to extra energy consumed during experiment. The extra energy consuming may reason from fiber re-orientation or plastic deformation during the experiment test.

The numerical results of debonding radius vs. central deflection are shown in Figure 6.8. The increasing trend is nearly the same as the trend of experimental results, and unstable increase is observed when the central deflection is larger than 2mm. The ratio of central deflection (w_0) to debonding radius (a) is calculated from numerical data (see Figure 6.9), as 0.376, which is 9.1% larger than the experimental results, which is 0.3445. Computing by using of the governing equation (Equation 5.24), the total work of adhesion can be obtained as 256.1 mJ/m^2 . Comparing the numerical results with experimental results, we can find these two results are very close to each other, and thus the SLBT is confirmed to be an effective tool to measure the adhesion energy between electrospun membrane and rigid substrate.

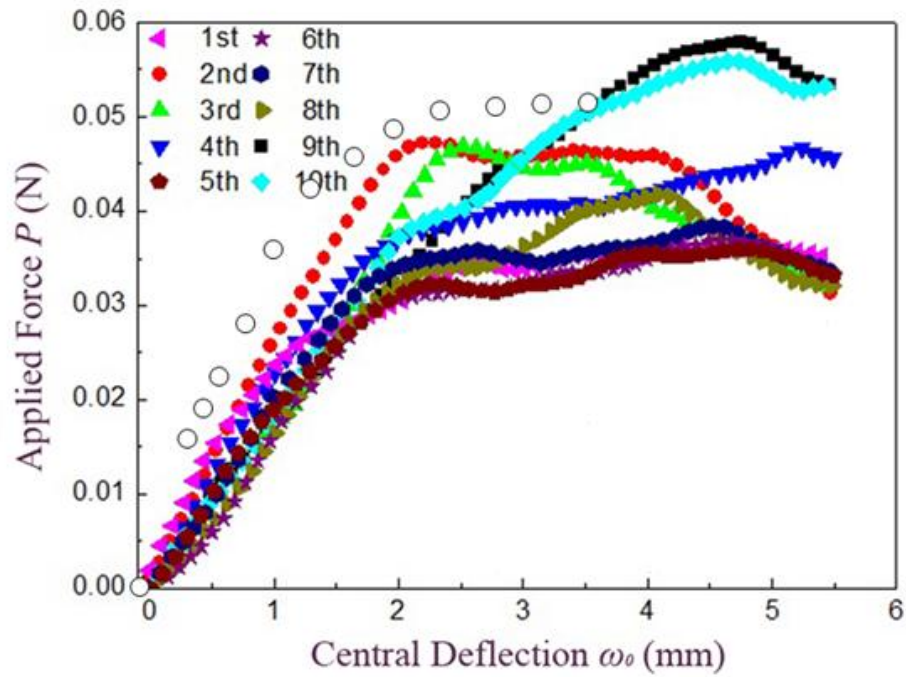


Figure 6.8 Comparison of data from numerical model and experimental SLBT test. Hollow circles illustrate data from numerical modeling.

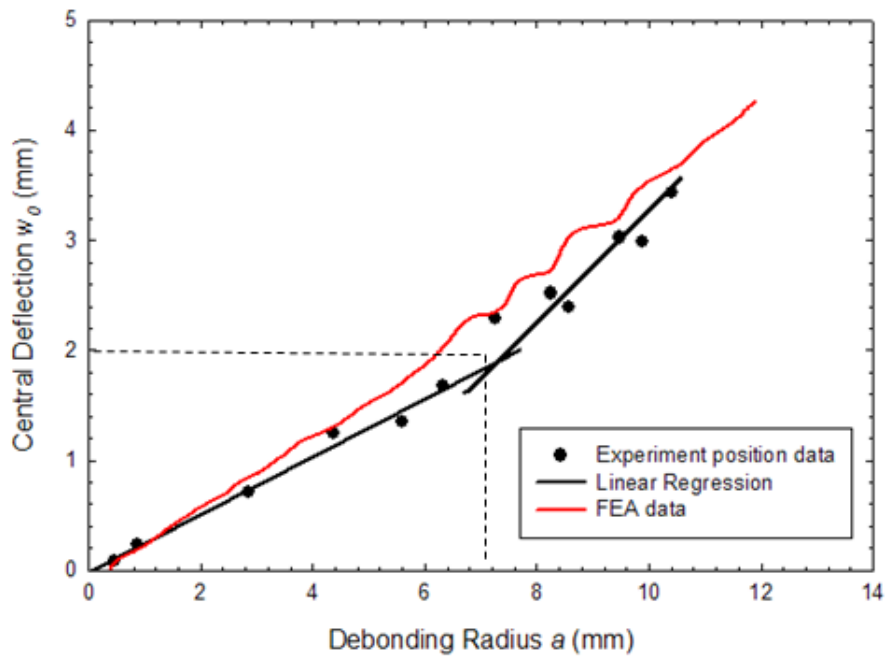


Figure 6.9 Comparison of data from numerical model and experimental SLBT test.

6.7 Conclusions

A shaft-loaded blister test was used to directly measure the adhesion energy of electrospun PVDF adhered onto a rigid substrate. The work of adhesion is found to be $206 \pm 26 \text{ mJ/m}^2$ from ten repeated tests. AFM images exhibit significantly varied highs and lows on a surface profile in the electrospun membranes. The membrane surface asperities increases the actual contact area between polymer fibers and inorganic substrate hereby a high adhesion energy is obtained. Our results, albeit novel in electrospun polymer membranes, are consistent with earlier findings of enhanced interfacial toughness and adhesion on grooved surfaces performed by Stein, Garrett and coworkers [170]. Our electrospun PVDF membranes exhibited a linear elastic deformation at a small external load, and the elastic modulus is found to be $23.42 \pm 2.69 \text{ MPa}$, which is consistent with a value obtained from a standard tensile test. Further FEA study confirms the results from experimental work. Fruitful insights could be gained from this study in performing future adhesion measurements between electrospun polymer membranes. The sub-micrometer randomly oriented fiber mats present potential for adhesion applications.

CHAPTER VII

EFFECT OF FIBER DIAMETER ON ADHESION ENERGY OF ELECTROSPUN MEMBRANE

7.1 Introduction

Adhesion between electrospun membrane and rigid substrate is studied in the previous chapter. SLBT adhesion test is proved to be an effective methodology to determine the adhesion energy. More is focused on deeper study of relationship between membrane's materials property and adhesion property.

Size effect on adhesion properties under macroscopic scale were reported by researchers [171-174]. Mechanical interlocking is reported as the dominate adhesion mechanism. However, under micro-scale contact, van der Waals interaction is always the dominate factor [3,6]. Little quantitative study on size effect of adhesion property of electrospun membrane was reported. In this chapter, we will study the relationship between fiber size and adhesion energy, and discuss the mechanism of size effect.

7.2 Sample Preparation

Electrospinning is conducted at ambient temperature, solution feed rate 0.3mL/h and applied voltage 10 kv. Duration of electrospinning process is 10 hours. Then PVDF membrane was dried in vacuum oven at 50 °C for 12 h before used in adhesion test. The

samples fabricated from condition A-F are also named Sample A-F, respectively. Six formulations of PVDF solutions are shown below, from condition A to condition F. Under condition *F*, a stable electrospinning procedure cannot be reached and maintained. Therefore no sample F is produced and no discussion is related to sample F in the future.

Table 7.1 Solution preparation methods of Sample A-F.

	Solvent ratio (DMF/Acetone)	Solution Concentration (g/ml)	Diameter(nm)	Projected Area Fraction (%)
Sample A	7/3	0.15	201±86	84.67±2.30
Sample B	7/3	0.17	387±65	77.81±2.76
Sample C	5/5	0.15	733±154	79.20±1.00
Sample D	5/5	0.17	1835±653	84.69±5.76
Sample E	7/3	0.20	2724±587	83.32±6.43
Sample F	5/5	0.20	N/A	N/A

7.3 Experimental Work

Morphology of five electrospun PVDF membranes is characterized by scanning electron microscopy (JEOL JSM-6510LV). Before imaging, samples are coated with argentineum by sputter coater (K575x, Emitech) for 1.5 min at 55 A. Average fiber diameter and projected area fraction (PAF) of electrospun fibers are determined from SEM micrographs by software ImageJ 1.45s

PVDF membrane is cut into $40 \times 10 \text{ mm}^2$. Tensile test on PVDF membrane is performed firstly. PVDF membrane is mounted on tensile tester (Thorlabs, MTS 25-Z) with a gauge length of 20 mm. the tests speed is consistent with the speed of adhesion tests, which is 0.33mm/s. Five repeated tests for each sample are performed to ensure consistency.

PVDF membrane is cut into $30 \times 30 \text{ mm}^2$ for adhesion measurement. Rigid substrate is prepared from cardboard with inorganic coating. In order to make good contact, a lightweight plastic roller ($w \approx 100 \text{ g}$) was used to roll over the membrane onto the substrate to squeeze air bubbles between membrane and substrate. SLBT adhesion tests are performed for sample A-E, as shown in Figure 7.1(a) and (b), which use the same home-made fixture as discussed in Chapter V. For each set of sample, five tests are repeated to ensure the accuracy of the results.

Sample C is chosen to perform adhesion tests with different thicknesses. In order to create samples with different thicknesses, multi-layers of sample C are stacked, and pressed by the plastic roller. Samples with 1 layer, 2 layers, 4 layers, 8 layers and 16 layers are used to evaluate the thickness effect. The samples with different thicknesses are mounted to perform SLBT adhesion tests. Five repeated tests are performed for each sample.

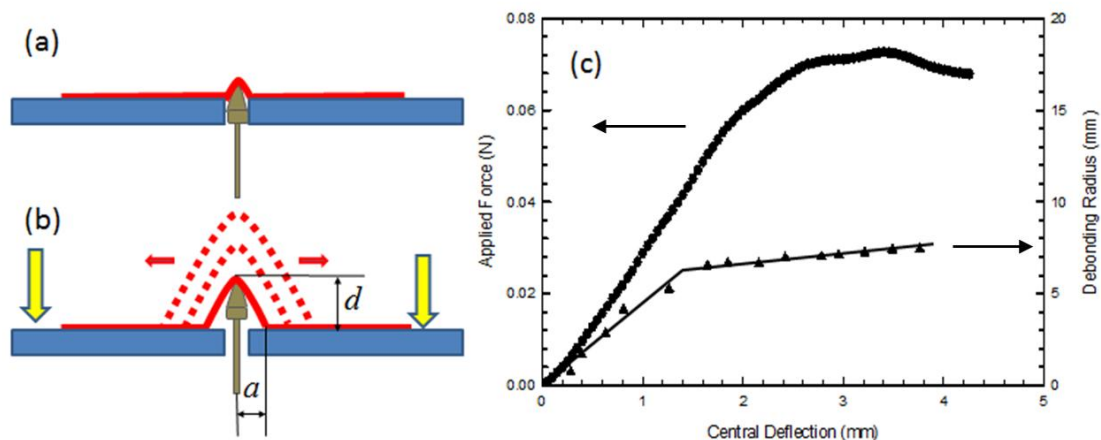


Figure 7.1 (a) The setup of SLBT test, the electrospun membrane is represented in red color, and the blue color shows the rigid substrate, (b) The test procedure of SLBT is illustrated, the membrane will keep debonding when a displacement is applied vertically. (c) The relationship between applied force and central deflection, central deflection and debonding radius are obtained, which are the key parameters to calculate the adhesion energy.

7.4 Morphology of Electrospun Membranes from Different Solutions

SEM image of Sample *A-E* are shown in Figure 7.2 (a-e) respectively. All of the five samples show smooth surfaces and uniform fiber diameters. No bead and irregular fiber are founded. PAF of sample *A-E* can be found in Table 7.1, which arrange from 77.81% to 84.69%. Since fiber fraction does not make significant differences, further comparison among Sample *A-E* is meaningful.

Fiber diameter distribution is shown in Figure 7.2(f). Condition *A* yields thinnest fibers (201 ± 86 nm), followed by condition *B* (387 ± 65 nm), condition *C* (733 ± 154 nm), condition *D* (1835 ± 653 nm) and condition *E* (2724 ± 587 nm). Clearly dilute solution can produce thin fibers. Other researchers also adopted the polymer concentration control in order to control output fiber diameters [157-159]. 0.15 g/ml solution produces 201 nm

and 733 nm fibers, and 0.17 g/ml solution produces 387 nm and 1835 nm fibers, and 0.20 g/ml solution produces 2724 nm fibers. Boiling point of Acetone (56.3°C) is much lower than DMF (153 °C), therefore decreasing DMF/acetone ratio can increase the rate of evaporation. Researchers demonstrated higher rate of evaporation during electrospinning can produce thicker fiber [160-162]. In our experiment, under same polymer concentration, lower DMF/acetone ratio significantly increases the fiber diameter. For 0.15 g/ml solution, when DMF/acetone ratio decreases from 7:3 to 5:5, fiber diameter increases from 201 nm to 733 nm. Similarly, Fiber diameter increases from 387nm to 1835nm when decreasing DMF/acetone ratio from 7:3 to 5:5, corresponding to 0.17 g/ml solution.

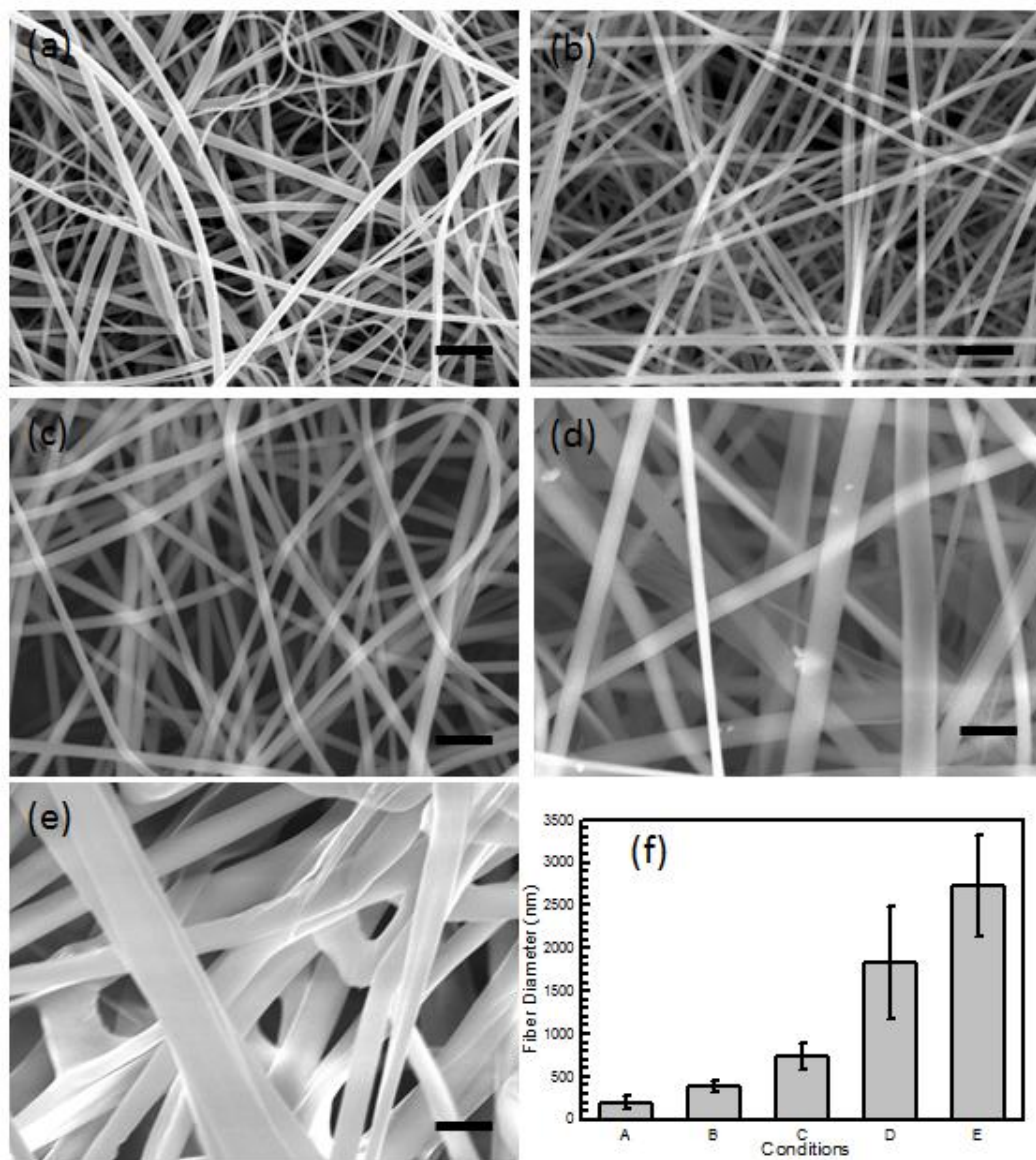


Figure 7.2 SEM images (a)-(e) corresponding to sample A-E. (f) illustrates fiber diameter distribution. From sample A to sample E, fiber diameter gradually increases. Scale bar is 5 μm .

7.5 Effect of Fiber Diameter on Tensile Properties

Sample A-E's stress-strain curves are shown in Figure 7.3. Each curve consists of three different regions. At the initial region, stress increases linearly, followed by a transition point, stress linear increases at a different slope. At the end, curve becomes instable, and drops down due to materials fracture. Elastic moduli are calculated from the initial region, because only material elastic deformation happens at this stage. After passing the transition point, the fibers begin to re-arrange, and the joints between fibers begin to be break, therefore, the slope of the curve changes. The ultimate tensile strength is reached around the fracture point. The finest fibers possess the highest ultimate tensile strength at 3.56 MPa.

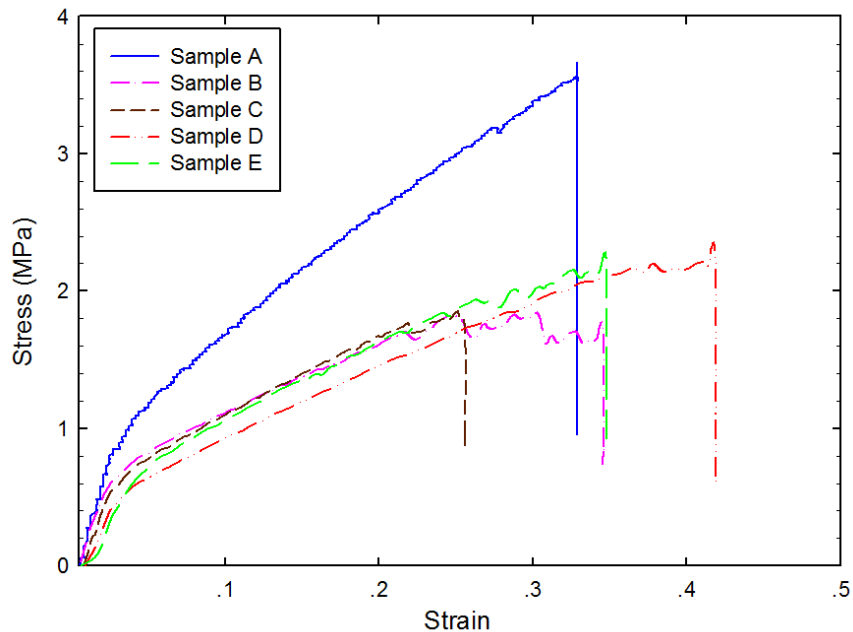


Figure 7.3 The stress-strain relationships for Sample A-E obtain from tensile test.

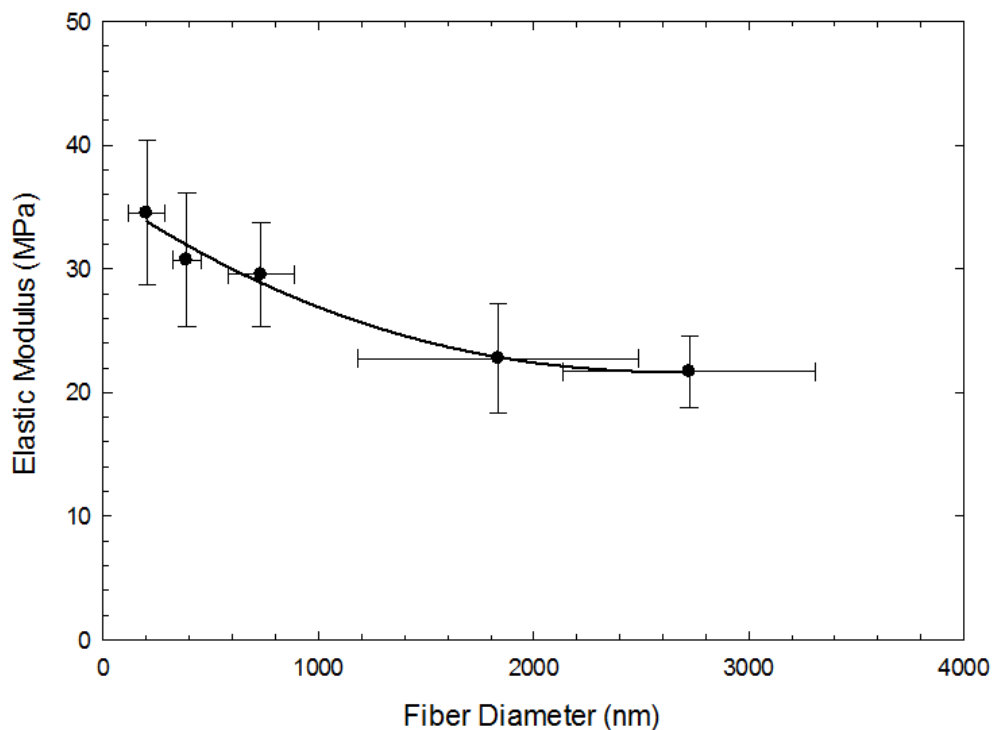


Figure 7.4 Relationship between fiber diameter and elastic modulus of electrospun membrane, as determined by tensile test.

As shown in Figure 7.4, five samples show variable elastic modulus, sample A 34.51 ± 5.84 MPa, sample B 30.72 ± 5.41 MPa, sample C 29.54 ± 4.22 MPa, sample D 22.76 ± 4.47 MPa and sample E 21.69 ± 2.91 MPa. Elastic modulus have a 38.31% increase from sample D to sample A. Researchers have reported thinner fiber always has better mechanical performance. In the case of elastic modulus, thinner fiber possesses high elastic modulus [99,144].

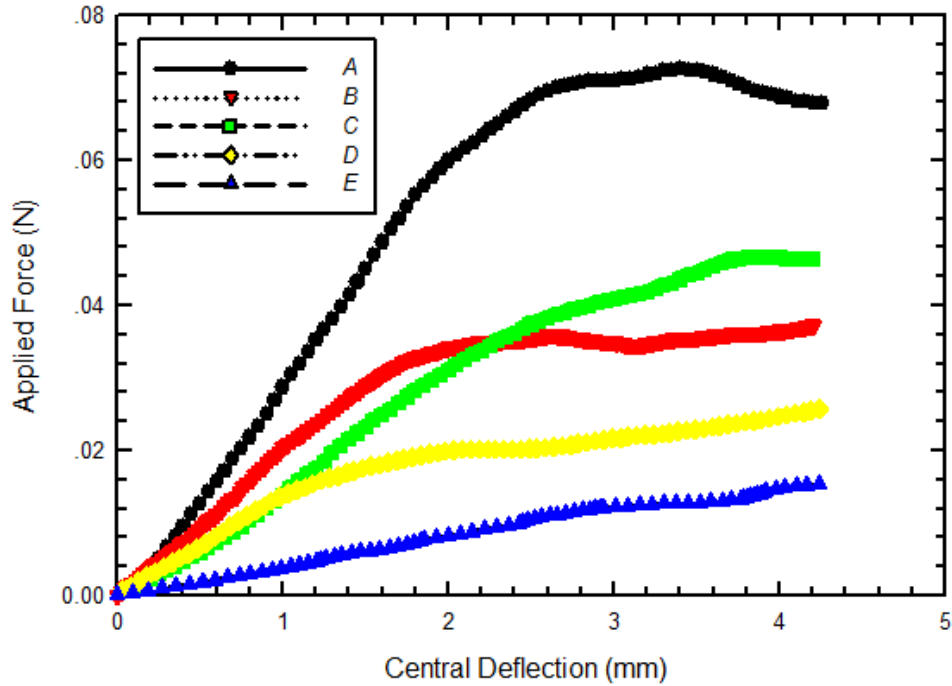


Figure 7.5 Applied load (P) vs. central deflection (w_0) for five samples tests (A, B, C, D, E). Linear elastic deformation occurs for every curve in the initial region. Each test reveals a yielding point around 2mm. The P/w_0 value is obtained from each curve's linear section, 24.6 N/m, 19.4 N/m, 13.7 N/m, 10.5 N/m, 0.35 N/m for sample A, B, C, D, E, respectively.

7.6 Effect of Fiber Diameter on Applied load and Debonding Radius

SLBT tests are performed on membrane samples A-E. Figure 7.5 shows the applied force vs central deflection of five fiber conditions. The initial region of every curve shows linear relationship. Plastic yielding happens to every sample when central deflection reaches 2-3 mm. Only linear elastic region is considered for adhesion energy determination. Following fiber diameter increasing, the value of P/w_0 also shows a gradual increasing trend. From Eqn. 5.24, the value of P/w_0 increasing is directly caused by adhesion energy increase. The value of w_0/a obtained from in-situ deformation profile also increasing with fiber diameter decreasing, such as 0.183 ± 0.017 for 2724 nm fibers,

0.303±0.011 for 1835 nm fibers, 0.0328±0.032 for 733 nm fibers, 0.0344±0.021 for 387 nm fibers and 0.0364±0.034 for 201 nm fibers. Therefore a smaller debonding radius is achieved when fiber diameter decreases. The resistance of debonding becomes larger, which means the interfacial adhesion energy is higher.

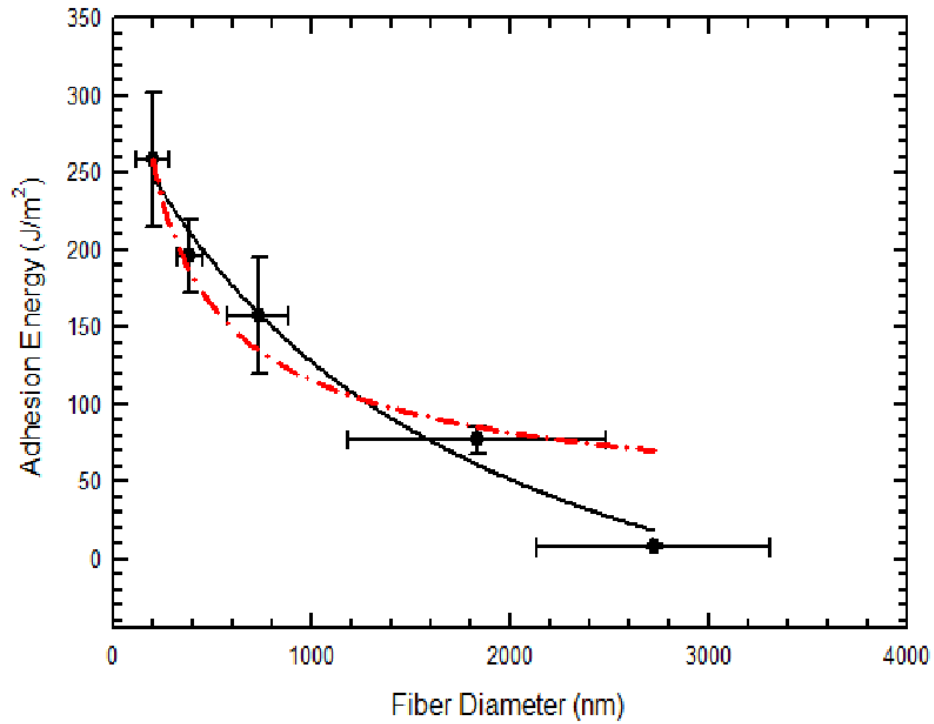


Figure 7.6 Relationship between adhesion energy and fiber diameter for sample A-E. A significant increase trend is established from sample E (8.06 ± 0.71 mJ/m²) to A (258.83 ± 43.54 mJ/m²). The solid line shows a polynomial regression of experiment data. Red dash-dot line illustrates a proportional relationship as $\propto 1/\sqrt{d}$.

7.7 Effect of Fiber Diameter on Adhesion Energy

Relationship between adhesion energy and fiber diameter is shown in Figure 7.6. Obviously adhesion energy is significantly improved from 8.06 mJ/m² (sample *E*) to 258.83 mJ/m² (sample *A*) by decreasing fiber diameter from 2724 nm to 201 nm. Similar size effect is reported on adhesion energy of trenched polymer film/SiO₂ [171]. When the size of patterned polymer line decreases from 12 μm to 2 μm, the adhesion energy increased 50%. The interfacial adhesion energy of sample *D* and *E* with rigid substrate is comparable to the values reported from bulk polymer film, PS film/glass interface [172] 62 mJ/m², polyimide film/aluminum film 86 mJ/m² [173], PCL film/PCL film 53mJ/m² [174]. However, no report was found that bulk polymer material can achieve adhesion energy as high as sample *A* (258.83 mJ/m²) and *B* (196.26 mJ/m²).

Adhesion energy, which is the interfacial fracture resistance, is expected to be determined mainly by van der Waals attractive force (F_{vdw}), which for a single fiber contact can be expressed by [28]:

$$F_{vdw} = \frac{A_h \sqrt{d}}{16D_{vdw}^{2.5}} \quad \text{Equation 7.1}$$

where A_h is materials-dependent Hamaker constant, D_{vdw} is gap distance between fiber surface and substrate, d is the fiber diameter. Therefore, for a given area, a proportional function can be derived between F_{vdw} and fiber diameter d , as shown in Equation 7.2.

$$F_{vdw} \propto \frac{A_h \sqrt{d}}{16D_{vdw}^{2.5}} \times \frac{\rho}{d} = \frac{A_h \rho}{16\sqrt{d}D_{vdw}^{2.5}} \quad \text{Equation 7.2}$$

where ρ is the density of materials. So if fiber density is consistent, vdW force in a given area will inversely proportion of \sqrt{d} . From JKR theory, the work of adhesion (W) can be related with adhesion force (F_{vdw}) by the following equations,

$$F_{vdw} = 3/2\pi RW \quad \text{Equation 7.3}$$

From Equation 7.2 and 7.3, an inverse proportional relationship between the work of adhesion (W) and square-root of fiber diameter (\sqrt{d}) can be established.

$$W \propto 1/\sqrt{d} \quad \text{Equation 7.4}$$

Equation 7.4 is applied to regress experiment data, as shown in the red dash-dot line in Figure 7.6. The trend of the regression line is the same as the trend of experimental data. The data point for sample E is failed to match the regression results. From Figure 7.2(e), the fiber structure is fused and cross-linked, as observed from sample E, which is significantly different from Figure 7.2 (a)-(d). Fusion of fiber will significantly decreases the flexibility of the membrane, and then the stiff membrane can't make good contact with substrate. Therefore, van der Waals force will not dominate the contact mechanics, and the debonding happens due to the poor surface contact.

Adhesion enhancement by size effect was explained by vdW force decreasing, as numerous researchers argued [2,29,175]. For nano-scale fibrous material, surface area to volume ratio increases tremendously with fiber diameter decrease. The actual contact area may be larger than nominal contact area. The fiber surface inside the membrane may also have adhesive contact with substrate. Therefore underestimate of contact area will overestimate adhesion energy. Thin fiber has more flexibility to fit into the surface

asperity of the substrate, therefore a strong adhesion contact is achieved by utilizing thinner fibers.

Table 7.2 Summary of materials properties determined in this study.

	Sample A	Sample B	Sample C	Sample D	Sample E
Diameter (nm)	201±86	387±65	733±154	1835±653	2724±587
Elastic Modulus (MPa)	34.51±5.84	30.72±5.41	29.54±4.22	22.76±4.47	21.69±2.91
Adhesion Energy (mJ/m ²)	258.83±43.54	196.26±23.42	157.03±37.46	76.96±8.85	8.06±0.71
Crystallinity(%)	64.32	58.88	65.02	60.39	55.28
Melting Temperature(°C)	152.67	155.83	151.99	151.24	150.62

Adhesion enhanced by micro mechanical-interlocking [170,176] is another explanation for size dependence. According to substrate's roughness (128nm), when fiber diameter decreases to several hundred nanometers, the smooth substrate will be as rough as fibrous membrane. A rough surface will establish mechanical interlocking with fibers, and then adhesion will be enhanced significantly. Stein and co-workers [170] reported interfacial toughness of two immiscible polymer plates can be improved by scribing grooves on one plate from 8 J/ m² (no groove) to 145 J/ m². According to fracture mechanics, we consider SLBT debonding experiment is a crack propagation process. Mode I (opening mode) possesses weakest adhesive resistance, which is our test mode.

However, mechanical interlocking could cause Mode II (in-plane shear) or Mode III (out-of-plane shear) crack locally. Then total adhesion energy will be enhanced.

7.8 Effect of Membrane Thickness on Adhesion Energy

In order to analyze the influence of thickness on adhesion energy, multilayers of PVDF membranes are attached, and a low pressure applied by a plastic roll to ensure good cohesive contact. Figure 7.7 illustrates the relationships between applied load and central deflection for membranes with different layer. The slope of applied load to central deflection (P/w_0) is summarized in Table 7.3. P/w_0 decrease slightly with the layer increasing. Thin layer membrane also possesses a larger w_0/a value, the plot is shown in Figure 7.8, and the value is summarized in Table 7.3. The adhesion energy is finally obtained from the tested data in Figure 7.7 and Figure 7.8, and summarized in Table 7.3. A decrease trend of adhesion energy with increasing of membrane layer is observed in Figure 7.8

A schematic is used to illustrate the mechanism of thickness effect, as shown in Figure 7.9. If the thickness of the membrane increases, a bending moment will exist inside the membrane. The stored bending energy will consume the interfacial adhesion energy, and then the work of adhesion can be detected by instrument is less. As a result, a thick membrane is observed to detach easier than a thin membrane. Peng and co-workers [177] have done a numerical study on thickness effect on adhesion properties of nanofilm. A decreasing trend of adhesion energy is presented, and they claim the adhesion energy will finally reach a constant if the thickness keeps increase.

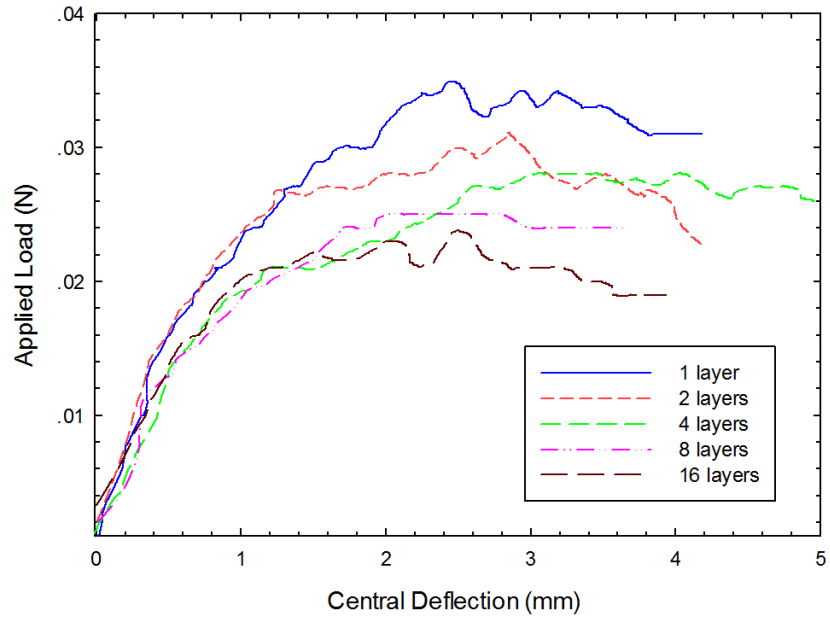


Figure 7.7 Applied load vs central deflection for PVDF membranes with different thickness.

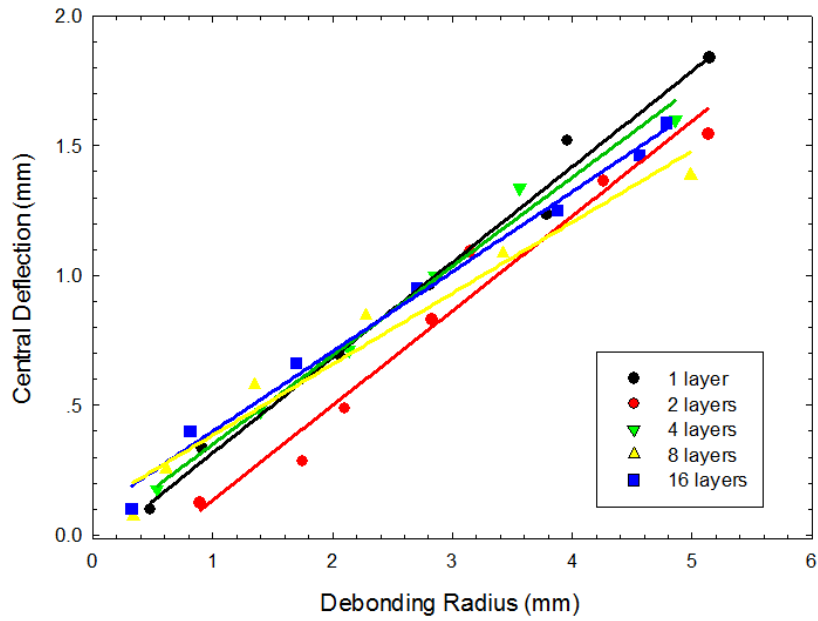


Figure 7.8 Central deflection vs. debonding radius for PVDF membranes with different thickness.

Table 7.3 Adhesion experimental data $P/w_0, w_0/a$ from SLBT tests, and the work of adhesion (W) calculated for membranes with different thickness.

	P/w_0 (N/m)	w_0/a (mm/mm)	W (mJ/m ²)
1 layer	20.82±1.04	0.335±0.021	220.46±34.53
2 layers	20.71±1.74	0.328±0.022	218.84±41.54
4 layers	19.73±0.99	0.295±0.015	158.45±21.52
8 layers	16.45±0.82	0.293±0.024	138.11±25.72
16 layers	15.71±0.86	0.248±0.028	100.46±23.56

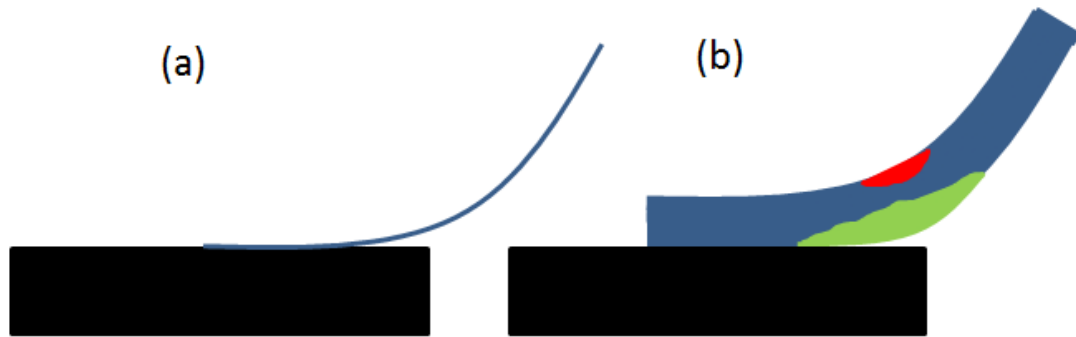


Figure 7.9 (a) Thin membrane has no beading moment, intimate contact can be achieved. (b) Thick membrane has a bending and compression in the membrane, contact is less intimate compare to thin membrane.

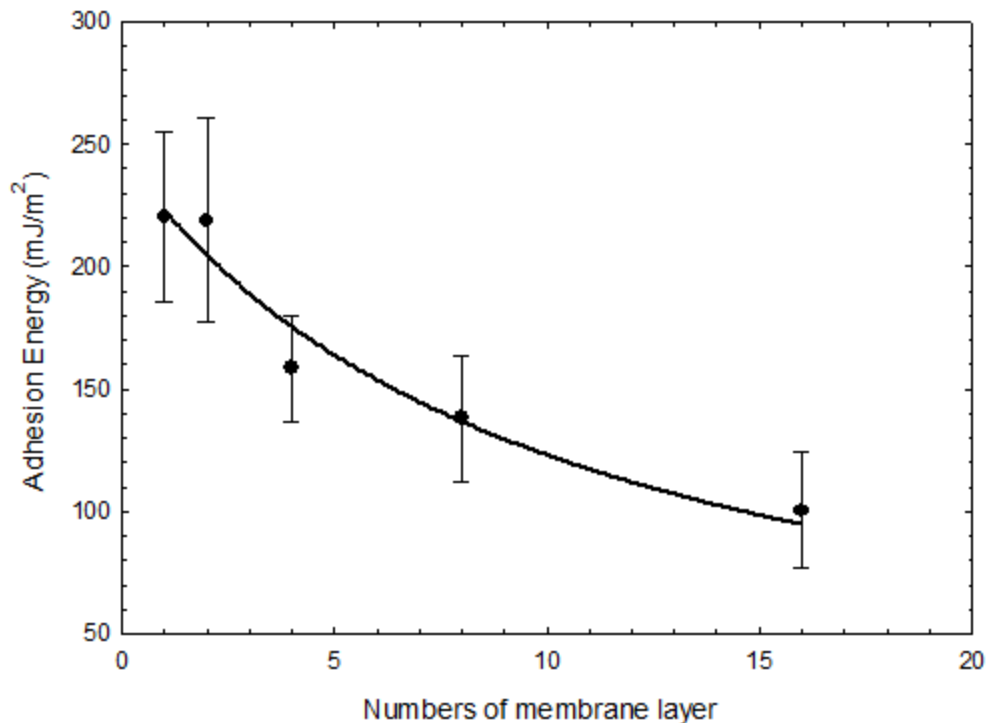


Figure 7.10 Relationship between adhesion energy and numbers of membrane layer.

7.9 Crystallinity of PVDF membranes

DSC is used to show the crystallization of PVDF fibrous membranes. DSC thermograms of PVDF are illustrated in Figure 7.11. The melting temperature and crystallinity are given in Table 7.2. DSC curves show similar endothermic peaks around 165 °C. This is indicative of a consistent melting temperature and thus crystal morphology for fibers across various diameters. Nevertheless, the change in endothermic area under the peak is noteworthy. Considering the melt enthalpy of a 100 % crystallized PVDF, which is 104.7 J/g [178], the degree of crystallinity of our PVDF sample could be estimated, as shown in Table 7.3. Other researchers [8,144] also reported crystallinity increase once the average fiber diameter decrease.

Thinner fiber constrained the molecular in a narrower space during the electrospinning process and thus the crystallization is promoted. The improved mechanical performance, as mentioned in section 7.5 may also be reasoned from the crystallinity increase.

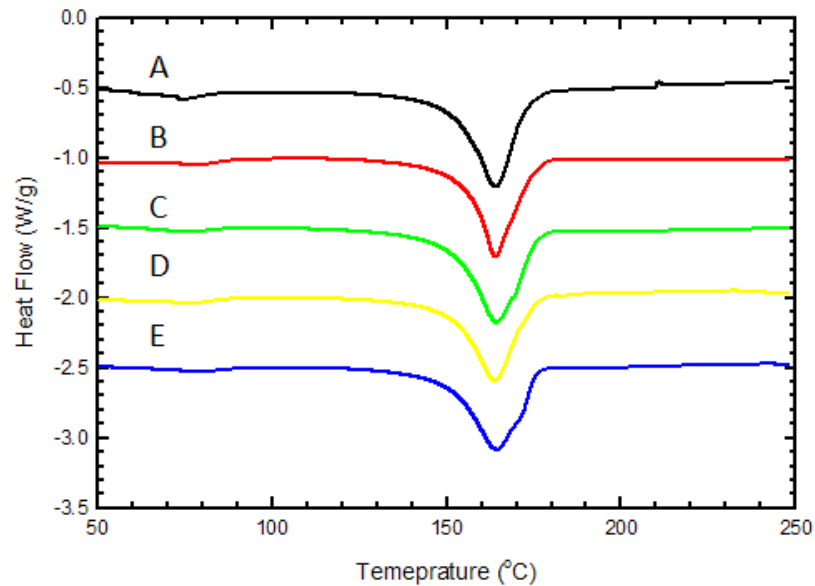


Figure 7.11 DSC thermograms of Sample A-E

7.10 Conclusions

Electrospun membranes fabricated from different solution conditions exhibit different average fiber diameters. Sample A-E is prepared by electrospinning with an average fiber diameter varies from 201 ± 86 nm to 2724 ± 587 nm. The elastic modulus and ultimate tensile strength is improved by decreasing the fiber diameter from 2724 ± 587 nm to 201 ± 86 nm. SLBT adhesion test is conducted to determine the work of

adhesion between PVDF membrane and a rigid substrate. Thinner fiber exhibits higher adhesion energy, and adhesion energy gradually decreases when the fiber diameter increases. Van der Waals forces, surface area to volume ratio and mechanical interlocking may increase when fiber diameter decreases. The three factors could explain the size dependent characteristic of PVDF electrospun membrane. The total adhesion energy is the combined effect of van der Waals forces, large surface area and mechanical interlocking. Van der Waals force is the essential force to adhere the membrane to substrate, large surface areas ensure the adhesion contact is sufficient and mechanical interlocking enhanced the adhesion by locking fibers in the substrate asperities. The thickness effect is investigated by testing membranes with different layers. The adhesion energy decreases when increasing the layers of electrospun membrane. Crystallinity of PVDF is also improved by decreasing the fiber diameter, and this may be a reason for the enhancement of mechanical performance.

CHAPTER VIII

EFFECT OF SUBSTRATE MICROTOPOGRAPHY ON ADHESION PROPERTY OF ELETROSPUN MEMBRANE

8.1 Introduction

The effect of fiber diameter and membrane thickness is evaluated in Chapter VII. Smooth substrate can give an intimate contact with electrospun membrane. The van der Waals attractive force between smooth substrate and electrospun fibers is discussed. However van der Waals attractive force is not the only effective factor on adhesion performance of electrospun membrane. One important factor, the topography of the contact surfaces, cannot be neglected for adhesion research. If the contact substrate is relatively rough, mechanical locking could be possible to lock the contact membrane into the substrate, and thus the adhesion performance is enhanced. McGain and Hopkins [179] conducted research in mechanical locking in the 1920's and they proposed that the cavities, pores, and asperities of the solid surface were the major factor in determining adhesion strength. Surface roughness exists all the time, no matter how well the surface is polished. The area of real contact will change when the surface roughness changes. The actual contact area is directly related to contact force, according to JKR theory. Additionally, when an elastic body contacts with a rigid rough surface, the elastic body can squeeze into asperities of the solid surface. Then mechanical interlocking will play a role in the contact force. Therefore, mechanical interlocking is always adopted to

enhance interfacial adhesion. For instance, good adhesion needs to be achieved between polymer and glass in MEMS (Micro-Electric-Mechanical-System) industry, electroplating or wet etching are used to establish overhanging profile in glass substrate [180]. Random micro-pittings on polymer surface by oxygen plasma treatment [181] has been demonstrated to increase adhesion strength and flexural properties mechanical interlocking [182,183].

Electrospun polymer membrane has been proved to possess good adhesion property when contacting with rigid smooth surface. In this chapter, the effect of substrate roughness on adhesion of electrospun membrane will be tested and discussed. Rough surface can lock the fibers from the electrospun membrane, and higher apparent work of adhesion could be expected.

8.2 Materials Preparation

Electrospun PCL membrane is prepared as discussed in Chapter 4.2. PCL solution is prepared by dissolving the PCL powders in CHCl_3 and DMF (7:3 v/v) at 40-50 °C for 2 h. The concentration of PCL solution is 0.12 g/mL. The prepared solution is then electrospun to fibrous membrane for further adhesion test. The diameters of fibers distributed in the range of 100-500 nm. The thickness of the membrane is $\sim 10 \mu\text{m}$, which is measured by a micrometer caliper.

Sandpapers with different grit size are used as substrate. The material of sandpaper is SiC. Sandpapers are cleaned by ethanol to eliminate possible contamination which may cause by loose SiC particles. Five different sandpapers with different grit size

are used. The sandpapers with grit size of 5 μm , 8.4 μm , 15.3 μm , 30.2 μm and 68 μm are named substrate *a*, substrate *b*, substrate *c*, substrate *d* and substrate *e* respectively (given by manufacturer). The surface morphology of the sandpaper is characterized by Veeco surface profiler.

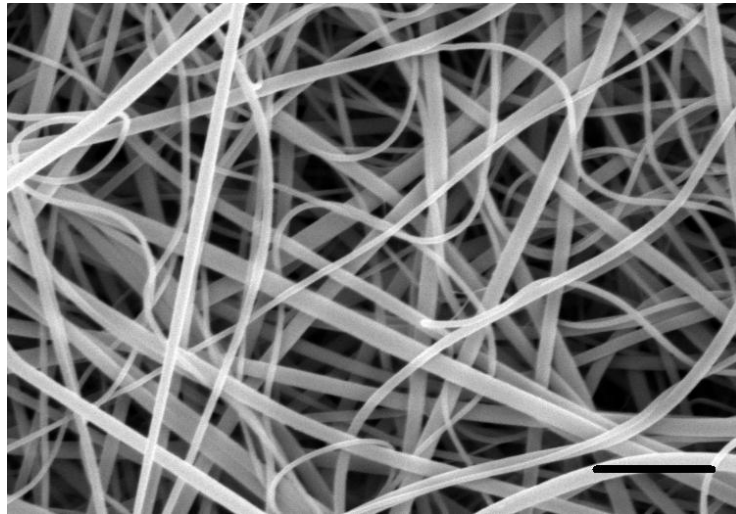


Figure 8.1 SEM image of electrospun PCL membrane, scale bar is 5 μm .

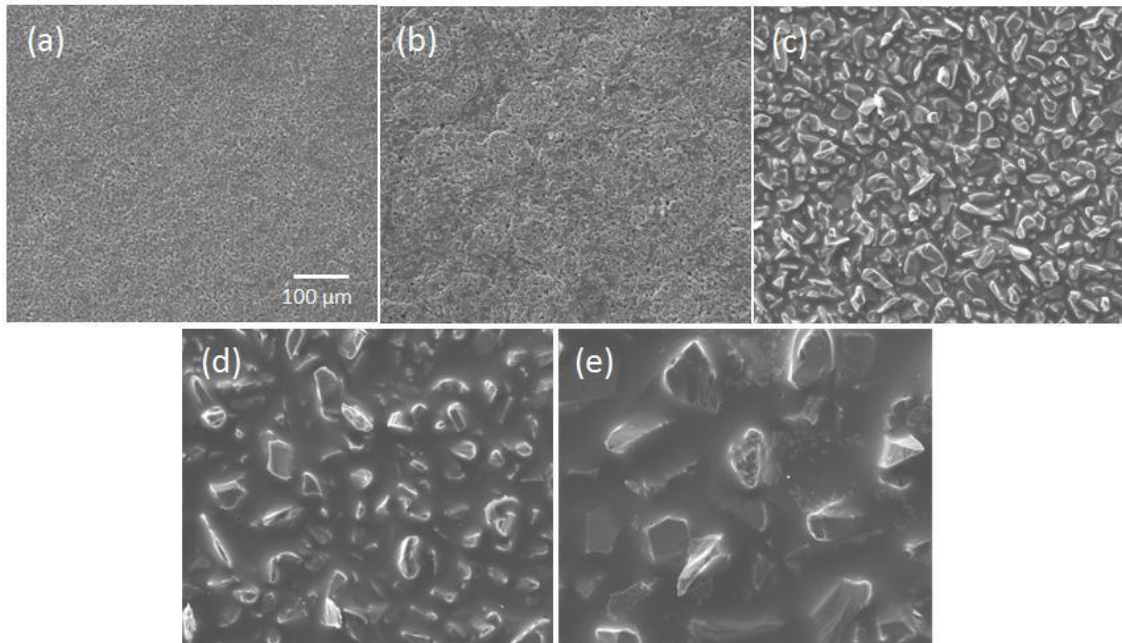


Figure 8.2 SEM images of SiC substrate a-e. The scale bar is 100 μm .

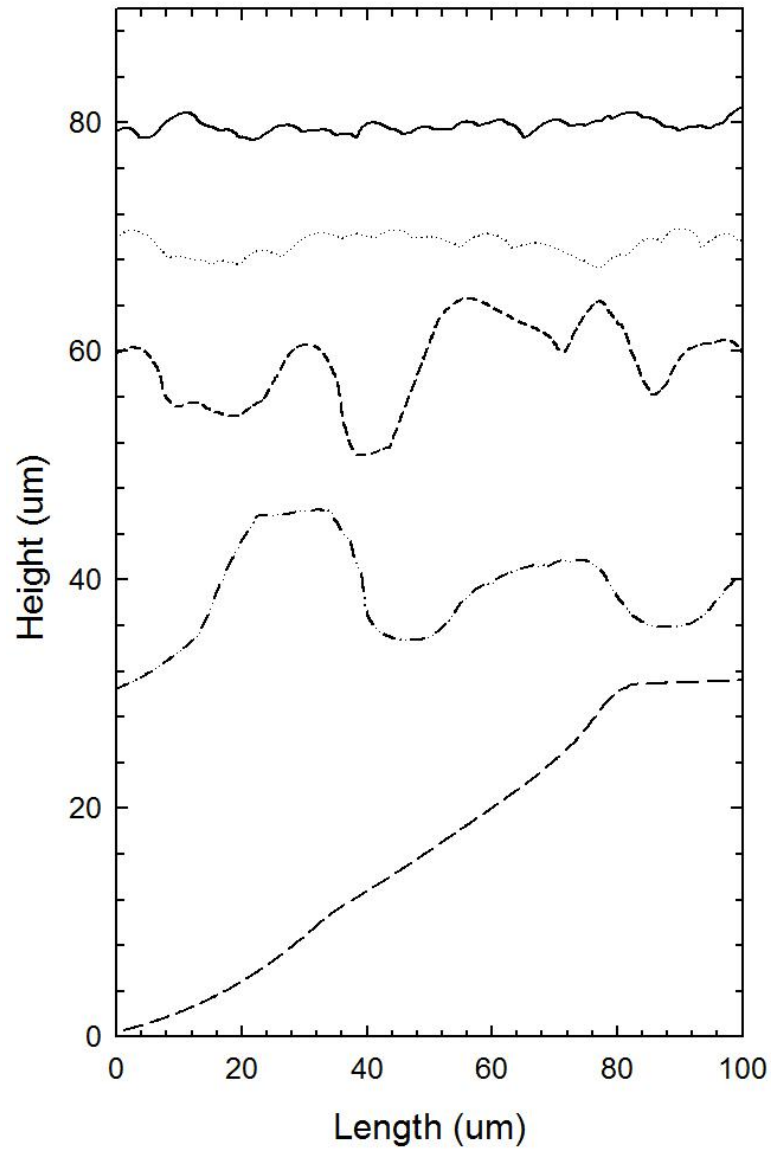


Figure 8.3 The surface profile of substrate a-e. The grit size is different, and confirmed with manufacture's data. The peak and valley distance is also various from substrate a-e.

8.3 Morphology Study of SiC Substrate

Figure 8.2 shows the SEM images of SiC substrates. Grits are uniformly distributed, as observed from SEM images. And the grit sizes showing in the SEM images confirm the grit sizes from manufacturer's data. Different size of grits forms distinct morphology of SiC substrate. As shown in Figure 8.3, the five profiler curves represent the topography of the five sandpapers. The mean peak and valley height (R_z) are measured from ten different points of the sandpaper, $R_z(a)=3.55 \mu\text{m} \pm 0.69 \mu\text{m}$, $R_z(b)=5.41 \mu\text{m} \pm 0.81 \mu\text{m}$, $R_z(c)=11.64 \mu\text{m} \pm 0.93 \mu\text{m}$, $R_z(d)=16.88 \mu\text{m} \pm 1.42 \mu\text{m}$, $R_z(e)=35.11 \mu\text{m} \pm 3.54 \mu\text{m}$. Figure 8.4 illustrates the relationship between grit size and R_z . The sandpapers with grit size of $5 \mu\text{m}$, $8.4 \mu\text{m}$, $15.3 \mu\text{m}$, $30.2 \mu\text{m}$ and $68 \mu\text{m}$ make a linear increase in R_z .

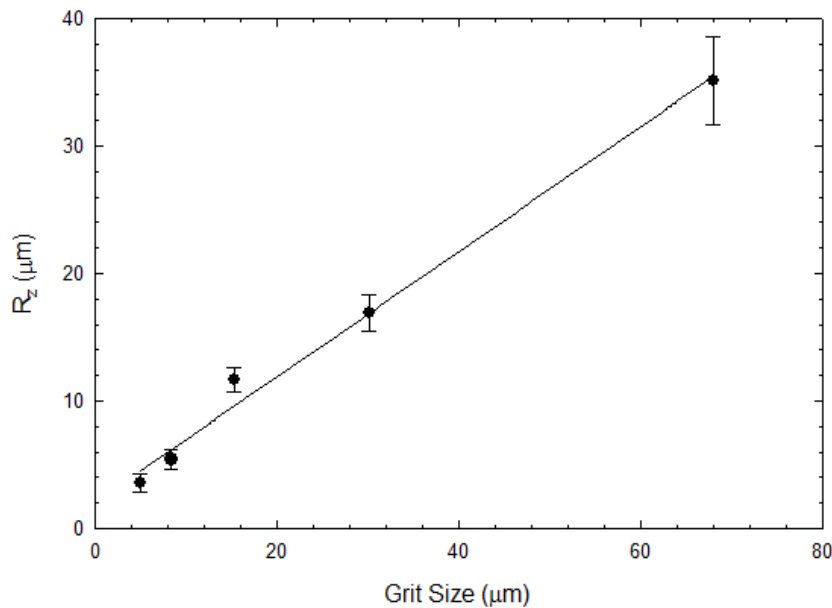


Figure 8.4 The relationship between grit size and the mean peak and valley roughness (R_z), the grit size information is supplied by manufacturer, and the R_z is obtained from the surface profile of each substrate.

8.4 Adhesion Test between electrospun PCL membrane and SiC substrate

SLBT adhesion test, as discussed in Chapter 4, is adopted to evaluate the adhesion energy. The sandpaper is fixed as the substrate, and PCL membrane is tested on the sandpapers. For each sandpaper substrate, five tests are performed to confirm the repeatability. Figure 8.5 shows five applied force vs. central deflection curves, and substrate effect is clearly observed. Every curve has a linear increasing region, and then drops at a turning point. The membrane afforded highest applied force at the turning point. The applied force drops significantly after the turning points, which illustrates materials failure. Different from test results from Chapter IV, there is no plastic deformation region in Figure 8.5. Membrane fails quickly after the turning point. The membrane is not re-usable, because the membrane damage during the test. Sample *a* exhibits lower applied force at the turning point, and the linear region is the shortest. With the roughness of the surface increase, the applied force at the turning point increases gradually from 0.0268 N (substrate a) to 0.0883 N (substrate e). Sample b, c and d have the turning points at 0.0321 N, 0.0368 N, 0.0742 N respectively. The turning points appear at a larger central deflection with rougher substrate. For substrate a, the turning points appear when central deflection reaches 2.23 mm. Sample b, c, d and e have the turning points at 2.409 mm, 3.077 mm, 4.408 mm and 3.375 mm. The phenomena illustrates rough surface can stretch the membrane more than smooth surface, reaches a higher applied force and larger deformation.

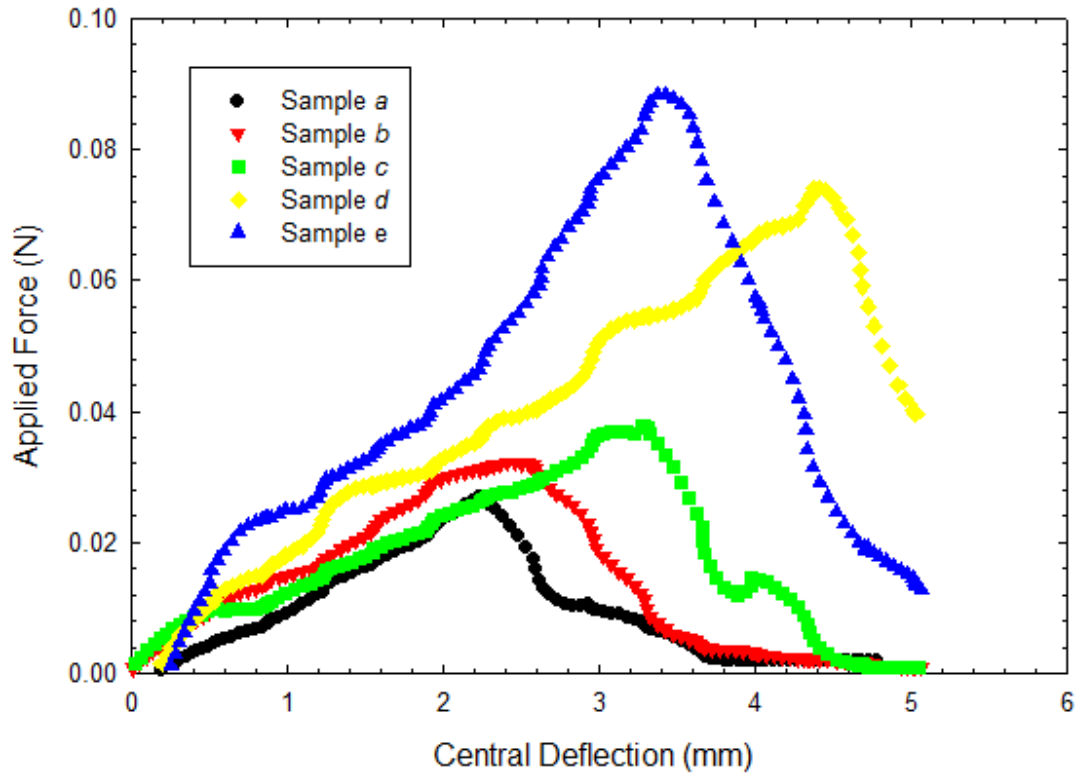


Figure 8.5 The relationship between central deflection and applied force for substrate a-e.

From Figure 8.5, the ratio of applied force and central deflection (P/w_0) can be obtained, 11.91 ± 0.84 N/mm, 13.64 ± 1.12 N/mm, 13.29 ± 1.47 N/mm, 15.2 ± 1.81 N/mm and 17.43 ± 1.17 N/mm from substrate a-e respectively. A linear relationship is established between P/w_0 and R_z , as shown in Figure 8.6. A linear relationship between w_0/a and R_z is also shown in Figure 8.6. The values of w_0/a for substrate a-e are 0.5277 ± 0.034 , 0.5179 ± 0.051 , 0.5403 ± 0.071 , 0.5507 ± 0.044 , 0.5893 ± 0.035 , respectively. From these two trend lines, a linear relationship between the work of adhesion (W) and R_z can be expected.

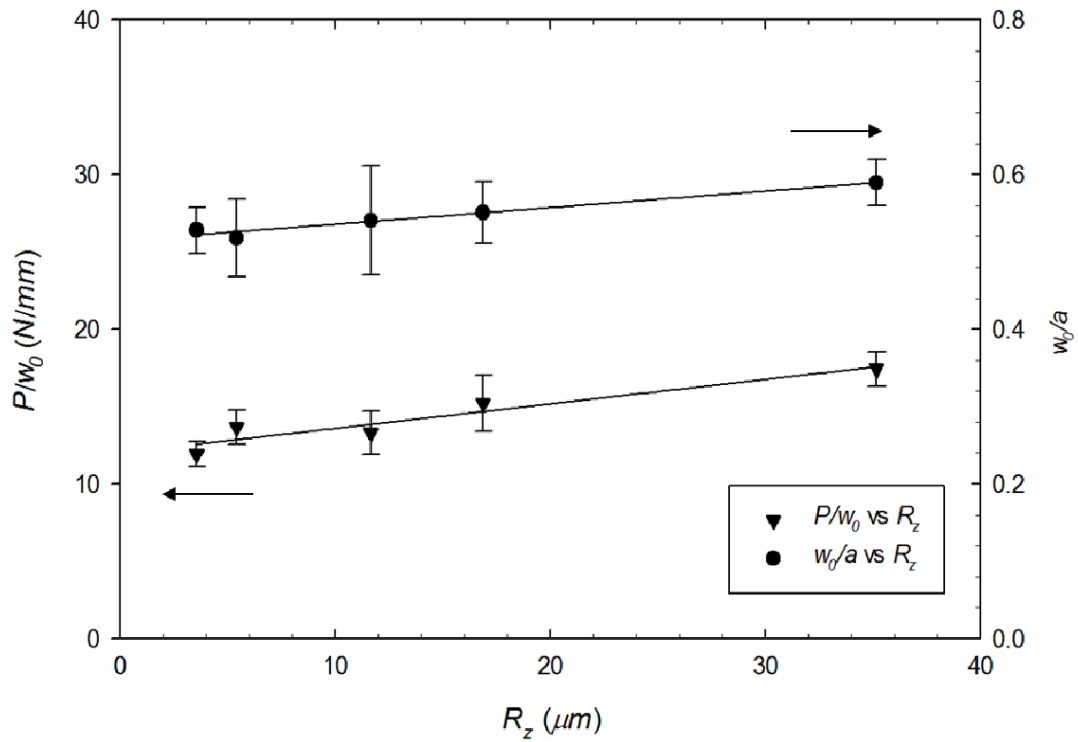


Figure 8.6 The relationship between P/w_0 (applied force/central deflection) and R_z (shown in triangle) and the relationship between w_0/a (central deflection/debonding radius) and R_z . Both show a linear increase trend with R_z increase.

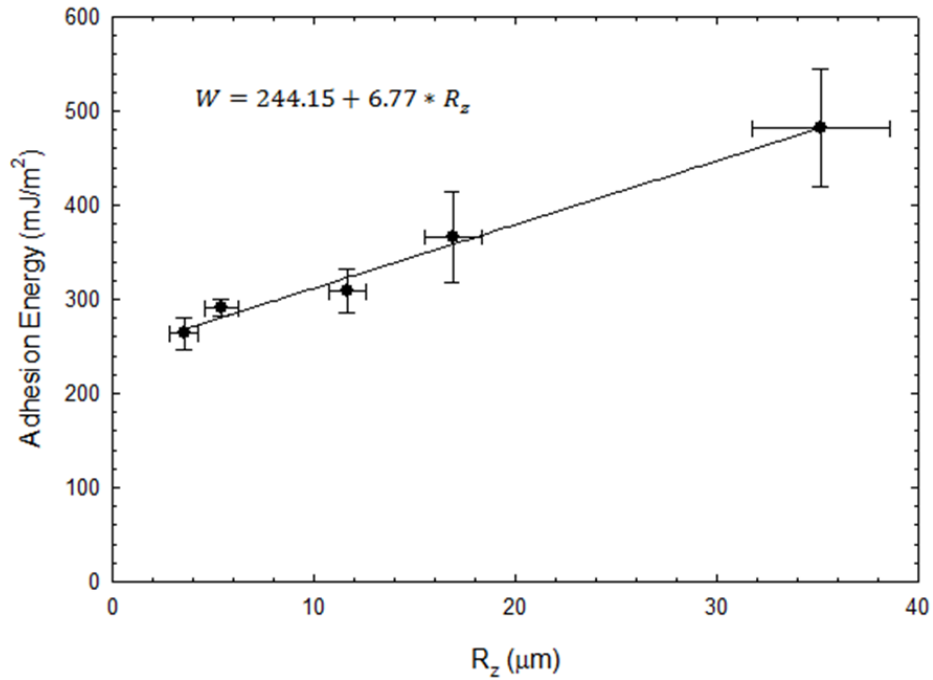


Figure 8.7 The relationship between adhesion energy and R_z . A linear regression is established.

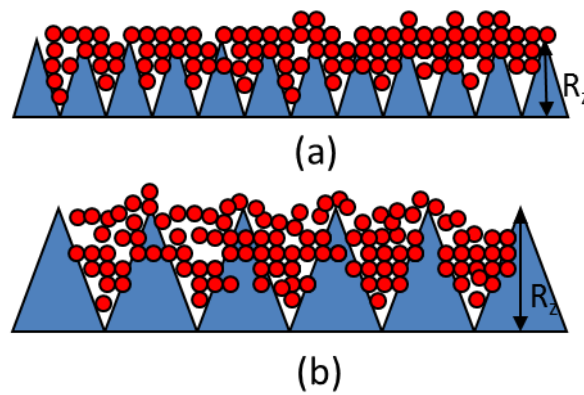


Figure 8.8 The schematic for substrate effect, (a) Substrate asperities represent in triangle shape, and electrospun fibers are represented in circle. R_z is the mean peak to valley value. (b) Substrate with rough surface. R_z increase causes an increase of the surface area of each grit, and thus the adhesion energy increases reasons from actual contact area increase. (c) The shape of deformed membrane

8.5 Effect of Substrate on the Work of Adhesion

Figure 8.7 illustrates the relationship between the work of adhesion (W) and R_z . With the increase of roughness R_z , the work of adhesion gradually increases, $264.12 \pm 16.97 \text{ mJ/m}^2$ for substrate a, $291.14 \pm 8.51 \text{ mJ/m}^2$ for substrate b, $308.73 \pm 23.34 \text{ mJ/m}^2$ for substrate c, $366.83 \pm 48.40 \text{ mJ/m}^2$ for substrate c and $481.68 \pm 62.55 \text{ mJ/m}^2$ for substrate e. Since the contact materials, PCL and SiC, are the same, even the PCL membranes are fabricated from the same electrospinning condition. The nominal work of adhesion should be the same if considered thermodynamically, because the surface energy keeps consistent. Surface roughness changes always can cause effective mechanical interlocking which can significantly improve the adhesion energy [184-185].

The mechanism of mechanical interlocking is illustrated in Figure 8.8, the red color represents PCL membranes, and the blue color represents the Sic substrate. Figure 8.8 (a) show the contact condition between electrospun membrane and substrate with different roughness. For a rough surface, as shown in Figure 8.8(a), the asperity of the substrate can penetrate the membrane, increase contact area, and partial of the fibrous is locked between the asperities. Mechanical interlocking effect is enhanced with the increase of asperity size, as shown in Figure 8.8(b). Without doubt, the penetration by substrate asperity is irreversible. The fibrous structure is damaged, because the original joints between fibers are deformed or broken. Some fibers are left in the substrate due to the high locking strength which is possible to overcome the cohesive rupture strength.

The most widely cited mechanical interlocking model is Gent's elastic contact model, as review in Chapter 2.2.2 [50].

$$W = W_0[1 + n\pi a^2 \left(\frac{4l}{a} - 1\right)] \quad \text{Equation 8.1}$$

where W_0 is the characteristic work of adhesion, n is the numbers of the holes, l is the depth of the hole or the length of the adhesive strands, and a is the radius of the hole. By studying the random distribution of equal size particle [186], the number of particles in a certain area decreases in proportion of particle size,

$$n \propto 1/a \quad \text{Equation 8.2}$$

If we assume the adhesion in these asperities is equivalent to adhesion at the surface, the model can be simplified to:

$$W/W_0 = 1 + 4n \pi a^2 (l/a) \quad \text{Equation 8.3}$$

Therefore, a linear relationship between the work of adhesion and depth of the asperity, which is the mean peak to valley value (R_z) here, can be derived

$$W/W_0 \propto 1 + 4\pi l \quad \text{Equation 8.4}$$

Therefore, with a linear regression, a linear relationship is established, with a coefficient of determination $R=0.9933$,

$$W = 244.15 + 6.77 * R_z \quad \text{Equation 8.5}$$

When $R_z=0$, W_0 can be obtained at 244.15 mJ/m^2 . In order to verify the results, van der Waals model and JKR theory are adopted to estimate the work of adhesion. Van der Waals contribution to adhesion can be estimated from

$$F_{vdw} = AR/6d_0^2, \quad \text{Equation 8.6}$$

where A is the Hamaker constant, when two different materials contact, $A = \sqrt{A_1 A_2}$, where A_1, A_2 are the Hamaker constants for the two materials. R is the contact radius, and d_0 is the cutoff distance. Then F_{vdw} can be estimated, which contribute to adhesion force. From JKR theory, the work of adhesion can be related with adhesion force by the following equations,

$$F = 3/2\pi RW_0 \quad \text{Equation 8.7}$$

Therefore, the work of adhesion contributed by van der Waals force (W_{vdw}) can be estimated by the following equation,

$$W_{vdw} = \frac{A}{9\pi d_0^2} \quad \text{Equation 8.8}$$

where $A_1 = 13.5 \times 10^{-20} J$ for PCL, and $A_2 = 24.8 \times 10^{-20} J$ for SiC. $d_0 \approx 0.3 \text{ nm}$. Therefore, $W_{vdw}=71.84 \text{ mJ/m}^2$ can be obtained. Compare W_{vdw} with W_0 , the orders of magnitude are consistent. The slight variation can be caused by the testing conditions and environment, the type of monomers and molecular weights supplied, and the assumption of d_0 , which can vary from one material to another. The results show the measure adhesion energy is consistent within the van der Waals range, and then support the existence of van der Waals force.

8.6 Effect of Loading Speed on Adhesion Energy

Substrate a is selected to perform SLBT adhesion tests under different loading speed. Loading speed of 0.10 mm/s, 0.33 mm/s, 0.66 mm/s and 1.0 mm/s are used.

Figure 8.9 shows the effect of loading speed on P/w_0 and w_0/a . Figure 8.9 illustrates the adhesion energy as a function of loading speed. No obvious trend can be observed in Figure 8.8 and Figure 8.9. The value of P/w_0 and w_0/a vary in a narrow range. The adhesion energy (W) is also independent to the loading speed.

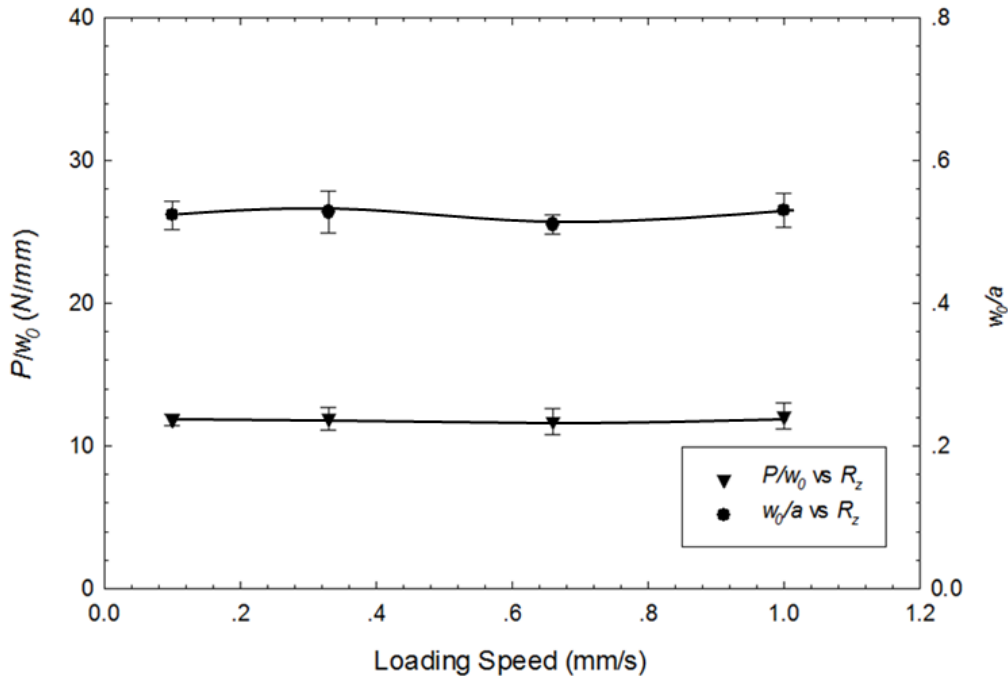


Figure 8.9 The relationship between P/w_0 (applied force/central deflection) and loading speed (shown in triangle) and the relationship between w_0/a (central deflection/debonding radius) and loading speed.

Some researchers observed speed effect during peel test. Shi and co-workers [145] observed speed effect during pull-off test of electrospun fibers. They explained the speed effect by the non-equilibrium state of electrospun fiber surface [187]. The viscoelastic behavior of polymer is also a possible explanation for the speed effect. The viscoelasticity of polymer can be indicated by Deborah number (D_e) [188], D_e is defined as,

$$D_e = \tau \frac{\dot{D}}{D} \quad \text{Equation 8.9}$$

where τ is the relaxation time of the polymer materials, \dot{D} is the loading speed and D is the separation distance. A smaller D_e indicated the material performs more like viscous liquid. In our case, PCL has the relaxation time of 0.05 s at room temperature [189], and D equals 2.5 mm, varies from 0.1mm/s to 1mm/s. Therefore, D_e varies from 0.002 to 0.2. PCL should perform more like a solid if the loading speed increase. However, no obvious effect of viscoelasticity is observed from the results of adhesion energy.

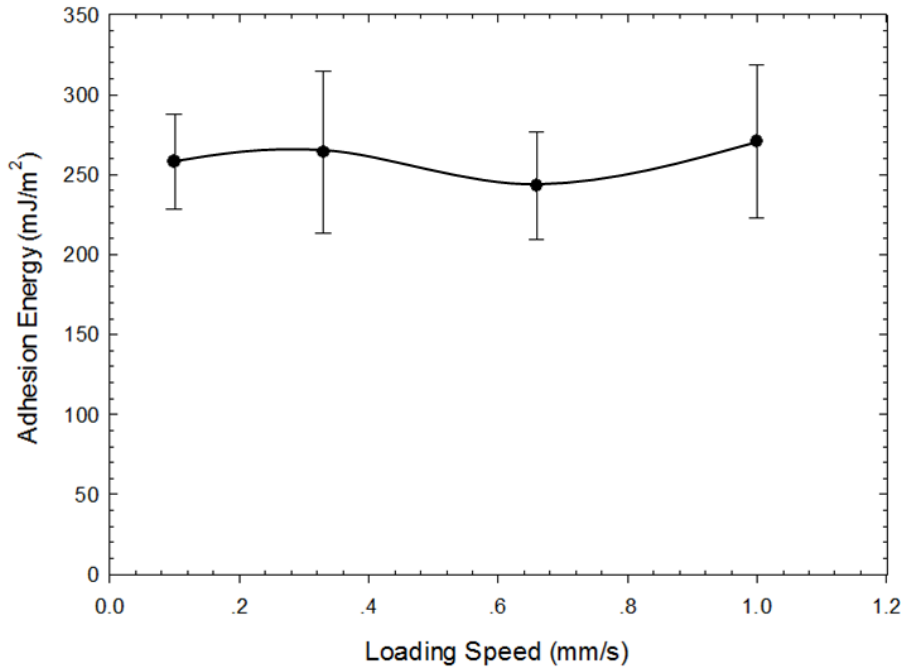


Figure 8.10 The relationship between adhesion energy and loading speed. No obvious effect of loading speed is observed.

8.7 Conclusions

Adhesion between electrospun membrane and rough SiC surface is evaluated by applying substrate with different roughness. The size of the surface girt varies from 5 μ m

to 68 μm , and causes the Rz ranges from $3.55 \mu\text{m} \pm 0.69 \mu\text{m}$ to $35.11 \mu\text{m} \pm 3.54 \mu\text{m}$. Mechanism of interlocking is the dominated mechanism for contact with rough surface. The effect of mechanical interlocking is explained by a simple triangular contact model. By using this model, the adhesion energy can be estimated for substrate with different roughness, and the contact between electrospun membrane and ideal smooth surface is also estimated by using the mechanical interlocking model, as 244.15 mJ/m^2 . The predicted result, 71.84 mJ/m^2 , is comparable with theoretical estimation from van der Waals force. This hypothetical consideration corroborates that the vdW is the primary force behind the adhesion between electrospun membrane and SiC sandpapers in this study. This study provided fruitful insight into adhesion applications of electrospun membrane on rough surface. Further study can be conducted on the improvement of interlocking effect to create a nano-scale connector to connect nano-size devices.

CHAPTER IX

ADHESION BETWEEN ELECTROSPUN PCL MEMBRANES: DUE TO VARIOUS SUBSTRATES

9.1 Introduction

In this chapter, the shaft-loaded blister test (SLBT) is adopted to evaluate the adhesion between electrospun nonwovens and rigid substrates. The classical blister test developed by Dannenberg [190] essentially uses hydrostatic pressure to drive delamination of the membrane-substrate interface, and the adhesion energy is thus derived from the applied pressure and blister dimension. The now celebrated technique is practically cumbersome since it is difficult to measure pressure to high accuracy, let alone the simultaneous measurement of blister growth. In a more convenient SLBT, mechanical load is applied to the center of an overhanging membrane to drive an axisymmetric conical delamination at the membrane-substrate interface. Simultaneous measurement of the small mechanical load, instead of hydrostatic pressure, and the blister radius, thus allows one to evaluate the strain energy release rate. The SLBT is aptly suitable for thin fibrous membrane, because both elastic modulus and adhesion energy can be measured in a single step and setup. The axisymmetric geometry also eliminates the possible edge effect in a conventional peel test.

To qualify the adhesion property, interfacial debonding by applying stress is the most direct way to evaluate. Conventional peel test [149] obtains adhesion property in the

same approach. However, plastic deformation is unavoidable in peel test, which will consume most of the energy dissipation, and a small work of adhesion is observed. In this chapter, we adopt a Shaft Loaded Blister Test (SLBT) [149,191] to avoid the drawback of peel test.

Van der Waals interactions between electrospun membrane and various substrates are discussed in Chapter VII and VIII. Adhesion energy can be improved by increasing the roughness of the substrate. Ko and co-workers [192-195] are proved nanowire forests are effective connect with the other nanowire forests, and has a strong adhesion strength. The nanowire forests only connect with the same nanowire forests, and have minimal adhesion strength with other surface [192]. The unusual property is utilized to produce nano-scale connector, which can be recognized as a nano size Velcro®. In this chapter, adhesion energy between two electrospun membranes will be examined. The nano Velcro® effect is expected for the contact between two fibrous structures.

9.2 Sample Preparation

PCL solution is prepared by dissolving the PCL powders in CHCl_3 and DMF (7:3 v/v) at 40-50 °C for 2 h. The concentration of PCL solution is 0.12 g/mL. The prepared solution is then electrospun to fibrous membrane for further adhesion test. The same solution is also used to cast PCL film for further adhesion evaluation. The cast film process is described in Chapter 4.2.

9.3 Surface morphology

Adhesion is a kind of surface property. Essentially, for membranes, adhesion is the general interaction between the membrane surfaces. So the principal issues of membrane adhesion are related to the membrane surface morphologies. In SLBT, electrospun PCL membrane is used as the test membrane. The fiber morphology and surface topography are shown in Figure 9.1. Figure 9.1(a) exhibits the membrane has a uniform fiber morphology. Fiber diameters are around 100-400 nm and majority of the fibers are concentrated at 200-300 nm, see Figure 9.1(b). Because of the tiny diameters, electrospun PCL fibers are very flexible. The flexible fibers are random-assembled in electrospun PCL membrane. They form a rough surface as detected by AFM, see Figure 9.1(c). Electrospun PCL membrane shows a 600-700 nm fluctuation at the surface profile as shown in Figure 9.1(d).

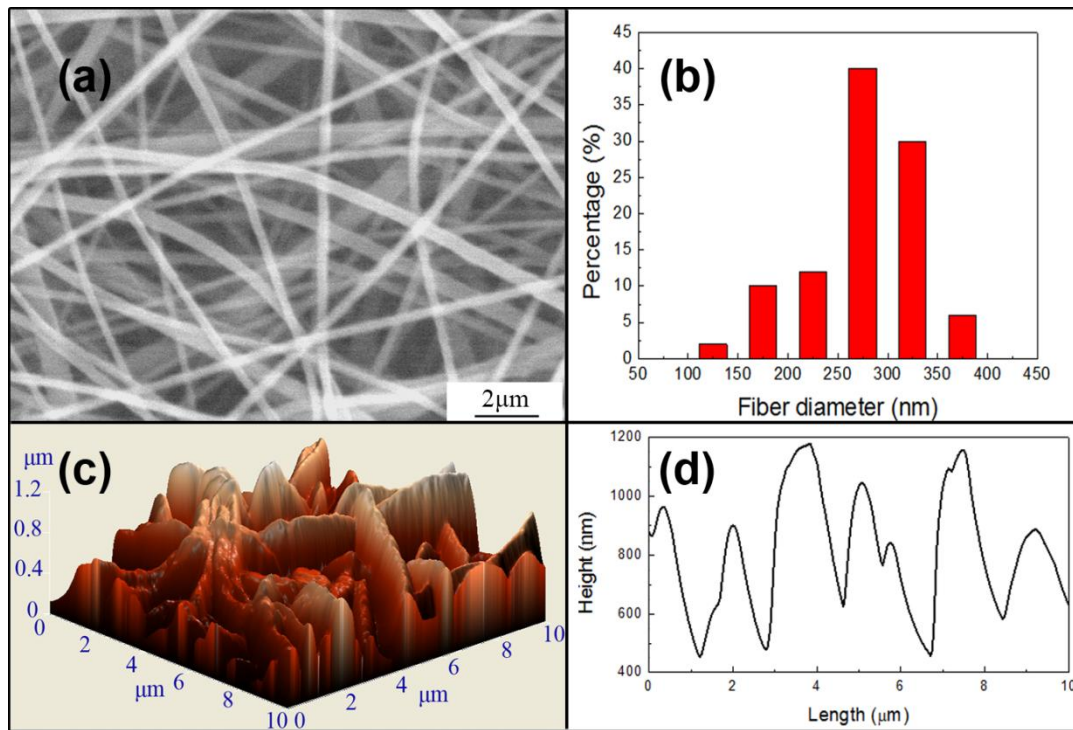


Figure 9.1 Fiber morphology and surface topography of test membrane. Test membrane is composed by electrospun PCL fibers. SEM image (a) shows the uniform fiber morphology at surface. Fiber diameters (b) are concentrated at 250-400 nm. Surface topography (c) is obtained by surface scanning with AFM. The scanning profile (d) fluctuates obviously. The height fluctuation of the membrane surface is ~800 nm. The test film shows fiber morphology and rough surface.

In SLBT, electrospun PCL membrane and cast PCL film covered rigid substrates are respectively used as test substrate. Because adhesion is the interaction between membrane surfaces, actually the adhesion obtained in experiment reflects the adhesion between test membrane and the membrane cover of test substrate. The surface morphologies of the membrane covers are shown in Figure 9.2. The electrospun PCL membrane exhibits a rough surface, see Figure 9.2(a). Its surface profile has a 600-700 nm fluctuation [Figure 9.2(b)] owing to the fiber morphology. When cast PCL film is used instead of electrospun PCL membrane, only relative smooth surface is exhibited

[see Figure 9.2(c)]. The surface fluctuation of the cast PCL film is around 200 nm, see Figure 9.2(d). Electrospun PCL membrane and cast PCL film provide two different models. They are respectively used in SLBT to discuss the change of adhesion impacted by fiber morphology at the surface.

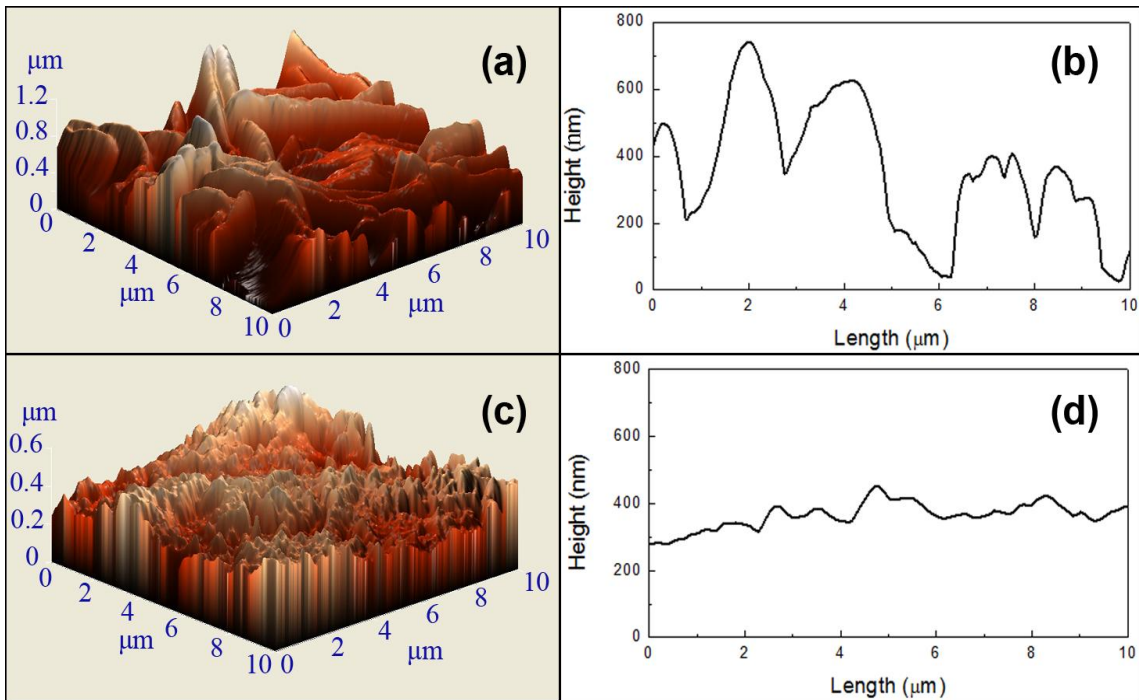


Figure 9.2 Surface topography and profile of membrane covers of the test substrates. Electrospun PCL membrane (a, b) and cast PCL film (c, d) are respectively used as membrane cover for the test membrane. Electrospun membrane cover shows a rough surface (a) with the height fluctuation ~ 800 nm (b). In comparison, a relative smooth surface (c) is exhibited in cast film cover. The height fluctuation of cast film is ~ 150 nm.

9.4 Adhesion Characterization

The exterior force (P) vs. central deflection (w_0) curves obtained from SLBT by use of two different membrane covers are respectively shown in Figure 9.3(a) and (b).

When SLBT is operated between electrospun membranes, P/w_0 curves show a linear

increase at the beginning [see Figure 9.3(a)]. With the increase of central deflection (w_0), the P/w_0 curves wiggled grow. Fluctuation is observed on P/w_0 curves. This phenomenon is attributed to the amorphous fibrous morphology of electrospun PCL membrane. In SLBT, delamination occurred between electrospun PCL membranes is actually concerned with the debonding of electrospun PCL fibers. Due to the amorphous fiber morphology, electrospun membrane could not initiate a complete stable delamination with a membrane cover. When the unstable delamination reflects on P/w_0 curves, a slight fluctuation is appeared. Except the unstable fluctuation, the P/w_0 curves almost increase monotonically. The linear increase of the exterior force (P) with central deflection (w_0) reflects the linear elastic response of the electrospun PCL membrane. As to the electrospun membrane, elastic response refers to the general effect of mechanical responses such as fibers strain, the fiber elastic deformation under stretching and the fiber orientation. After the central deflection grows over a critical point, in experiment ~ 4 mm [see, Figure 9.3(a)], yielding is taken place. In the SLBT of electrospun membrane, yielding is not only related to the plastic yielding of PCL material. It is also produced by slight relative movement between PCL fibers and lateral slip of electrospun fiber on membrane cover.

Similar process can be also found in the SLBT of electrospun PCL membrane with cast PCL film, see Figure 9.3(b). On the P/w_0 curves in Figure 9.3(b), linear increase, fluctuate growth and yielding transition are all existed. Between the P/w_0 curves in Figure 9.3(a) and (b), the main difference is the maximum exterior force. The exterior (P) force of the delamination between electrospun PCL membranes reaches 0.08-0.10 N, see Figure 9.3(a). But the exterior force of electrospun PCL membrane with cast PCL film is 40-50 % lower. Only 0.4-0.6 N is detected from the delamination [see Figure 9.3(b)].

Owing to the flexible fiber morphology and surface topography [see Figure 9.1 and Figure 9.2(a)], ultrafine fibers in one of the electrospun membranes can be crushed into the space between the fibers of the other electrospun membrane under pressure. As a result, fiber-fiber interpenetration is formed. The fiber-fiber interpenetration can provide larger surface contact and interlocking effect. A strong surface interaction is produced. High exterior force is needed to peel away the electrospun PCL membrane from the electrospun PCL membrane cover. In comparison with electrospun PCL membrane cover, cast PCL film is rather stiff and short of deep fluctuated region for fiber penetration at the surface. Only small contact and weak interlocking can be produced between electrospun PCL membrane and cast PCL film. So, small exterior force is found in their delamination, see Figure 9.3(b). Maximum exterior force for delamination in SLBT is actually the adhesion force between the electrospun PCL membrane and the membrane cover. The results in Figure 9.3 show stronger adhesion force is produced between electrospun membranes.

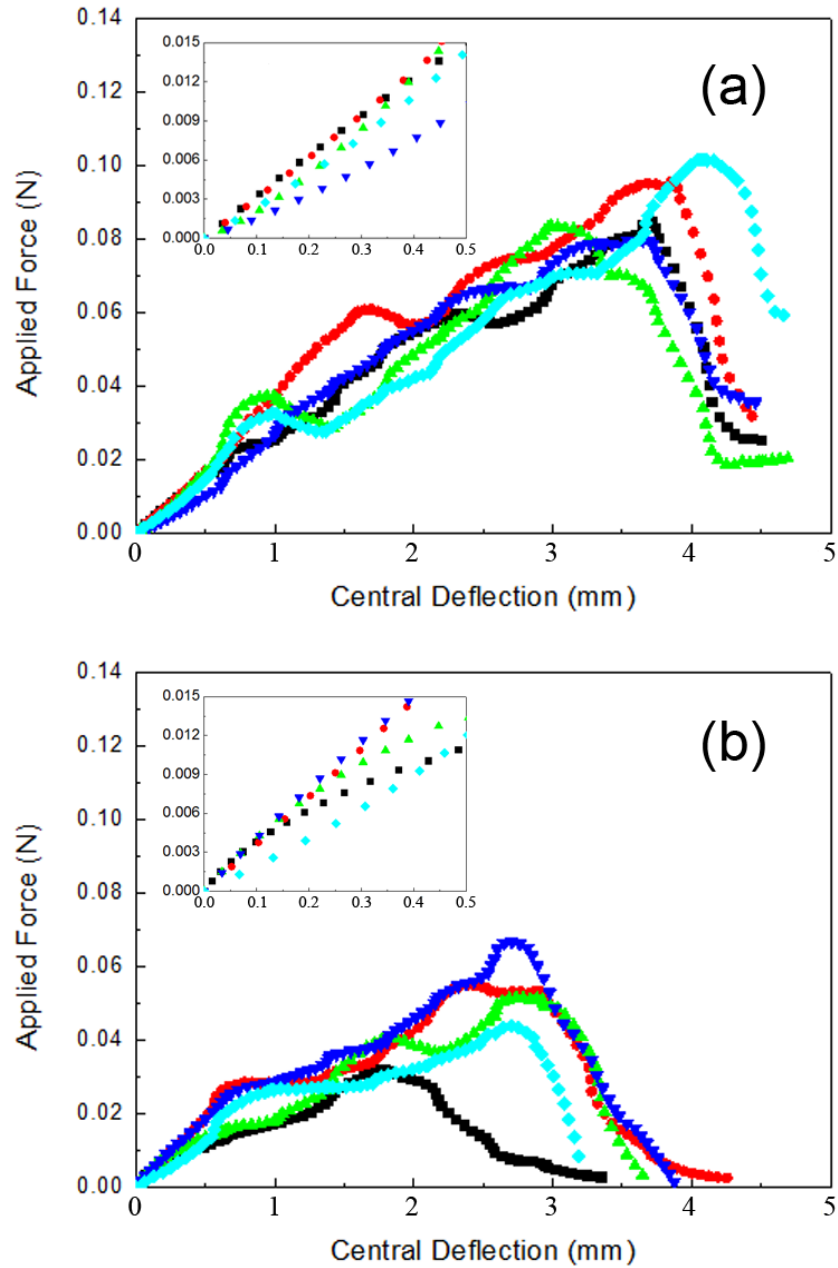


Figure 9.3 Exterior force (P) vs. central deflection (w_0) curves of SLBT by use of test substrates covered with (a) electrospun PCL membrane and (b) cast PCL film respectively. 5 measurements are taken to show the relations between exterior force and central deflection. The initial parts of P - w_0 curves exhibit linear trend concerned with the stable debonding between test membrane and membrane cover.

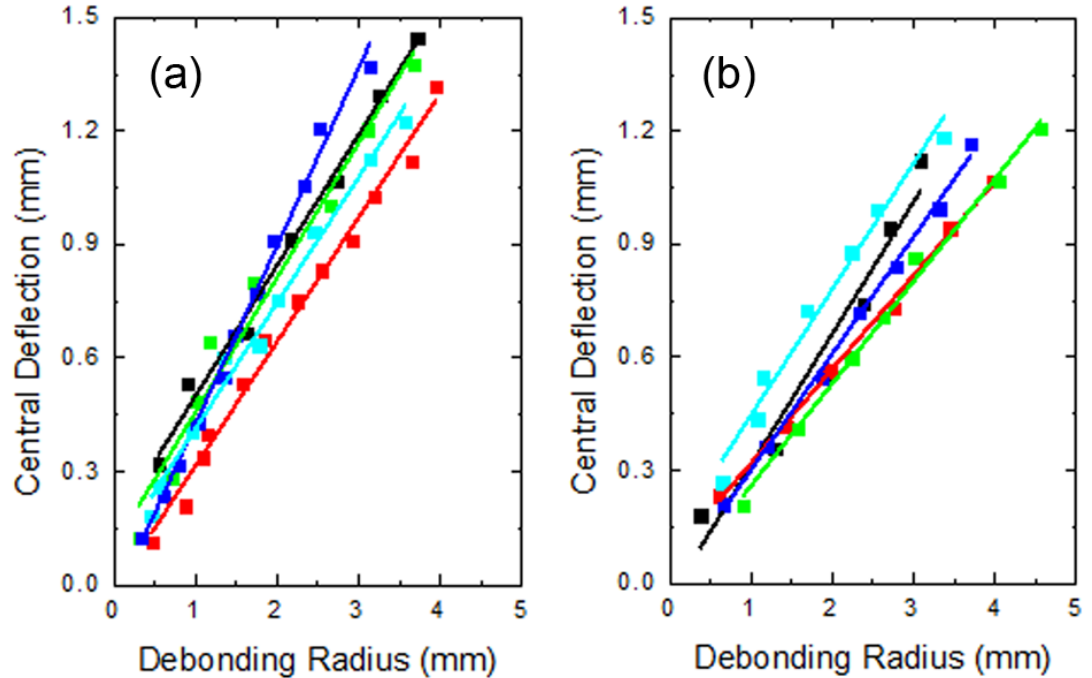


Figure 9.4 The central deflection (w_0) plotted as a function of debonding radius (a) for the test membrane blister. w_0 and a of test membrane blister are measured from video record by use of (a) electrospun PCL membrane and (b) and cast PCL film covered substrates in SLBT. When w_0 is 0-2 mm, w_0 - a curves show a linear trend.

P/w_0 curves are also used to calculate the adhesion energy. As shown in Equation 5.26, the slopes of the linear elastic parts of P/w_0 curves are taken into account for the adhesion energy calculation. In order to assure the accuracy of calculation, only the initial parts of P/w_0 curves are used to measure the slopes, see Figure 9.4 (a) and (b). Majority of initial parts of P/w_0 curves in Figure 9.4 (a) and (b) show very clear linear increase. It reflects the pure elastic response of electrospun PCL membrane in SLBT. The slopes measured from initial parts of P/w_0 curves are summarized in Table 9.1.

During the calculation of adhesion energy, the slopes of central deflection (w_0)/debonding radius (a) are also needed. The w_0/a curves are obtained in experiment

and shown in Figure 9.4. When central deflection is below 1.5 mm, almost all the w_0/a curves in Figure 9.5 (a) and (b) show linear increase. No matter electrospun PCL membrane or cast PCL film is used as the membrane cover in SLBT, w_0/a curves grows monotonically. It reflects the linear elastic response of test electrospun PCL membrane in SLBT. The values of w_0/a are measured from the trend lines of w_0/a curves and summarized in Table 9.1

Table 9.1 The slopes of w_0/a and P/w_0 curves.

ESM vs. ESM*	P/w_0 (N/m)	w_0/a (m/m)	ESM vs. CF**	P/w_0 (N/m)	w_0/a (m/m)
1	31.9	0.345	1	22.0	0.350
2	33.0	0.328	2	36.9	0.249
3	33.3	0.356	3	26.6	0.271
4	20.2	0.470	4	36.4	0.309
5	28.5	0.332	5	23.1	0.334

* ESM is the abbreviation of electrospun PCL membrane. ESM vs. ESM refers to the SLBT is operating by use of electrospun PCL membrane with electrospun membrane covered substrate.

** CF is represented the cast PCL film. The term of ESM vs. CF means SLBT is operating between electrospun PCL membrane and cast PCL film covered substrate.

9.5 Calculation of Adhesion Energy

By understanding the thermodynamic energy balance of the SLBT in our previous work [196], the strain energy release G equals the linear elastic energy of the test membrane. G is calculated only by considering the elastic response of the test electrospun PCL membrane. As shown in section 9.3, the adhesion-delamination analysis is under purely elastic response without any plastic yielding. The obtained G is the total energy including the work of fibers strain, the elastic energy associated with stretching and the energy of fiber orientation. Under the pure elastic deformation analysis, adhesion energy W equals to strain energy release G due to the mechanical equilibrium in SLBT, see our earlier work ref. [196]. The obtained W reflects the true adhesion at the electrospun membrane and membrane cover interfaces.

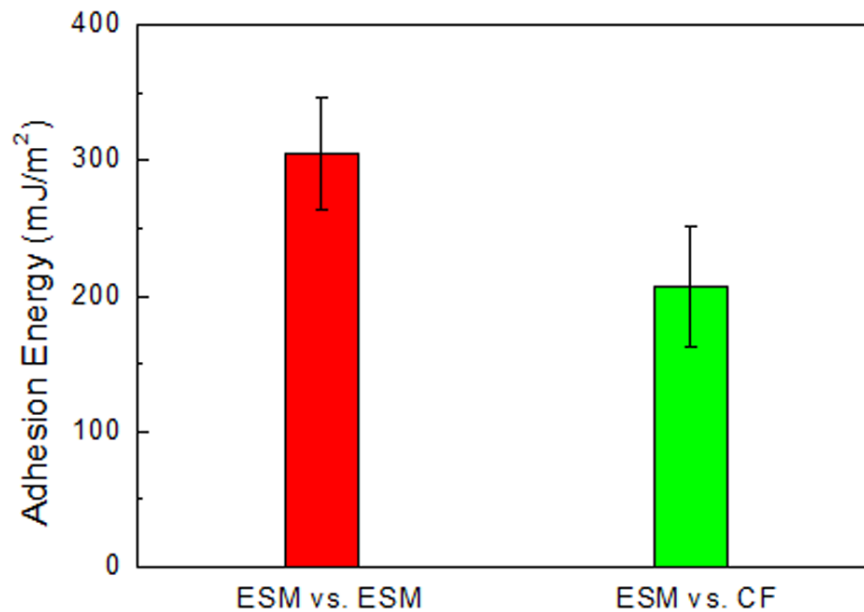


Figure 9.5 Adhesion energy of test membrane against membrane covers. Adhesion energy is calculated from Equation (2) by use of the data from Table 9.1. The average adhesion energy between electrospun PCL membranes (ESM vs. ESM) is 305.0 ± 41.9

mJ/m². This value is considered 1.32 times larger than the adhesion energy between electrospun PCL membrane and cast PCL film (ESM vs. CF).

By use of Equation 5.24 with the data in Table 9.1, adhesion energy is calculated. As shown in Figure 9.5, the adhesion energy between electrospun PCL membranes is 305.0 ± 41.9 mJ/m². Nearly 30% larger than the adhesion energy of electrospun PCL membrane with cast PCL film. The discrepancy in adhesion energy is attributed to the surface topography between contact membranes. The electrospun PCL membrane cover is composed by ultrafine electrospun fibers. It forms a fluctuated surface. When the test electrospun PCL membrane is fixed on the surface of electrospun PCL membrane cover, the fibers from the test membrane is penetrated into the vacant space. The two electrospun PCL membrane surfaces forms a compact contact named fiber interpenetration. It results in a large actual contact between electrospun fibers and the interlocking effect. High actual contact area increases the interaction between fibers. The strong interaction between one pair of fibers does not only confine the debonding between them but also the debonding of the other fibers thus produces the interlocking effect. The strong interaction between electrospun fibers particularly produced by the interlocking tremendously increases the general interaction between electrospun PCL membranes. High adhesion energy is observed. On the contrary, the cast PCL film has a relative smooth surface. When electrospun membrane is fixed onto cast film surface, electrospun fibers can only touch its smooth surface. Electrospun PCL fibers have no change to deeply penetrate into the surface of cast PCL film. It only forms small actual contact area hereby a weak interaction. Almost no interlocking structure can be formed

with electrospun fiber owing to the short of the fiber morphology of the cast PCL film. As a result, low adhesion energy is finally obtained in SLBT.

Interlocking fiber structure hinders relative sliding thus reduces the propagation of delamination, as discussed in Chapter VIII. It leads to large adhesion stress and high adhesion energy. Interlocking for adhesion increase is also researched by Stein and co-workers [170]. The core of the methodology refers to the preparation of rough contact interfaces between polymer plates. In Stein and co-workers' work [170], artificial rough interfaces were used to increase the actual contact of polymer plate and lessen the interfacial crack propagation from perpendicular direction. Then the interfacial toughness extremely increases from 8 J/m^2 to $145\text{-}170 \text{ J/m}^2$. Because of the fiber morphology, electrospun PCL membrane has a natural rough surface. It could easily fit for the requirement of interlocking formation with the other piece of electrospun membrane, as shown in Figure 9.6. The results obtained in SLBT clearly exhibit the high adhesion force and adhesion energy is produced between electrospun membranes.

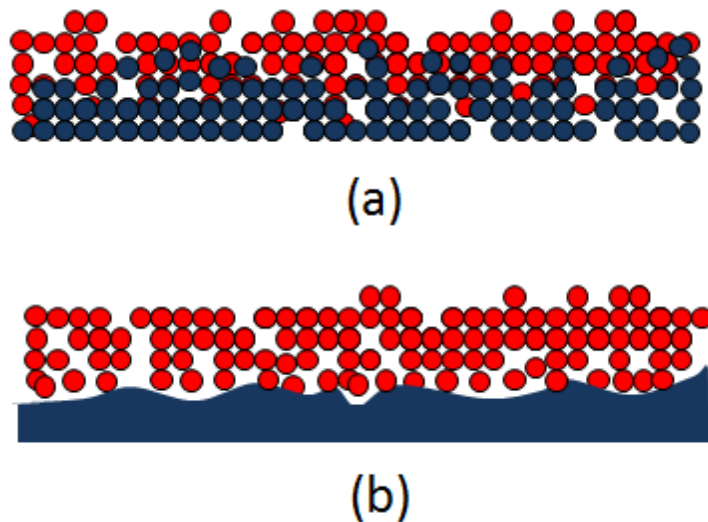


Figure 9.6 A schematic to represent the interpenetration and mechanical interlocking of electrospun membrane. (a) Contact between two electrospun membranes, both of the red and blue circles are PCL membranes, red color represents the upper tested membranes, and the blue color represents the substrate membranes. The fibers entangled with each other and interlocked with each other. (b) Contact between electrospun membranes and cast film substrate. The fibers (in red) could not penetrate into the cast film, and therefore less contact area is observed, and no fiber interlocking could happen either.

9.6 Conclusions

The morphologies of electrospun PCL membrane and cast PCL film are characterized by AFM, and significant difference in size of surface asperities is observed. The surface fluctuation of electrospun membrane is ~600-700 nm, compared to smooth cast film surface of ~200 nm. In SLBT, the adhesion force and adhesion energy of electrospun PCL membranes are evaluated. Ultrafine fiber morphology provides the electrospun membrane rough surface hereby the potential ability to produce high adhesion property. The curve of applied force vs central deflection for ESM vs ESM test is not as stable ESM vs CF, the variation of the curve illustrates the membranes entangle with each other, and reasons from broken of a local entanglement. The adhesion energy between electrospun PCL membranes is ~30 % higher than the adhesion energy of electrospun PCL membrane with cast PCL film. Fibrous structure can interpenetrate each other, and Electrospun membrane together with its fiber morphology provides an ideal model to increase adhesion property of thin membranes. The experimental results give researcher an inspiration to conduct application development of nano-connectors by use of the electrospun membranes.

CHAPTER X

FABRICATION OF ADHESION ENERGY BETWEEN HOLLOW FIBERS AND RIGID SUBSTRATE

10.1 Introduction

Flexible, microtubular structures present excellent potential for applications in microfluidics [197-199], water filtration and purification [200], drug release [201], electro- mechanical coupling [202], protective clothing [203] and energy conversion [204]. In many investigations, hollow fibers and hollow fibers are fabricated by core/shell electrospinning methodology. First, core/shell fiber is prepared in coaxial electrospinning. Then, the core is removed by post treatments to produce tubular structures. Core/shell fibers refer to liquid- core [205-208] and solid-core fibers [209-210]. Liquid core could be removed by vacuum drying [205] and [207] and solvent extraction [208]. Solid core is usually removed by solvent [209-210] or calcination [211].

A novel coaxial electrospinning methodology is presented to directly fabricate hollow fibers without any additional treatment. In this methodology, two incompatible polymer solutions are required as core and shell solutions, respectively. When the two solutions contact each other in electrospinning, the incompatibility between the two solutions will induce a gelled interface. As the electrospinning progresses, both the core and shell polymers coagulate at the gelled interface and thus hollow fibers are formed. In

this paper, incompatible poly(vinylidene fluoride) (PVDF) and poly(vinyl alcohol) (PVA) solutions are prepared by the novel coaxial electrospinning for hollow fiber formation.

The other issue is the secondary erosion caused by solvents trapped inside the hollow fibers. Because PVDF solution is dissolved in high boiling point solvents, the solvents cannot evaporate completely during the short time frame of electrospinning but partly left inside PVDF/PVA hollow fibers. The residual solvents could erode the microtubular wall. In order to mitigate secondary erosion, the residual solvents need to be removed in a timely fashion. In this study, a water (H₂O) assisted methodology is utilized to remove residual solvents and prevent secondary erosion. By means of a combination of the coaxial electrospinning and the H₂O-assisted methodology, PVDF/PVA hollow fibers are fabricated. The merits of this approach are that microtubular formation and mitigation of secondary erosion are accomplished simultaneously in one, single process without additional treatments. Our method is effective to eliminating solvent erosion and easier to handle. The physical properties and crystallization of the hollow fibers so produced are reported.

This chapter presents a unique approach to fabricating poly(vinylidene fluoride) (PVDF)/poly(vinyl alcohol) (PVA) hollow fibers in coaxial electrospinning. This methodology includes two objectives, namely, microtubular formation and mitigation of secondary erosion. In the first step, PVDF solution and ethanol mixed PVA solution are directly electrospun to PVDF/PVA hollow fibers. Then, the obtained PVDF/PVA hollow fibers are treated by a water assisted route to remove the residual solvents and mitigate the secondary erosion. Without solvent erosion, PVDF/PVA hollow fibers exhibit smooth inner and outer surfaces and hollow structure. Furthermore, in this technique, the hollow

fiber diameter and wall thickness are controllable by the feed rate of PVA solution in electrospinning. Thinner-walled hollow fibers are prepared under a high feed rate. Differential scanning calorimetry, X-ray Diffraction and Fourier Transformed Infrared Spectroscopy are respectively used to characterize the crystallization of PVDF. High degree of PVDF crystallinity is shown in thin PVDF/PVA hollow fibers. β -phase crystallite is dominant. For future applications, the motion of piezoelectric hollow structure can be controlled electrically, and gecko's locomotion could be mimicked by hollow structures. Therefore, a study of adhesion property of hollow PVDF/PVA fibers is necessary. Hollow structure has less material inside compared with solid fibers, hence the flexibility can be improved, which gives a potential to initiate a good contact with rigid substrate. In this chapter, the adhesion property of PVDF/PVA hollow fibers will be investigated by use of SLBT adhesion test.

10.2 Co-Axial Electrospinning of PVDF/PVA Hollow Fibers

A novel coaxial electrospinning methodology is presented to directly fabricate hollow fibers without any additional treatment. In this methodology, two incompatible polymer solutions are required as core and shell solutions, respectively. PVDF and PVA solutions are used as the shell and core liquids in coaxial electrospinning. PVDF solution is prepared at the concentration of 0.17 g/mL by dissolving PVDF powder in a mixture of DMSO and acetone (4:6, v/v) at 40 – 50 °C for 2 h. PVA is dissolved at 0.19 g/mL in a mixture of DMSO and ethanol (9:1, v/v) at 70 – 80 °C until a clear solution is obtained.

The coaxial electrospinning setup includes two syringes to independently feed PVDF and PVA solutions to electrospin hollow fibers, see Figure 10.1. The coaxial tip consists of two concentric needles. The exterior needle has an inner diameter of 1.3 mm. The interior needle has an inner diameter of 0.55 mm, and is set 0.5 mm longer than the exterior one at the end of a tip. Coaxial electrospinning is performed with varied core and shell feeding rates. The feed rate of core solution varies from 0.1 mL/h to 1.5 mL/h and shell feed rate is kept at 1.7 mL/h. A custom-made rotatable collector prepared by two parallel metal sticks is used to collect electrospun hollow fibers. The distance between the two metal sticks is 9 cm. During electrospinning, the rotating speed is controlled at 60 rpm. Applied voltage is kept at a constant of 10 kV. Distance between spinneret and collector is 6 - 7 cm. H₂O bath is utilized to assist coagulating PVDF/PVA hollow fibers, as shown in Figure 10.1. The collected fiber bundles are soaked into H₂O for more than 24 h to wash away the residual solvents. All the experiments operate at room temperature.

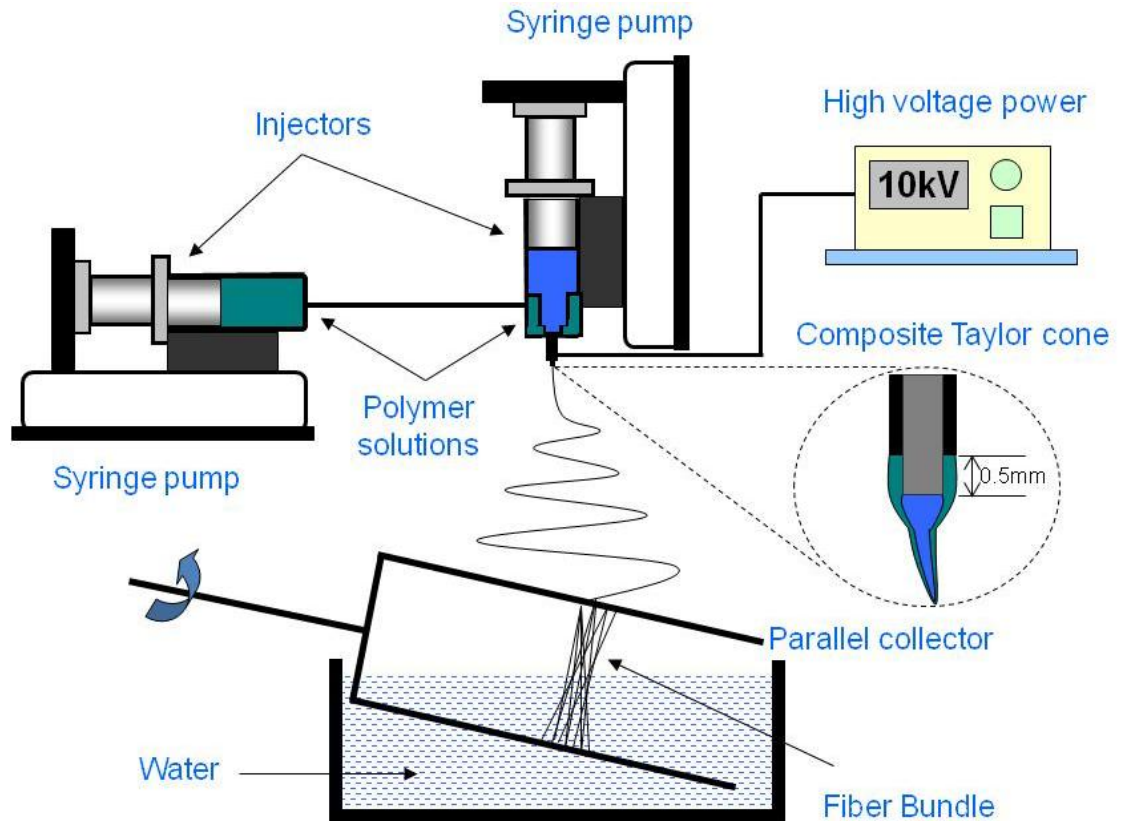


Figure10.1 Schematic that illustrates the set-up for co-axial electrospinning. Two different measuring pumps are used to independently control the feed rates of core and shell solutions. The inner solution is indicated by blue color. The shell solution is indicated by green. Two needles are packed in a co-axial setup. The internal needle is 0.5 mm longer than external needle. Applied voltage is kept constant at 10 kV to electrospun fibers. A rotating collector is prepared by two parallel metal wires. The distance between the two metal wires is about 9 cm, and the rotational speed is 60 rpm. H₂O bath underneath is utilized to assist coagulating PVDF/PVA hollow fibers simultaneously during electrospinning.

10.3 Formation of PVDF/PVA Hollow Fibers

In coaxial electrospinning, polymer solution is held at the end of the tip by surface tension. As the voltage increases, the electric field strength overcomes the surface tension. A cone begins to form with convex sides and a round tip. This is known in literature as the Taylor cone. Coaxial electrospinning consists of core and shell

solutions. Core and shell solutions are delivered independently through coaxial capillaries [212] and are only in contact transiently in the Taylor cone. In this study, the core solution is ethanol mixed PVA solution, and PVDF solution uses as the shell solution. Because ethanol is non-solvent of PVDF [213-214], the ethanol mixed PVA solution becomes moderately incompatible with PVDF solution. When PVDF solution contacts ethanol mixed PVA solution at Taylor cone, PVDF solution gels and forms an interface between core and shell solutions. Under a high potential difference, core and shell solutions along with the gelled interface form an electrospun jet and continuously eject from the Taylor cone's tip. As the solvent evaporates, PVDF solution precipitates at the outside of the gelled interface. PVA deposits at the inside of the gelled interface. Hollow structure is directly produced in coaxial electrospinning. Given equivalent wettability between PVDF and PVA, Zussman and coworkers [215] also demonstrated this technique to produce hollow polycaprolactone (PCL)/PVA fibers directly in coaxial electrospinning.

One issue is the secondary erosion caused by solvents trapped inside the hollow fibers. Because PVDF solution is dissolved in high boiling point solvents, the solvents cannot evaporate completely during the short time frame of electrospinning but partly left inside PVDF/PVA hollow fibers. The residual solvents could erode the microtubular wall. In order to mitigate secondary erosion, the residual solvents need to be removed in a timely fashion. In this study, a water (H₂O) assisted methodology is utilized to remove residual solvents and prevent secondary erosion. By means of a combination of the co-axial electrospinning and the H₂O assisted methodology, PVDF/PVA hollow fibers are fabricated.

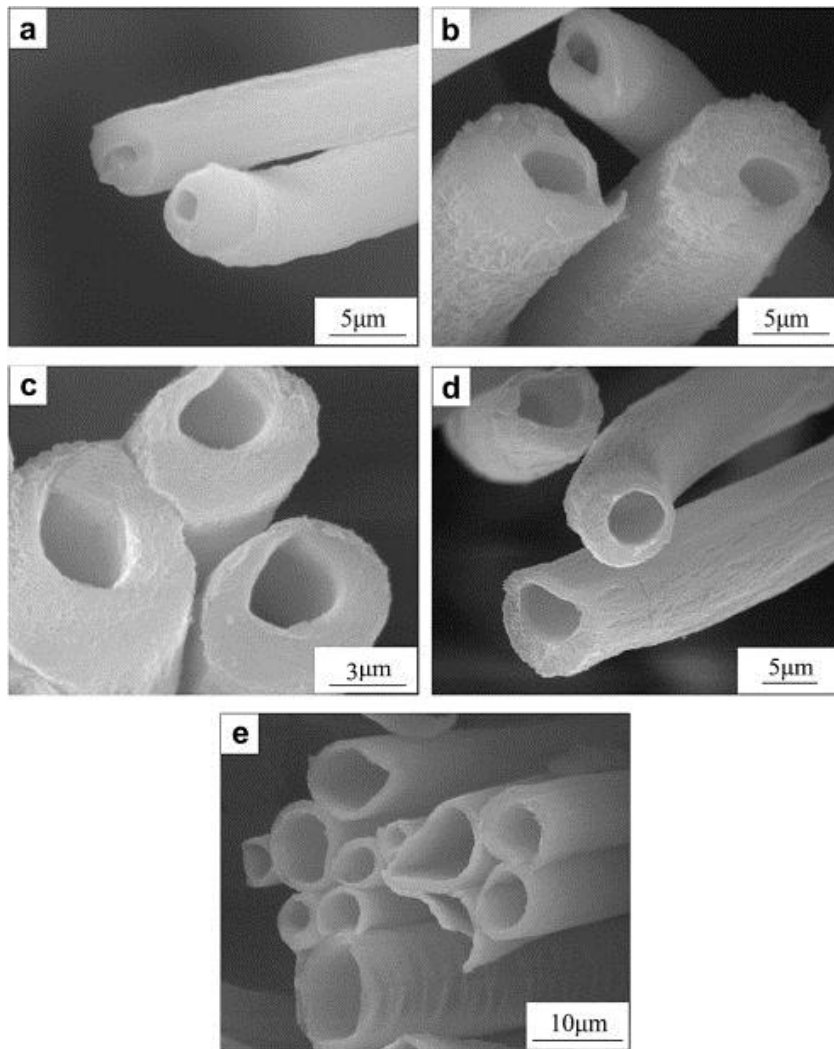


Figure 10.2 SEM micrographs of the PVDF/PVA hollow fibers prepared at different core/shell feed rates (mL/h) at (a) 0.1/1.7. PVDF/PVA hollow fibers exhibit the smallest diameter; (b) 0.3/1.7, the inner diameter in the PVDF/PVA hollow fibers increases; (c) 0.5/1.7, the thickness of the wall decreases, and approximately equals the inner diameter; (d) 0.8/1.7, the hollow fibers can be considered as thin-walled cylindrical shell, since the inner diameter is larger than the wall thickness; (e) 1.5/1.7, hollow fibers with ultra-thin wall is formed.

10.4 Diameters of the Hollow Fibers

One of the main purposes of this work is achieving the size control of the hollow fibers. One main issue studied was the effect of core/shell flow rates on the wall thickness of electrospun hollow fibers [212, 216-219]. However, in recent studies [212, 216-219], hollow fibers and hollow fibers are all prepared by core/shell electrospinning and a core removal process. Until now few discussed the control of wall thickness of the hollow fibers fabricated directly in coaxial electrospinning as in this study. When the feed rate of PVA solution is 0.1 mL/h (5.9% of the shell feed rate), PVDF/PVA hollow fibers demonstrate the smallest inner diameter, see Figure 10.2 (a). With the increase of the feed rate from 0.1 to 1.5 mL/h, the inner diameter of the tubular structure becomes increasingly large, see Figure 10.2 (b-e), whereas the wall thickness gently decreases. Regardless of feed rates, all electrospun PVDF/PVA hollow fibers in Figure 10.2 exhibit clear hollow structures, intact solid wall, and smooth inner and outer surfaces. The average inner and outer diameters of the hollow fibers are measured and shown in Figure 10.3. When the feed rate of PVA solution is increased from 0.1 mL/h to 1.5 mL/h, the inner diameter of the PVDF/PVA hollow fibers increases from $1.16 \pm 0.15 \mu\text{m}$ to $6.61 \pm 1.80 \mu\text{m}$ and the outer diameters of electrospun hollow fibers also increase from $5.70 \pm 0.59 \mu\text{m}$ to $9.79 \pm 2.25 \mu\text{m}$. The wall thicknesses of the PVDF/PVA hollow fibers are calculated with average outer diameters subtracting the average inner diameters. The results show the thicknesses of the PVDF/PVA wall gradually decrease. When the feed rate of PVA is 0.1 mL/h, the wall is $2.27 \mu\text{m}$ in thickness. As the core/shell feed rates increase to 1.5/1.7 mL/h, the wall thickness is reduced to $1.59 \mu\text{m}$. The feed rate of inner liquid exhibits an apparent

effect on the fiber diameter and wall thickness. This effect is different from the results pertaining to the hollow electrospun fibers prepared by core/shell electrospinning followed by a core removal process [218,219]. In Refs. [209,218], the outer fiber diameter of the hollow fiber remains unchanged even the core feed rate increases several times. However, this phenomenon does not occur in PVDF/PVA electrospinning. Figure 10.3 shows a clear increase of outer diameter by increasing the core solution feed rate. The result demonstrates a viable methodology to control the size of the obtained PVDF/PVA hollow fibers.

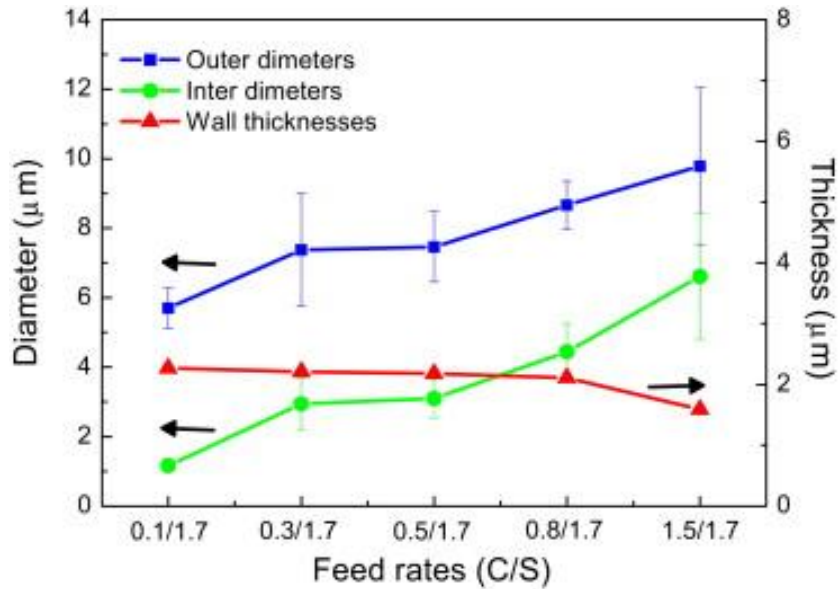


Figure 10.3 Diameters and wall thicknesses of the electrospun hollow fibers for different solution feed rates. The inner diameters of the PVDF/PVA hollow fibers increase from $1.16 \pm 0.15 \mu\text{m}$ to $6.61 \pm 1.80 \mu\text{m}$. The outer diameter increases slightly while the wall thickness of the PVDF/PVA decreases.

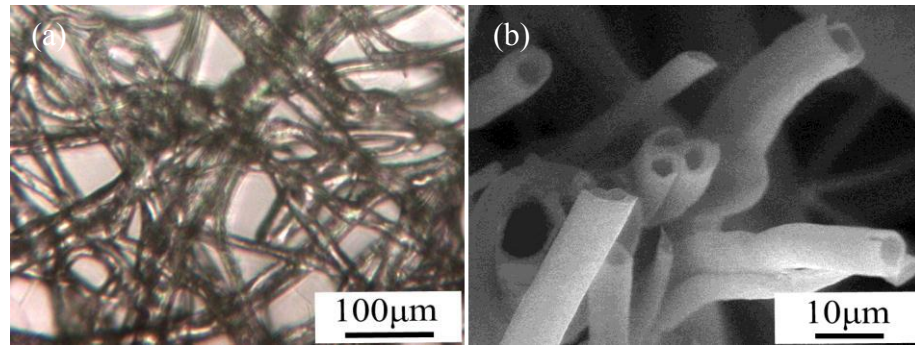


Figure 10.4 (a) An image of PVDF hollow fibers under transmission optical microscope. (b) A SEM image of PVDF hollow fibers taken from the view of cross-section.

10.5 Adhesion Test between Hollow Fibers and Rigid Substrate

SLBT test is performed to evaluate the adhesion energy between hollow fibrous membrane and rigid inorganic substrate. Five different samples are prepared under a flow rate of 1.5/1.7 mL/h. Central deflection vs. applied force can be found in Figure 10.5 (a). In the initial region, linear relationship can be observed, and the ratio of applied force to central deflection is used for adhesion energy calculation. A linear relationship between debonding radius and central deflection is also established, and used for further calculation, as shown in Figure 10.5 (b). The adhesion energy calculated from Figure 10.5 is $142.8 \pm 57.9 \text{ mJ/m}^2$.

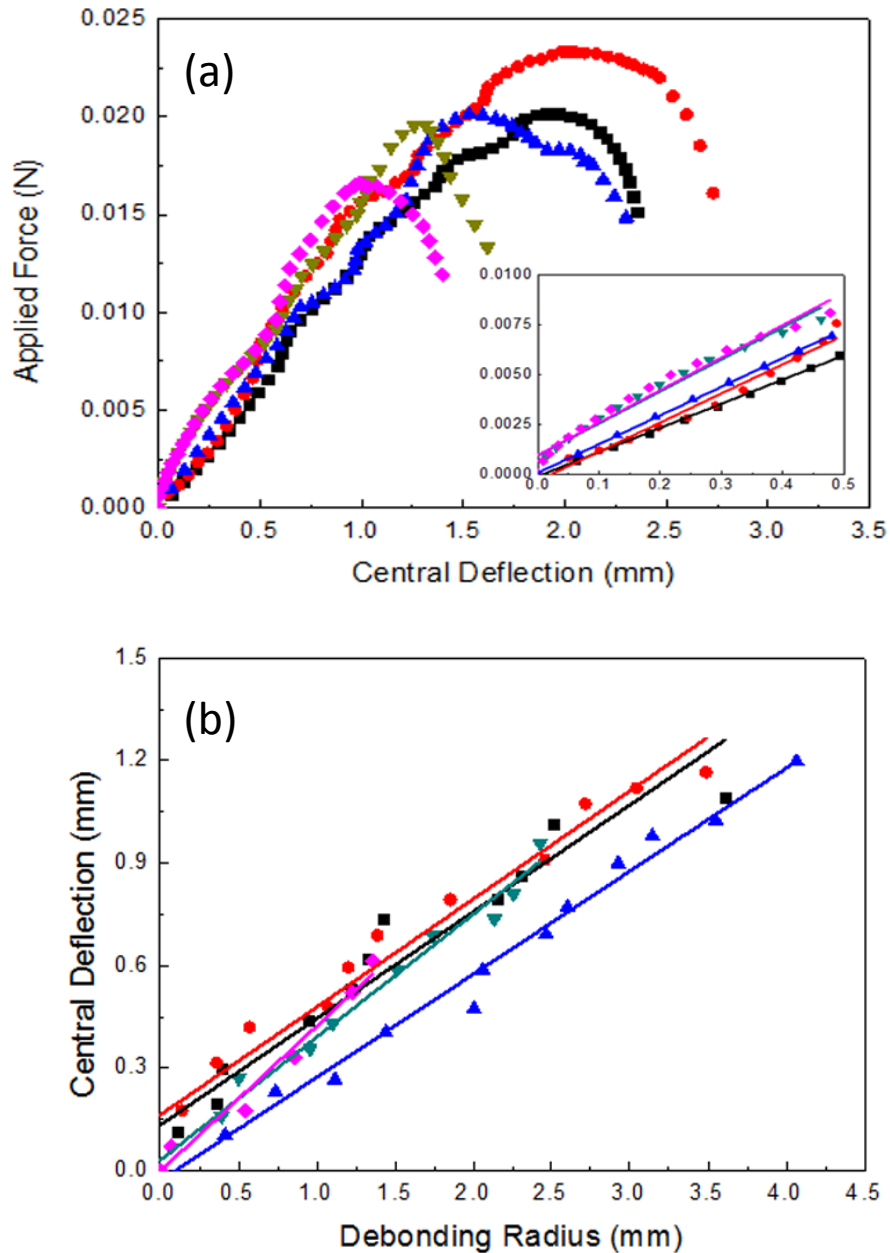


Figure 10.5 Output of adhesion tests. Five different samples are tested under some test conditions. (a) Applied force vs. central deflection. (b) Debonding radius vs. central deflection.

As discussed in Chapter 7, the adhesion energy decreased dramatically with fiber diameter decreasing. The adhesion energy is as low as 8.06 ± 0.71 mJ/m² when fiber

diameter is $2.724 \pm 0.587 \mu\text{m}$. However, the hollow fiber diameter in Figure 10.4 is $5.70 \pm 0.59 \mu\text{m}$, but the adhesion energy can still keep relative high value as $142.8 \pm 57.9 \text{ mJ/m}^2$. The reason for the high value of adhesion energy is attributed to the hollow structure. The hollow structure increase the flexibility of the membrane, compare to the membrane assembled by solid fiber with same diameter as outer diameter in hollow fiber. Najem [148] has studied the effect of bending stiffness on adhesion strength. Bending stiffness diminishes when the fiber diameter increasing, and lower bending stiffness causes an enhancement in real contact area between the fibers and substrate, and thus the adhesion strength is enhanced. Elsner and co-workers [220] has the similar explanation to the hollow microcapsule. They believe the adhesion energy between hollow capsule and solid substrate highly depended on the thickness of the hollow capsule in case of small deformation happens. The wall thickness (h) directly influents the radius of adhesion contact area (R_{ad}),

$$R_{ad} = \sqrt{\frac{2\sqrt{12}\pi R^3 \gamma}{Eh^2}} \quad \text{Equation 10.1}$$

where R is the radius of the capsule, γ is the surface energy and E is the elastic modulus. R_{ad} has a relationship with the work of adhesion,

$$W = \pi R_{ad}^2 \gamma \quad \text{Equation 10.2}$$

From Equation 10.1 and 10.2, we can find the strong dependency of the work of adhesion in the capsule thickness. The wall thickness of tested hollow PVDF fibers is roughly $2.27 \mu\text{m}$, therefore the effective cross-sectional diameter is twice the walk

thickness, as $4.54\mu\text{m}$. Figure 10.6 illustrates the equivalent fiber diameter need to be $\sim 0.88\mu\text{m}$ for adhesion energy of $142.8\pm 57.9\text{ mJ/m}^2$. In the other hand, adhesion energy for a solid fibers with diameter of $4.54\mu\text{m}$ would be approaching to zero according Figure 10.6. Apparently hollow structure effectively enhanced the adhesion performance, even only compare the wall thickness with solid fibers.

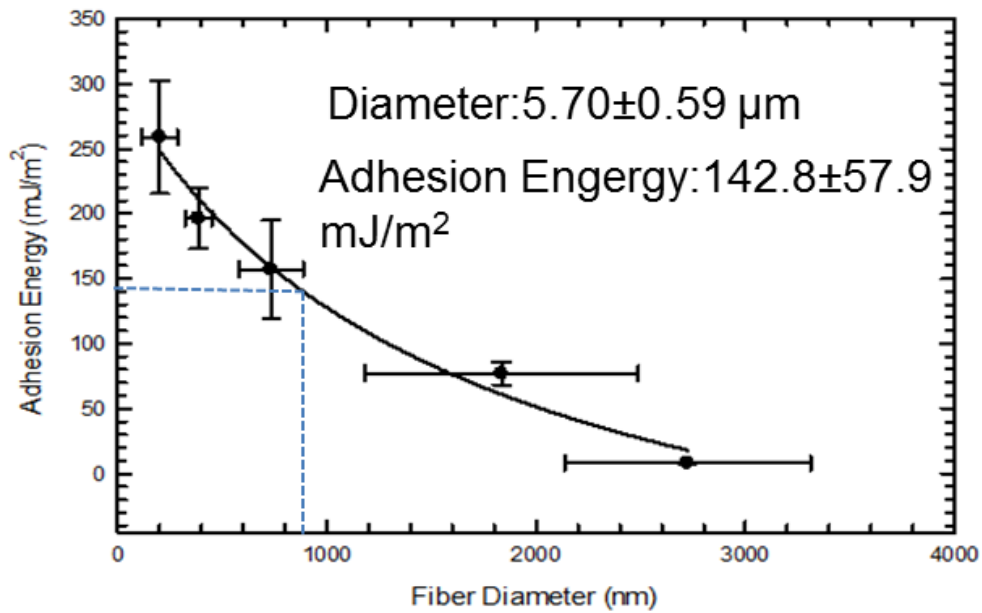


Figure 10.6 Relationship between fiber diameter of solid PVDF fiber and adhesion energy. The horizontal dash lines represent the adhesive energy of tested hollow PVDF fibrous membrane at $142.8 \pm 57.9\text{ mJ/m}^2$, and the vertical dash lines represent the equivalent fiber diameter for solid fibers at $142.8 \pm 57.9\text{ mJ/m}^2$.

10.6 Crystalline Structures of PVDF Hollow Fibers

PVDF has three crystalline structures depending on the preparation conditions [143], i.e., form I (β type crystalline in planar zigzag conformation, orthorhombic), form II (α -type crystalline in TGTG, monoclinic), and form III (γ -type crystalline in TTTGTTTG, monoclinic) [12.166]. Generally, β -type crystallites form of PVDF is mainly produced in

tensile orientation. α -type crystallites appear in melt crystallization process. FTIR and XRD are always used to analyze the forms of crystallites of PVDF.

Recently PVDF is processed by co-axial electrospinning to produce micro-tube [221]. FTIR spectra of PVDF in the electrospun hollow fibers prepared at different core/shell feed rates are shown in Figure 10.6. The strong peaks at 840 cm^{-1} and 1275 cm^{-1} are the characteristic bands of β -phase crystallites of PVDF. No observable peaks appear at 975 cm^{-1} , 795 cm^{-1} and 764 cm^{-1} . The results indicate that α -type PVDF crystal does not exist in hollow electrospun fibers [169]. A small peak is detected at 1234 cm^{-1} , which is recognized as γ -type PVDF crystallite [222]. Figure 10.7 shows the XRD diffraction patterns of PVDF in the electrospun hollow fibers prepared under different feed rates. PVDF shows similar crystalline structures including one major peak at $2\theta = 20.6^\circ$ and a minor peaks at $2\theta = 36.0^\circ$. They are recognized as the characteristic peaks of β -type crystallite form of PVDF. At $2\theta = 18.4^\circ$ in XRD diffractions, slight band can be observed. There are no observable peaks $2\theta = 27.4^\circ$ in XRD diffractions. The XRD results corroborate the FTIR findings that no perfect α -form crystallites exist in PVDF [120]. Another minor peak found at $2\theta = 40.0^\circ$ exhibits a small trace of γ -type PVDF crystallite [223]. During the co-axial electrospinning process, amount of excess charges exist on the surface of polymer solution jet. A strong electrostatic repulsion could be produced by these charges [224]. The electrostatic repulsion extends the polymer solution into a long thin nanofiber. In this process, the molecular chain of PVDF is stretched to form an oriented structure without any melt crystallization. As a result, β -type crystallite dominates in electrospun PVDF.

The principal rationale for piezoelectricity in PVDF is related to its crystal polymorphism [117]. There are two proposed mechanisms by use of trapped charges and orientation of dipoles to explain the relationship between the structures and the piezoelectric or pyroelectric effects associated with PVDF [225]. The most desirable form with the highest piezoelectricity of PVDF is the polar β form [226-227]. The increase of β -type crystallites can effectively enhance the piezoelectricity of the electrospun hollow fibers [122-123].

β -phase PVDF operates as nonlinear dielectrics; the surface charge density increases non-linearly with the electric field. An applied sinusoidal electric field to PVDF will result in repeated cycles of hysteresis loop, allowing PVDF to exhibit ferroelectric switching of dipoles. Poling occur whereby the dipoles within the crystalline regions will re-orientate, giving a strong dipole moment and large “remnant” polarization. This large remnant polarization is required for PVDF to fully exhibit its piezoelectricity. Co-axial electrospinning of thin-walled cylindrical hollow fibers as in this study provides a perfect scheme for enhancing (i) the amount of β -phase crystals in PVDF; (ii) remnant polarization and thus poling, (iii) degree of crystallinity and (iv) alignment of molecular chains, which are all essential to piezoelectricity for PVDF hollow fibers as we suggested in this study. The potential application of flexible hollow fibers can be improved with the increase of electro-mechanical coupling using fluid filled hollow fibers.

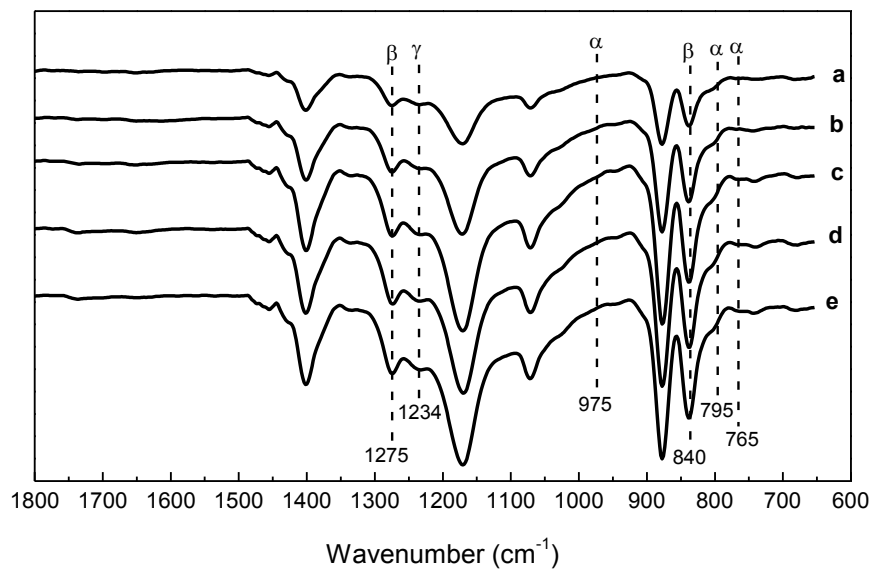


Figure 10.7 FTIR spectra of PVDF in the electrospun hollow fibers prepared at different core/shell feed rates (mL/h) at (a) 0.1/1.7, (b) 0.3/1.7, (c) 0.5/1.7, (d) 0.8/1.7, and (e) 1.5/1.7, respectively.

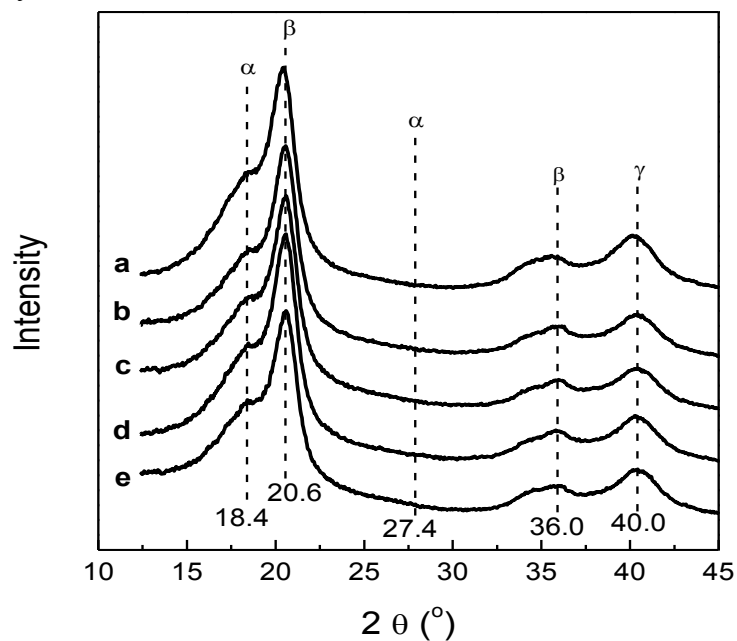


Figure 10.8 XRD patterns of PVDF in the electrospun hollow fibers prepared at different core/shell feed rates (mL/h) at (a) 0.1/1.7, (b) 0.3/1.7, (c) 0.5/1.7, (d) 0.8/1.7, and (e) 1.5/1.7, respectively.

10.7 Conclusions

A process based on coaxial electrospinning is exploited to fabricate PVDF/PVA hollow fibers. This technique consisted of two objectives, viz., (i) hollow fiber formation and (ii) mitigation of secondary erosion. Using this methodology, the prepared membrane with PVDF hollow fibers exhibited better adhesion property compared to membranes assembled by solid fibers. The effect of wall thickness on melting peak, heat of fusion, crystallinity and polymorphism of PVDF was studied. As the wall thickness decreases, the degree of crystallinity increases. β -form crystallite dominates in PVDF hollow fibers. The XRD results corroborated those data obtained from FTIR. Hollow structures can effectively improve the adhesion performance compared to solid fibers in same size. Further study could be performed to investigate the adhesion property in a function of fiber wall thickness. The adhesion performance of the hollow fiber can be evolved to become controllable by controlling the property of the possible filled-in fluids.

CHAPTER XI

SUMMARY

11.1 Conclusions

SLBT is an effective method to characterize adhesion property of electrospun membranes adhered to inorganic or organic substrate. In this study, theory of SLBT is established analytically and numerically.

Experimental work includes adhesion tests between PVDF electrospun membrane and rigid inorganic substrate. Our electrospun PVDF membranes exhibited a linear elastic deformation at a small external load, and the elastic modulus is found from SLBT to be 23.42 ± 2.69 MPa, which is consistent with the value obtained from a standard tensile test. The adhesion energy determined by SLBT is 206 ± 26 mJ/m², which is almost 4 times larger than the adhesion energy between gecko seta and Si [1, 4]. Ten times repeatable tests are performed to ensure the reusability of the electrospun membrane.

Different sizes of PVDF fiber are electrospun from different solution conditions. Adhesion energy is evaluated for membranes contained different size of fibers. Thinner fibers can make better contact with substrate asperities, and then possess higher adhesion energy. DSC results show higher crystallinity of thinner fibers. Membranes from different thickness are also evaluated for their adhesion

energy, thick membrane possesses lower adhesion energy, because the bending moment of thick film can consume more adhesion energy.

Effect of substrate topography is also investigated by testing substrates with different grits on surface. The substrate exhibits different roughness, and adhesion energy trends to increase when the mean peak and valley roughness (R_z) increase. The experimental results coincide with the prediction by mechanical interlocking theory. Effect of loading speed is evaluated, however, no obvious effect of speed can be observed on adhesion energy, when loading speed varies from 0.1 mm/s to 2mm/s.

The adhesion energy of electrospun PCL membranes is also evaluated. The adhesion energy between electrospun PCL membranes is ~30 % higher than the adhesion energy of electrospun PCL membrane with cast PCL film. Significant self-interlocking effect of PCL membrane is observed. Electrospun membrane together with its fiber morphology provides an ideal model to increase adhesion property of thin membranes, which can be potential used for nano-connector.

PVDF hollow fibers prepared from co-axial electrospinning has the potential application on smart fiber. Hollow fiber has the capacity to fill functional liquid in, and perform like gecko to extend, contract and move its foot hair. The prepared membrane with PVDF fibers exhibited better adhesion property compared to membranes assembled by solid fibers. Hollow structure provides more flexibility to membrane, therefore better contact with substrate can be achieved.

Overall, Adhesion properties of electrospun polymer adhesives are systematically studied in this work. SLBT is used for the first time in adhesive energy determination of

electrospun polymers membrane. Several important parameters are investigated, such as fiber diameter, fiber structure, substrate roughness, substrate materials etc. The adhesion energy of electrospun fibers are controllable under controlling with different parameters. However, adhesion mechanism of electrospun membrane is not well understood.

11.2 Suggestion for Future Work

Future work will have two major focuses. One is the theoretical modeling study; the other is the application development. The mechanism of adhesion is complex, and no single adhesion theory can be applied to explain the adhesion phenomenon between electrospun membranes and various substrates. In order to understand the theory of electrospun membrane adhesion, more experimental work needs to be performed. By testing membranes with different physical properties, adhesion energy can be accurately correlated to membrane's physical property. To be specific, membrane's elastic modulus, in-plane friction coefficient, viscoelasticity can be studied.

FEA is the powerful modeling tool for continuous materials. In our study, electrospun membrane is treated as thin smooth membrane with a given adhesion energy. For the electrospun membranes, FEA cannot effectively represent membrane's surface morphology, cross-linking of fibers and even the molecular structure of fibers. Therefore, a number of variational parameters cannot be well addressed by FEA modeling. In order to consider fiber's molecular structure, molecular dynamic (MD) simulation could be used to simulate the physical movements of the molecules. Wei and co-workers [228] demonstrated a bead model to represent electrospun fibers, as shown in Figure 11.1. A

series of connected beads is adopted to simulate a nanofiber, and the fibers are randomly distributed to a square space. A MD simulation study has been done to investigate the tensile property of electrospun membranes. The MD simulation, as cited from Wei and co-workers can be recognized as a meso scale simulation, which uses the microscale molecular movement to represent physical properties of macroscale materials. More detail description of meso scale simulation can be found in [229]. Future work of adhesion research could utilize the tool of MD simulation, and to consider more variational conditions for adhesion contact.

Adhesion science is a kind of fundamental research topic. After understanding the adhesion mechanisms of electrospun membranes, it is urgent to convert the research results to meaningful application products. The Chapter VIII has proposed a new way to make nano-connectors, which is inspired by Velcro®. The optimistic electrospun fibers for nano-connector need to be flexible, strong and durable. The following study needs to elaborate on electrospinning to improve fibers' quality and uniformity, in order to achieve better adhesion strength.

Table 1.1.1 Comparison of adhesion energy with literature.

Materials	Test Method	Adhesion Energy (mJ m^{-2})	Investigators
Gecko setae	Pull-off from MEMS sensor	50-60	Autumn et al. 2002 [3]
PCL film	JKR pull-off	26.5	Johnson, KL 1971 [71]
Nylon 6 fiber	AFM cantilever pull-off	71.0±13.3	Wang X, 2012 [169]
PCL electrospun fiber	Nano Binox pull-off	190±7	Shi et al. 2010 [8]
PVDF electrospun membrane contacted with inorganic cardboard	SLBT	8-259 (various fiber diameters)	This Work
	SLBT	42.8±57.9 (hollow fiber)	
PCL electrospun membrane	SLBT	305.0±41.9 (with same membrane)	This Work
	SLBT	206.7±45.2 mJ/m^2 (with PCL cast film)	

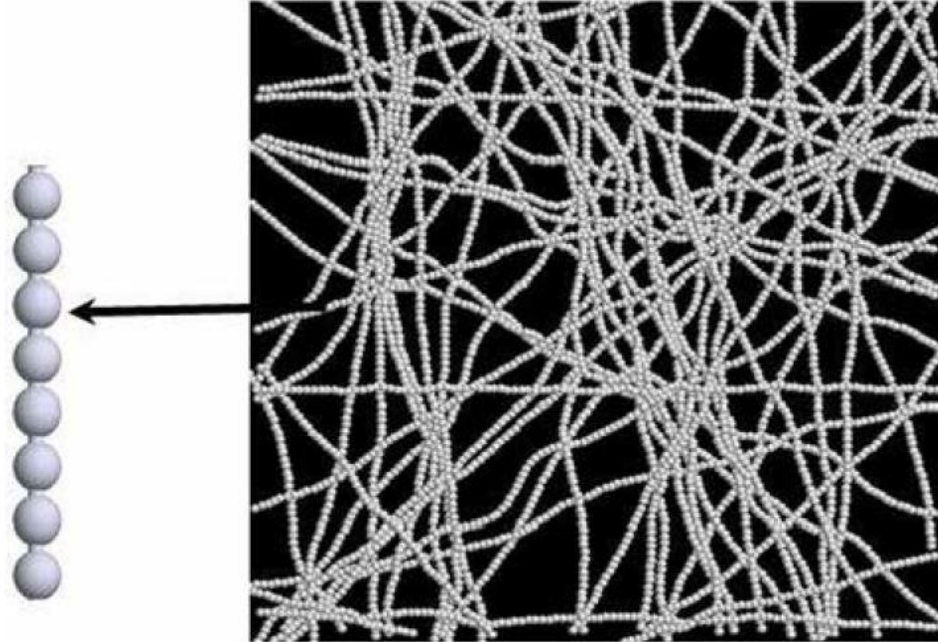


Figure 11.1 Randomly oriented electrospun fibers are modeled as a network of randomly distributed fibers. Each fiber is considered as a connection of multiple beads (reprinted with permission from Inderscience) [228].

The other application discussed in the dissertation is the adhesion of hollow electrospun fibers. The improvement of adhesion property by fabricating hollow fiber structure is demonstrated in Chapter IV. The following research needs to be focused on mimicking the movement of gecko foot hair. Giant electrorheological (GER) fluids [230-232] are suspensions with functional nano-particles inside. GER fluids can change their materials' flow property through an electrical field [232], which can show electrically controllable liquid-solid transitions. The following research could fill GER into the electrospun hollow fibers, and then the movement of the fibers could become controllable

by electrical field. Since the wall of the hollow fiber is built with piezoelectric materials (PVDF), therefore the actuation could be accomplished by stretching or bending PVDF fibers simultaneously [233-235]. More electrical responsive materials can be considered to fill in the piezoelectric fibers for other piezoelectric applications [236].

REFERENCES

1. Autumn, K., Liang, Y. A., Hsieh, S. T., Zesch, W., Chan, W. P., Kenny, T. W., ... & Full, R. J. (2000). Adhesive force of a single gecko foot-hair. *Nature*, 405(6787), 681-684.
2. Gao, H., & Yao, H. (2004). Shape insensitive optimal adhesion of nanoscale fibrillar structures. *Proceedings of the National Academy of Sciences of the United States of America*, 101(21), 7851-7856.
3. Autumn, K., Sitti, M., Liang, Y. A., Peattie, A. M., Hansen, W. R., Sponberg, S., ... & Full, R. J. (2002). Evidence for van der Waals adhesion in gecko setae. *Proceedings of the National Academy of Sciences*, 99(19), 12252-12256.
4. Sitti, M., & Fearing, R. S. (2002). Nanomolding based fabrication of synthetic gecko foot-hairs. In *Nanotechnology, 2002. IEEE-NANO 2002. Proceedings of the 2002 2nd IEEE Conference on* (pp. 137-140). IEEE.
5. Sethi, S., Ge, L., Ci, L., Ajayan, P. M., & Dhinojwala, A. (2008). Gecko-inspired carbon nanotube-based self-cleaning adhesives. *Nano letters*, 8(3), 822-825.
6. Lee, H. J., Kim, J. H., Cho, K. H., Hyun, S. M., Kim, J. Y., Yoo, Y. E., & Kim, W. D. (2007). Adhesion Test of Nanostructured Materials by a Novel AFM Probe. *Key Engineering Materials*, 353, 2253-2256.
7. Huber, G., Gorb, S. N., Spolenak, R., & Arzt, E. (2005). Resolving the nanoscale adhesion of individual gecko spatulae by atomic force microscopy. *Biology Letters*, 1(1), 2-4.
8. Shi, Q., Wan, K. T., Wong, S. C., Chen, P., & Blackledge, T. A. (2010). Do electrospun polymer fibers stick?. *Langmuir*, 26(17), 14188.
9. Ford, T. A. (1948). *U.S. Patent No. 2,435,537*. Washington, DC: U.S. Patent and Trademark Office.
10. Fukada, E. (1974). Piezoelectric properties of organic polymers. *Annals of the New York Academy of Sciences*, 238(1), 7-25.

11. Na, H., Li, Q., Sun, H., Zhao, C., & Yuan, X. (2009). Anisotropic mechanical properties of hot - pressed PVDF membranes with higher fiber alignments via electrospinning. *Polymer Engineering & Science*, 49(7), 1291-1298.
12. Na, H., Zhao, Y., Zhao, C., Zhao, C., & Yuan, X. (2008). Effect of hot - press on electrospun poly (vinylidene fluoride) membranes. *Polymer Engineering & Science*, 48(5), 934-940.
13. Wadley, L., Hodgskiss, T., & Grant, M. (2009). Implications for complex cognition from the hafting of tools with compound adhesives in the Middle Stone Age, South Africa. *Proceedings of the National Academy of Sciences*, 106(24), 9590-9594.
14. A Pizzi, K. L. Mittal (2003). Handbook of Adhesive Technology. *Marcel Dekker, Inc*, New York.
15. Petrie, E. M. (2000). *Handbook of adhesives and sealants* (p. 615). New York: McGraw-Hill.
16. Gillies, A. G., & Fearing, R. S. (2011). Shear Adhesion Strength of Thermoplastic Gecko-Inspired Synthetic Adhesive Exceeds Material Limits. *Langmuir*, 27(18), 11278-11281.
17. Lee, J., Majidi, C., Schubert, B., & Fearing, R. S. (2008). Sliding-induced adhesion of stiff polymer microfibre arrays. I. Macroscale behaviour. *Journal of The Royal Society Interface*, 5(25), 835-844.
18. Lee, J., & Fearing, R. S. (2008). Contact self-cleaning of synthetic gecko adhesive from polymer microfibers. *Langmuir*, 24(19), 10587-10591.
19. Lee, J., Fearing, R. S., & Komvopoulos, K. (2008). Directional adhesion of gecko-inspired angled microfiber arrays. *Applied Physics Letters*, 93(19), 191910-191910.
20. Jeong, H. E., & Suh, K. Y. (2009). Nanohairs and nanotubes: Efficient structural elements for gecko-inspired artificial dry adhesives. *Nano Today*, 4(4), 335-346.
21. Jeong, H. E., Lee, J. K., Kim, H. N., Moon, S. H., & Suh, K. Y. (2009). A nontransferring dry adhesive with hierarchical polymer nanohairs. *Proceedings of the National Academy of Sciences*, 106(14), 5639-5644.
22. Qu, L., & Dai, L. (2007). Gecko - Foot - Mimetic Aligned Single - Walled Carbon Nanotube Dry Adhesives with Unique Electrical and Thermal Properties. *Advanced materials*, 19(22), 3844-3849.
23. Qu, L., Dai, L., Stone, M., Xia, Z., & Wang, Z. L. (2008). Carbon nanotube arrays with strong shear binding-on and easy normal lifting-off. *Science*, 322(5899), 238-242.

24. Mahdavi, A., Ferreira, L., Sundback, C., Nichol, J. W., Chan, E. P., Carter, D. J., ... & Karp, J. M. (2008). A biodegradable and biocompatible gecko-inspired tissue adhesive. *Proceedings of the National Academy of Sciences*, 105(7), 2307-2312.
25. Geim, A. K., Grigorieva, S. D. I., Novoselov, K. S., Zhukov, A. A., & Shapoval, S. Y. (2003). Microfabricated adhesive mimicking gecko foot-hair. *Nature materials*, 2(7), 461-463.
26. Aksak, B., Murphy, M. P., & Sitti, M. (2007). Adhesion of biologically inspired vertical and angled polymer microfiber arrays. *Langmuir*, 23(6), 3322-3332.
27. Murphy, M. P., Aksak, B., & Sitti, M. (2008). Gecko - Inspired Directional and Controllable Adhesion. *Small*, 5(2), 170-175.
28. Jeong, H. E., Lee, S. H., Kim, P., & Suh, K. Y. (2006). Stretched polymer nanohairs by nanodrawing. *Nano letters*, 6(7), 1508-1513.
29. Ge, L., Sethi, S., Ci, L., Ajayan, P. M., & Dhinojwala, A. (2007). Carbon nanotube-based synthetic gecko tapes. *Proceedings of the National Academy of Sciences*, 104(26), 10792-10795.
30. Sitti, M. (2003, July). High aspect ratio polymer micro/nano-structure manufacturing using nanoembossing, nanomolding and directed self-assembly. In *Advanced Intelligent Mechatronics, 2003. AIM 2003. Proceedings. 2003 IEEE/ASME International Conference on (Vol. 2, pp. 886-890)*. IEEE.
31. Schaffer, E., Thurn-Albrecht, T., Russell, T. P., & Steiner, U. (2000). Electrically induced structure formation and pattern transfer. *Nature*, 403(6772), 874-877.
32. Hansen, W. R., & Autumn, K. (2005). Evidence for self-cleaning in gecko setae. *Proceedings of the National Academy of Sciences of the United States of America*, 102(2), 385-389.
33. Autumn, K., Majidi, C., Groff, R. E., Dittmore, A., & Fearing, R. (2006). Effective elastic modulus of isolated gecko setal arrays. *Journal of Experimental Biology*, 209(18), 3558-3568.
34. Majidi, C., Groff, R. E., Maeno, Y., Schubert, B., Baek, S., Bush, B., ... & Fearing, R. S. (2006). High friction from a stiff polymer using microfiber arrays. *Physical review letters*, 97(7), 76103.
35. Tian, Y., Pesika, N., Zeng, H., Rosenberg, K., Zhao, B., McGuiggan, P., ... & Israelachvili, J. (2006). Adhesion and friction in gecko toe attachment and detachment. *Proceedings of the National Academy of Sciences*, 103(51), 19320-19325.

36. Autumn, K., Dittmore, A., Santos, D., Spenko, M., & Cutkosky, M. (2006). Frictional adhesion: a new angle on gecko attachment. *Journal of Experimental Biology*, 209(18), 3569-3579.
37. Daltorio, K. A., Gorb, S., Peressadko, A., Horchler, A. D., Ritzmann, R. E., & Quinn, R. D. (2006). A robot that climbs walls using micro-structured polymer feet. *Climbing and Walking Robots*, 131-138.
38. Aksak, B., Murphy, M. P., & Sitti, M. (2008, May). Gecko inspired micro-fibrillar adhesives for wall climbing robots on micro/nanoscale rough surfaces. In *Robotics and Automation, 2008. ICRA 2008. IEEE International Conference on* (pp. 3058-3063). IEEE.
39. Cutkosky, M. R., & Kim, S. (2009). Design and fabrication of multi-material structures for bioinspired robots. *Philosophical Transactions of the Royal Society A: Mathematical, Physical and Engineering Sciences*, 367(1894), 1799-1813.
40. Sitti, M., & Fearing, R. S. (2003). Synthetic gecko foot-hair micro/nano-structures as dry adhesives. *Journal of Adhesion Science and Technology*, 17(8), 1055-1073.
41. Yurdumakan, B., Raravikar, N. R., Ajayan, P. M., & Dhinojwala, A. (2005). Synthetic gecko foot-hairs from multiwalled carbon nanotubes. *Chemical Communications*, (30), 3799-3801.
42. Israelachvili, J. N. (2011). *Intermolecular and surface forces: revised third edition*. Academic press.
43. Lee, L. H. (Ed.). (1991). *Fundamentals of adhesion*. Springer.
44. Allara, D. L., Fowkes, F. M., Noolandi, J., Rubloff, G. W., & Tirrell, M. V. (1986). Bonding and adhesion of polymer interfaces. *Mater. Sci. Eng.*, 83(2), 213-226.
45. Fowkes, F. M., Dwight, D. W., Cole, D. A., & Huang, T. C. (1990). Acid-base properties of glass surfaces. *Journal of Non-Crystalline Solids*, 120(1), 47-60.
46. Fowkes, F. M. (1987). Role of acid-base interfacial bonding in adhesion. *Journal of Adhesion Science and Technology*, 1(1), 7-27.
47. Clearfield, H. M., McNamara, D. K., & Davis, G. D. (1991). Adherend surface preparation for structural adhesive bonding. *Adhesive Bonding*, 203-237.
48. Jennings, C. W. (1972). Surface roughness and bond strength of adhesives. *The Journal of Adhesion*, 4(1), 25-38.
49. Sharpe, L. H., & Schonhorn, H. (1964). *Advances in Chemistry Series*, 43, American Chemical Society, Washington, 189.
50. Gent, A. N., & Lin, C. W. (1990). Model studies of the effect of surface roughness and mechanical interlocking on adhesion. *The Journal of Adhesion*, 32(2-3), 113-125.

51. Voyutskii, S. (1963). *Autohesion and adhesion of high polymers*. Interscience Publ..
52. Roberts, A. D. (2001). Surface charge contribution in rubber adhesion and friction. *Journal of Physics D: Applied Physics*, 10(13), 1801.
53. Possart, W. (1988). Experimental and theoretical description of the electrostatic component of adhesion at polymer/metal contacts. *International Journal of Adhesion and Adhesives*, 8(2), 77-83.
54. Bikerman, J. J. (1961). *The science of adhesive joints* (Vol. 7). New York: Academic Press.
55. Lee, L. H. (Ed.). (1973). *Recent advances in adhesion: proceedings*. Gordon & Breach Publishing Group.
56. Wu, S. (1982). *Polymer interface and adhesion*.
57. Dekker, M. Kendall, K. (2001). *Molecular adhesion and its applications: the sticky universe*. Springer.
58. Israelachvili, J. N. (2011). *Intermolecular and surface forces: revised third edition*. Academic press.
59. Derjaguin, B. V., Muller, V. M., & Toporov, Y. P. (1975). Effect of contact deformations on the adhesion of particles. *Journal of Colloid and interface science*, 53(2), 314-326.
60. Muller, V. M., Derjaguin, B. V., & Toporov, Y. P. (1983). On two methods of calculation of the force of sticking of an elastic sphere to a rigid plane. *Colloids and Surfaces*, 7(3), 251-259.
61. Johnson, K. L. (1987). *Contact mechanics*. Cambridge university press.
62. Shull, K. R. (2002). Contact mechanics and the adhesion of soft solids. *Materials Science and Engineering: R: Reports*, 36(1), 1-45.
63. Horn, R. G., Israelachvili, J. N., & Pribac, F. (1987). Measurement of the deformation and adhesion of solids in contact. *Journal of colloid and interface science*, 115(2), 480-492.
64. Tirrell, M. (1996). Measurement of interfacial energy at solid polymer surfaces. *Langmuir*, 12(19), 4548-4551.
65. Tabor, D. (1977). Surface forces and surface interactions. *Journal of Colloid and Interface Science*, 58(1), 2-13.
66. Pashley, M. D. (1984). Further consideration of the DMT model for elastic contact. *Colloids and surfaces*, 12, 69-77.

67. Greenwood, J. A. (1997). Adhesion of elastic spheres. *Proceedings of the Royal Society of London. Series A: Mathematical, Physical and Engineering Sciences*, 453(1961), 1277-1297.
68. Mittal, K. L. (1976). Adhesion measurement of thin films. *Active and Passive Electronic Components*, 3(1), 21-42.
69. Chapman, B. N. (1974). Thin-film adhesion. *Journal of Vacuum Science and Technology*, 11(1), 106-113.
70. Valli, J. (1986). A review of adhesion test methods for thin hard coatings. *Journal of Vacuum Science & Technology A: Vacuum, Surfaces, and Films*, 4(6), 3007-3014.
71. Kendall, K. (1971). The adhesion and surface energy of elastic solids. *Journal of Physics D: Applied Physics*, 4(8), 1186-1195.
72. Drory, M. D., & Hutchinson, J. W. (1995, January). An indentation test for measuring adhesion toughness of thin films under high residual compression with application to diamond films. In *MATERIALS RESEARCH SOCIETY SYMPOSIUM PROCEEDINGS* (Vol. 383, pp. 173-182). Materials Research Society.
73. Volinsky, A. A., Vella, J. B., & Gerberich, W. W. (2003). Fracture toughness, adhesion and mechanical properties of low- K dielectric thin films measured by nanoindentation. *Thin Solid Films*, 429(1), 201-210.
74. Landman, U., Luedtke, W. D., Burnham, N. A. N. C. Y. A., & COLTON, R. (1990). Atomistic mechanisms and dynamics of adhesion, nanoindentation, and fracture. *Science*, 248(4954), 454-461.
75. Kim, K. S., & Kim, J. (1988). Elasto-plastic analysis of the peel test for thin film adhesion. *Journal of Engineering Materials and Technology*, 110, 266.
76. Kim, J., Kim, K. S., & Kim, Y. H. (1989). Mechanical effects in peel adhesion test. *Journal of adhesion science and technology*, 3(1), 175-187.
77. Dannenberg, H. (1961). Measurement of adhesion by a blister method. *Journal of Applied Polymer Science*, 5(14), 125-134.
78. Anderson, G. P., Bennett, S. J., & DeVries, K. L. (1977). *Analysis and testing of adhesive bonds*. Academic Press.
79. Williams, M. L. (1969). The continuum interpretation for fracture and adhesion. *Journal of Applied Polymer Science*, 13(1), 29-40.
80. Bennett, S. J., Devries, K. L., & Williams, M. L. (1974). Adhesive fracture mechanics. *International Journal of Fracture*, 10(1), 33-43.

81. Hinkley, J. A. (1983). A blister test for adhesion of polymer films to SiO₂. *The Journal of Adhesion*, 16(2), 115-125.
82. Gent, A. N., & Lewandowski, L. H. (1987). Blow off pressures for adhering layers. *Journal of applied polymer science*, 33(5), 1567-1577.
83. Maseeh, F., & Senturia, S. D. (1990, June). Viscoelasticity and creep recovery of polyimide thin films. In *Solid-State Sensor and Actuator Workshop, 1990. 4th Technical Digest., IEEE* (pp. 55-60). IEEE.
84. Napolitano, M. J., Chudnovsky, A., & Moet, A. (1988). The constrained blister test for the energy of interfacial adhesion. *Journal of Adhesion Science and Technology*, 2(1), 311-323.
85. Chang, Y. S., Lai, Y. H., & Dillard, D. A. (1989). The Constrained Blister—A Nearly Constant Strain Energy Release Rate Test for Adhesives. *The Journal of Adhesion*, 27(4), 197-211.
86. Lai, Y. H., & Dillard, D. A. (1990). Numerical analysis of the constrained blister test. *The Journal of Adhesion*, 33(1-2), 63-74.
87. Dillard, D. A., & Chang, Y. S. (1987). *The Constrained Blister: A Novel Constant Strain Energy Release Rate Test for Adhesives*. Virginia Polytechnic Institute and State University.
88. Lai, Y. H., & Dillard, D. A. (1990). An elementary plate theory prediction for strain energy release rate of the constrained blister test. *The Journal of Adhesion*, 31(2-4), 177-189.
89. Allen, M. G. (1989). Measurement of adhesion and mechanical properties of thin films using microfabricated structures. PhD dissertation, *Massachusetts Institute of Technology*.
90. Allen, M. G., & Senturia, S. D. (1988). Analysis of critical debonding pressures of stressed thin films in the blister test. *The Journal of Adhesion*, 25(4), 303-315.
91. Allen, M. G., & Senturia, S. D. (1989). Application of the island blister test for thin film adhesion measurement. *The Journal of Adhesion*, 29(1-4), 219-231.
92. Allen, M. G., Nagarkar, P., & Senturia, S. D. (1988). Aspects of Adhesion Measurement of Thin Polyimide Films. In *Third Annual Conference on Polyimides, Ellenville, NY*.
93. Y. Boa, D. A. Dillard, H. F. Webster, J. P. Wrightman. (1992) Application of the peninsula blister test to measure adhesion of thin polymer films. *Proc of the 15th Annual Meeting of the Adhesion Society*.

94. Dillard, D. A., & Bao, Y. (1991). The peninsula blister test: a high and constant strain energy release rate fracture specimen for adhesives. *The Journal of Adhesion*, 33(4), 253-271.
95. K. M. Liechti, A. Shirani(1993) Nonlinear plate analysis of thin film blistering. *Proc of the Adhesion Soc.*
96. Baji, A., Mai, Y. W., Wong, S. C., Abtahi, M., & Chen, P. (2010). Electrospinning of polymer nanofibers: Effects on oriented morphology, structures and tensile properties. *Composites science and technology*, 70(5), 703-718.
97. Kongkhleng, T., Tashiro, K., Kotaki, M., & Chirachanchai, S. (2008). Electrospinning as a new technique to control the crystal morphology and molecular orientation of polyoxymethylene nanofibers. *Journal of the American Chemical Society*, 130(46), 15460-15466.
98. Lim, C. T., Tan, E. P. S., & Ng, S. Y. (2008). Effects of crystalline morphology on the tensile properties of electrospun polymer nanofibers. *Applied Physics Letters*, 92(14), 141908.
99. Baji, A., Wong, S. C., Blackledge, T. A., Leng, S. (2008). Mechanical properties of electrospun composites and their crystallinity measurements using X-ray diffraction. *ANTEC Conf Proc*, 12, 14–24.
100. Chen, P., Hague, S., Na, H., Wong, S. C. (2010). Piezoelectrical and mechanical properties of electrospun PVDF nanofiber” *Poster Presentation of MRS Fall Meeting 2010, Boston.*
101. Koombhongse, S., Liu, W., & Reneker, D. H. (2001). Flat polymer ribbons and other shapes by electrospinning. *Journal of Polymer Science Part B: Polymer Physics*, 39(21), 2598-2606.
102. Yarin, A. L., Kataphinan, W., & Reneker, D. H. (2005). Branching in electrospinning of nanofibers. *Journal of applied physics*, 98(6), 064501.
103. Bognitzki, M., Czado, W., Frese, T., Schaper, A., Hellwig, M., Steinhart, M., ... & Wendorff, J. H. (2001). Nanostructured fibers via electrospinning. *Advanced Materials*, 13(1), 70-72.
104. Megelski, S., Stephens, J. S., Chase, D. B., & Rabolt, J. F. (2002). Micro-and nanostructured surface morphology on electrospun polymer fibers. *Macromolecules*, 35(22), 8456-8466.
105. Casper, C. L., Stephens, J. S., Tassi, N. G., Chase, D. B., & Rabolt, J. F. (2004). Controlling surface morphology of electrospun polystyrene fibers: Effect of humidity and molecular weight in the electrospinning process. *Macromolecules*, 37(2), 573-578.

106. Li, D., Ouyang, G., McCann, J. T., & Xia, Y. (2005). Collecting electrospun nanofibers with patterned electrodes. *Nano letters*, 5(5), 913-916.
107. Dersch, R., Liu, T., Schaper, A. K., Greiner, A., & Wendorff, J. H. (2003). Electrospun nanofibers: Internal structure and intrinsic orientation. *Journal of Polymer Science Part A: Polymer Chemistry*, 41(4), 545-553.
108. Huang, Z. M., Zhang, Y. Z., Kotaki, M., & Ramakrishna, S. (2003). A review on polymer nanofibers by electrospinning and their applications in nanocomposites. *Composites science and technology*, 63(15), 2223-2253.
109. Fridrikh, S. V., Yu, J. H., Brenner, M. P., & Rutledge, G. C. (2003). Controlling the fiber diameter during electrospinning. *Physical review letters*, 90(14), 144502.
110. Tao, J., & Shivkumar, S. (2007). Molecular weight dependent structural regimes during the electrospinning of PVA. *Materials letters*, 61(11), 2325-2328.
111. Eda, G., & Shivkumar, S. (2006). Bead structure variations during electrospinning of polystyrene. *Journal of materials science*, 41(17), 5704-5708.
112. Fong, H., Chun, I., & Reneker, D. H. (1999). Beaded nanofibers formed during electrospinning. *Polymer*, 40(16), 4585-4592.
113. Baumgarten, P. K. (1971). Electrostatic spinning of acrylic microfibers. *Journal of colloid and interface science*, 36(1), 71-79.
114. Doshi, J., & Reneker, D. H. (1995). Electrospinning process and applications of electrospun fibers. *Journal of electrostatics*, 35(2), 151-160.
115. Fong, H., & Reneker, D. H. (1999). Elastomeric nanofibers of styrene-butadiene-styrene triblock copolymer. *Journal of Polymer Science Part B Polymer Physics*, 37, 3488-3493.
116. Bognitzki, M., Czado, W., Frese, T., Schaper, A., Hellwig, M., Steinhart, M., ... & Wendorff, J. H. (2001). Nanostructured fibers via electrospinning. *Advanced Materials*, 13(1), 70-72.
117. Zong, X., Kim, K., Fang, D., Ran, S., Hsiao, B. S., & Chu, B. (2002). Structure and process relationship of electrospun bioabsorbable nanofiber membranes. *Polymer*, 43(16), 4403-4412.
118. Lee, K. H., Kim, H. Y., La, Y. M., Lee, D. R., & Sung, N. H. (2002). Influence of a mixing solvent with tetrahydrofuran and N, N - dimethylformamide on electrospun poly (vinyl chloride) nonwoven mats. *Journal of Polymer Science Part B: Polymer Physics*, 40(19), 2259-2268.

119. Deitzel, J. M., Kleinmeyer, J., Harris, D., & Beck Tan, N. C. (2001). The effect of processing variables on the morphology of electrospun nanofibers and textiles. *Polymer*, *42*(1), 261-272.
120. Megelski, S., Stephens, J. S., Chase, D. B., & Rabolt, J. F. (2002). Micro- and nanostructured surface morphology on electrospun polymer fibers. *Macromolecules*, *35*(22), 8456-8466.
121. http://en.wikipedia.org/wiki/Polyvinylidene_fluoride
122. Costa, L. M. M., Bretas, R. E. S., & Gregorio, R. (2010). Effect of Solution Concentration on the Electrospray/Electrospinning Transition and on the Crystalline Phase of PVDF. *Materials Sciences and Applications*, *1*(4), 247-252.
123. Kim, Y. T., & Baek, C. K. (2003). Electrospinning of poly (vinylidene fluoride)/dimethylformamide solutions with carbon nanotubes. *Journal of Polymer Science Part B: Polymer Physics*, *41*(13), 1572-1577.
124. Choi, S. W., Kim, J. R., Ahn, Y. R., Jo, S. M., & Cairns, E. J. (2007). Characterization of electrospun PVDF fiber-based polymer electrolytes. *Chemistry of materials*, *19*(1), 104-115.
125. Lee, J. S., Choi, K. H., Ghim, H. D., Kim, S. S., Chun, D. H., Kim, H. Y., & Lyoo, W. S. (2004). Role of molecular weight of atactic poly (vinyl alcohol)(PVA) in the structure and properties of PVA nanofabric prepared by electrospinning. *Journal of Applied Polymer Science*, *93*(4), 1638-1646.
126. Wannatong, L., Sirivat, A., & Supaphol, P. (2004). Effects of solvents on electrospun polymeric fibers: preliminary study on polystyrene. *Polymer International*, *53*(11), 1851-1859.
127. Yee, W. A., Kotaki, M., Liu, Y., & Lu, X. (2007). Morphology, polymorphism behavior and molecular orientation of electrospun poly (vinylidene fluoride) fibers. *Polymer*, *48*(2), 512-521.
128. Zhao, Z., Li, J., Yuan, X., Li, X., Zhang, Y., & Sheng, J. (2005). Preparation and properties of electrospun poly (vinylidene fluoride) membranes. *Journal of applied polymer science*, *97*(2), 466-474.
129. Ren, X., & Dzenis, Y. (2006, January). Novel continuous poly (vinylidene fluoride) nanofibers. In *Materials Research Society Symposium Proceedings* (Vol. 920, p. 55). Warrendale, Pa.; Materials Research Society; 1999.
130. Huang, S., Yee, W. A., Tjiu, W. C., Liu, Y., Kotaki, M., Boey, Y. C. F., ... & Lu, X. (2008). Electrospinning of polyvinylidene difluoride with carbon nanotubes: synergistic effects of extensional force and interfacial interaction on crystalline structures. *Langmuir*, *24*(23), 13621-13626.

131. Sun, D., Chang, C., Li, S., & Lin, L. (2006). Near-field electrospinning. *Nano letters*, 6(4), 839-842.
132. Chang, C., Limkraisiri, K., & Lin, L. (2008). Continuous near-field electrospinning for large area deposition of orderly nanofiber patterns. *Applied Physics Letters*, 93(12), 123111.
133. Chang, C., Tran, V. H., Wang, J., Fuh, Y. K., & Lin, L. (2010). Direct-write piezoelectric polymeric nanogenerator with high energy conversion efficiency. *Nano letters*, 10(2), 726-731.
134. Tazaki, M., Wada, R., Abe, M. O., & Homma, T. (1997). Crystallization and gelation of poly (vinylidene fluoride) in organic solvents. *Journal of applied polymer science*, 65(8), 1517-1524.
135. Hasegawa, R., Kobayashi, M., & Tadokoro, H. (1972). Molecular Conformation and Packing of Poly (vinylidene fluoride). Stability of Three Crystalline Forms and the Effect. *Polymer Journal*, 3(5), 591-599.
136. Boccaccio, T., Bottino, A., Capannelli, G., & Piaggio, P. (2002). Characterization of PVDF membranes by vibrational spectroscopy. *Journal of membrane science*, 210(2), 315-329.
137. Matsushige, K., & Takemura, T. (1980). Crystallization of macromolecules under high pressure. *Journal of Crystal Growth*, 48(2), 343-354.
138. <http://en.wikipedia.org/wiki/Polycaprolactone>
139. Pham, Q. P., Sharma, U., & Mikos, A. G. (2006). Electrospun poly (ε-caprolactone) microfiber and multilayer nanofiber/microfiber scaffolds: characterization of scaffolds and measurement of cellular infiltration. *Biomacromolecules*, 7(10), 2796-2805.
140. Burger, C., Hsiao, B. S., & Chu, B. (2006). Nanofibrous materials and their applications. *Annu. Rev. Mater. Res.*, 36, 333-368.
141. Martins, A., Reis, R. L., & Neves, N. M. (2008). Electrospinning: processing technique for tissue engineering scaffolding. *International Materials Reviews*, 53(5), 257-274.
142. Kim, G. H. (2008). Electrospun PCL nanofibers with anisotropic mechanical properties as a biomedical scaffold. *Biomedical materials*, 3(2), 025010.
143. Lee, K. H., Kim, H. Y., Khil, M. S., Ra, Y. M., & Lee, D. R. (2003). Characterization of nano-structured poly (ε-caprolactone) nonwoven mats via electrospinning. *Polymer*, 44(4), 1287-1294.

144. Wong, S. C., Baji, A., & Leng, S. (2008). Effect of fiber diameter on tensile properties of electrospun poly (ϵ -caprolactone). *Polymer*, 49(21), 4713-4722.
145. Shi, Q., Wong, S. C., Ye, W., Hou, J., Zhao, J., & Yin, J. (2012). Mechanism of Adhesion between Polymer Fibers at Nanoscale Contacts. *Langmuir*, 28(10), 4663-4671.
146. Maeda, N., Chen, N., Tirrell, M., & Israelachvili, J. N. (2002). Adhesion and friction mechanisms of polymer-on-polymer surfaces. *Science*, 297(5580), 379-382.
147. Persson, B. N. J., & Gorb, S. (2003). The effect of surface roughness on the adhesion of elastic plates with application to biological systems. *The Journal of chemical physics*, 119, 11437.
148. Najem, J. F. (2012). *Gecko-Inspired Electrospun Flexible Fiber Arrays for Adhesion* (Doctoral dissertation, The University of Akron).
149. Wan, K. T., & Mai, Y. W. (1990). Fracture mechanics of a shaft-loaded blister of thin flexible membrane on rigid substrate. *International journal of fracture*, 74(2), 181-197.
150. Timoshenko, S., Woinowsky-Krieger, S., & Woinowsky, S. (1959). *Theory of plates and shells* (Vol. 2). New York: McGraw-hill.
151. Needleman, A. (1990). An analysis of decohesion along an imperfect interface. *International Journal of Fracture*, 42(1), 21-40.
152. Hbaieb, K., & Zhang, Y. W. (2005). A parametric study of a pressurized blister test for an elastic-plastic film-rigid substrate system. *Materials Science and Engineering: A*, 390(1), 385-392.
153. Tvergaard, V., & Hutchinson, J. W. (1992). The relation between crack growth resistance and fracture process parameters in elastic-plastic solids. *Journal of the Mechanics and Physics of Solids*, 40(6), 1377-1397.
154. Tvergaard, V., & Hutchinson, J. W. (1993). The influence of plasticity on mixed mode interface toughness. *Journal of the Mechanics and Physics of Solids*, 41(6), 1119-1135.
155. Jiang, L. M., Zhou, Y. C., Liao, Y. G., & Sun, C. Q. (2008). A pressurized blister test model for the interface adhesion of dissimilar elastic-plastic materials. *Materials Science and Engineering: A*, 487(1), 228-234.
156. Hillerborg, A., Modeer, M., & Petersson, P. E. (1976). Analysis of crack formation and crack growth in concrete by means of fracture mechanics and finite elements. *Cement and concrete research*, 6(6), 773-781.

157. Fridrikh, S. V., Yu, J. H., Brenner, M. P., & Rutledge, G. C. (2003). Controlling the fiber diameter during electrospinning. *Physical review letters*, 90(14), 144502.
158. Chowdhury, M., & Stylios, G. (2010). Effect of experimental parameters on the morphology of electrospun Nylon 6 fibres. *International Journal of Basic & Applied Sciences*, 10(06), 116-131.
159. Huang, Z. M., Zhang, Y. Z., Kotaki, M., & Ramakrishna, S. (2003). A review on polymer nanofibers by electrospinning and their applications in nanocomposites. *Composites science and technology*, 63(15), 2223-2253.
160. Zhao, Z., Li, J., Yuan, X., Li, X., Zhang, Y., & Sheng, J. (2005). Preparation and properties of electrospun poly (vinylidene fluoride) membranes. *Journal of applied polymer science*, 97(2), 466-474.
161. Shawon, J., & Sung, C. (2004). Electrospinning of polycarbonate nanofibers with solvent mixtures THF and DMF. *Journal of materials science*, 39(14), 4605-4613.
162. Zheng, J., He, A., Li, J., & Han, C. C. (2007). Polymorphism control of poly (vinylidene fluoride) through electrospinning. *Macromolecular Rapid Communications*, 28(22), 2159-2162.
163. Jeong, H. E., Lee, J. K., Kim, H. N., Moon, S. H., & Suh, K. Y. (2009). A nontransferring dry adhesive with hierarchical polymer nanohairs. *Proceedings of the National Academy of Sciences*, 106(14), 5639-5644.
164. Pu, J., Yan, X., Jiang, Y., Chang, C., & Lin, L. (2010). Piezoelectric actuation of direct-write electrospun fibers. *Sensors and Actuators A: Physical*, 164(1), 131-136.
165. Baji, A., Mai, Y. W., Li, Q., Wong, S. C., Liu, Y., & Yao, Q. W. (2011). One-dimensional multiferroic bismuth ferrite fibers obtained by electrospinning techniques. *Nanotechnology*, 22(23), 235702.
166. Smithgall, D. H., Watkins, L. S., & Frazee Jr, R. E. (1977). High-speed noncontact fiber-diameter measurement using forward light scattering. *Applied Optics*, 16(9), 2395-2402.
167. Jasapara, J., Monberg, E., DiMarcello, F., & Nicholson, J. W. (2003). Accurate noncontact optical fiber diameter measurement with spectral interferometry. *Optics letters*, 28(8), 601-603.
168. Benz, M., Rosenberg, K. J., Kramer, E. J., & Israelachvili, J. N. (2006). The deformation and adhesion of randomly rough and patterned surfaces. *The Journal of Physical Chemistry B*, 110(24), 11884-11893.
169. Wang, X., Najem, J. F., Wong, S. C., & Wan, K. T. (2012). A nano-cheese-cutter to directly measure interfacial adhesion of freestanding nano-fibers. *Journal of Applied Physics*, 111(2), 024315-024315.

170. Janarthanan, V., Garrett, P. D., Stein, R. S., & Srinivasarao, M. (1997). Adhesion enhancement in immiscible polymer bilayer using oriented macroscopic roughness. *Polymer*, 38(1), 105-111.
171. Litteken, C. S., & Dauskardt, R. H. (2003). Adhesion of polymer thin-films and patterned lines. *International journal of fracture*, 120(1), 475-485.
172. Li, M., Carter, C. B., Hillmyer, M. A., & Gerberich, W. W. (2001). Adhesion of polymer–inorganic interfaces by nanoindentation. *Journal of Materials Research*, 16(12), 3378-3388.
173. Choi, S. T., Lee, S. R., & Earmme, Y. Y. (2008). Measurement of time-dependent adhesion between a polymer film and a flat indenter tip. *Journal of Physics D: Applied Physics*, 41(7), 074023.
174. Erbil, H. Y., Yasar, B., Süzer, S., & Baysal, B. M. (1997). Surface characterization of the hydroxy-terminated poly (ε-caprolactone)/poly (dimethylsiloxane) triblock copolymers by electron spectroscopy for chemical analysis and contact angle measurements. *Langmuir*, 13(20), 5484-5493.
175. Larsson, M. P., & Ahmad, M. M. (2006). Improved polymer–glass adhesion through micro-mechanical interlocking. *Journal of Micromechanics and Microengineering*, 16(6), S161.
176. Lee, J. S., Kim, G. H., Hong, S. M., Choi, H. J., & Seo, Y. (2009). Surface Functionalization of a Poly (vinylidene fluoride): Effect on the Adhesive and Piezoelectric Properties. *ACS applied materials & interfaces*, 1(12), 2902-2908.
177. Peng, Z. L., & Chen, S. H. (2011). Effects of surface roughness and film thickness on the adhesion of a bioinspired nanofilm. *Physical Review E*, 83(5), 051915.
178. Nakagawa, K., & Ishida, Y. (2003). Annealing effects in poly (vinylidene fluoride) as revealed by specific volume measurements, differential scanning calorimetry, and electron microscopy. *Journal of Polymer Science: Polymer Physics Edition*, 11(11), 2153-2171.
179. McBain, J. W., & Hopkins, D. G. (1926). Films of adhesives. *The Journal of Physical Chemistry*, 30(1), 114-125.
180. Larsson, M. P., & Ahmad, M. M. (2006). Improved polymer–glass adhesion through micro-mechanical interlocking. *Journal of Micromechanics and Microengineering*, 16(6), S161.
181. Hine, P. J., Muddarris, S. E., & Packham, D. E. (1987). Adhesion of microfibrinous surfaces on steel and copper to epoxy resins. *Journal of Adhesion Science and Technology*, 1(1), 69-78.

182. Woods, D. W., & Ward, I. M. (1993). Study of the oxygen treatment of high - modulus polyethylene fibres. *Surface and interface analysis*, 20(5), 385-392.
183. Holmes, S., & Schwartz, P. (1990). Amination of ultra-high strength polyethylene using ammonia plasma. *Composites science and technology*, 38(1), 1-21.
184. Wang, Y. Y., Li, C. J., & Ohmori, A. (2005). Influence of substrate roughness on the bonding mechanisms of high velocity oxy-fuel sprayed coatings. *Thin Solid Films*, 485(1), 141-147.
185. Larsson, M. P., Syms, R. R. A., & Wojcik, A. G. (2005). Improved adhesion in hybrid Si-polymer MEMS via micromechanical interlocking. *Journal of micromechanics and microengineering*, 15(11), 2074-2082.
186. Gotoh, K. (1971). Distribution of particle spacings in a random dispersion. *Industrial & Engineering Chemistry Fundamentals*, 10(2), 315-316.
187. Arinstein, A., & Zussman, E. (2011). Electrospun polymer nanofibers: mechanical and thermodynamic perspectives. *Journal of Polymer Science Part B: Polymer Physics*, 49(10), 691-707.
188. Moura-Ramos, J. J., & Correia, N. T. (2001). The Deborah number, relaxation phenomena and thermally stimulated currents. *Phys. Chem. Chem. Phys.*, 3(24), 5575-5578.
189. Lu, J., Mirau, P. A., & Tonelli, A. E. (2001). Dynamics of isolated polycaprolactone chains in their inclusion complexes with cyclodextrins. *Macromolecules*, 34(10), 3276-3284.
190. Dannenberg, H. (1961). Measurement of adhesion by a blister method. *Journal of Applied Polymer Science*, 5(14), 125-134.
191. Wan, K. T., & Mai, Y. W. (1990). Fracture mechanics of a shaft-loaded blister of thin flexible membrane on rigid substrate. *International journal of fracture*, 74(2), 181-197.
192. Ko, S. H., Lee, D., Kang, H. W., Nam, K. H., Yeo, J. Y., Hong, S. J., ... & Sung, H. J. (2011). Nanoforest of hydrothermally grown hierarchical ZnO nanowires for a high efficiency dye-sensitized solar cell. *Nano letters*, 11(2), 666-671.
193. Kapadia, R., Ko, H., Chueh, Y. L., Ho, J. C., Takahashi, T., Zhang, Z., & Javey, A. (2009). Hybrid core-multishell nanowire forests for electrical connector applications. *Applied Physics Letters*, 94(26), 263110-263110.
194. Ko, H., Zhang, Z., Chueh, Y. L., Saiz, E., & Javey, A. (2010). Thermoresponsive Chemical Connectors Based on Hybrid Nanowire Forests. *Angewandte Chemie*, 122(3), 626-629.

195. Herman, I., Yeo, J., Hong, S., Lee, D., Nam, K. H., Choi, J. H., ... & Ko, S. H. (2012). Hierarchical weeping willow nano-tree growth and effect of branching on dye-sensitized solar cell efficiency. *Nanotechnology*, 23(19), 194005.
196. Na, H., Chen, P., Wan, K. T., Wong, S. C., Li, Q., & Ma, Z. (2012). Measurement of Adhesion Work of Electrospun Polymer Membrane by Shaft-Loaded Blister Test. *Langmuir*, 28(16), 6677-6683..
197. Hueso, L., & Mathur, N. (2004). Dreams of a hollow future. *Nature*, 427(6972), 301-304.
198. Hou, S., Harrell, C. C., Trofin, L., Kohli, P., & Martin, C. R. (2004). Layer-by-layer nanotube template synthesis. *Journal of the American Chemical Society*, 126(18), 5674-5675.
199. Wen X, & Tresco P. (2006) Fabrication and characterization of permeable degradable poly(dl- lactide-co-glycolide) (PLGA) hollow fiber phase inversion membranes for use as nerve tract guidance channels. *Biomaterials*. 27(20), 3800-3809.
200. Inoue, M., & Kawashima, K. (1987). *U.S. Patent No. 4,636,307*. Washington, DC: U.S. Patent and Trademark Office..
201. Schakenraad, J. M., Oosterbaan, J. A., Nieuwenhuis, P., Molenaar, I., Olijslager, J., Potman, W., ... & Feijen, J. (1988). Biodegradable hollow fibres for the controlled release of drugs. *Biomaterials*, 9(1), 116-120.
202. Brei, D., & Cannon, B. J. (2004). Piezoceramic hollow fiber active composites. *Composites science and technology*, 64(2), 245-261.
203. Barer S J, Besso M M. US patent 4636307.
204. Benabid, F., Bouwmans, G., Knight, J. C., Russell, P. S. J., & Couny, F. (2004). Ultrahigh efficiency laser wavelength conversion in a gas-filled hollow core photonic crystal fiber by pure stimulated rotational Raman scattering in molecular hydrogen. *Physical review letters*, 93(12), 123903.
205. Li, D., & Xia, Y. (2004). Direct fabrication of composite and ceramic hollow nanofibers by electrospinning. *Nano Letters*, 4(5), 933-938.
206. Nasir, M., & Kotaki, M. (2009). Fabrication of Aligned Piezoelectric Nanofiber by Electrospinning. *International Journal of Nanoscience*, 8(03), 231-235.
207. Loscertales, I. G., Barrero, A., Márquez, M., Spretz, R., Velarde-Ortiz, R., & Larsen, G. (2004). Electrically forced coaxial nanojets for one-step hollow nanofiber design. *Journal of the American Chemical Society*, 126(17), 5376-5377.

- 208.Chan, M. Y., Chan, T. K., Osipowicz, T., Chan, L., & Lee, P. S. (2009). Lanthanide-based graded barrier structure for enhanced nanocrystal memory properties. *Applied Physics Letters*, 95(11), 113113-113113.
- 209.Wang, C., Yan, K. W., Lin, Y. D., & Hsieh, P. C. (2010). Biodegradable core/shell fibers by coaxial electrospinning: Processing, fiber characterization, and its application in sustained drug release. *Macromolecules*, 43(15), 6389-6397.
- 210.Na, H., Liu, X., Li, J., Zhao, Y., Zhao, C., & Yuan, X. (2009). Formation of core/shell ultrafine fibers of PVDF/PC by electrospinning via introduction of PMMA or BTEAC. *Polymer*, 50(26), 6340-6349.
- 211.Yarin, A. L., Zussman, E., Wendorff, J. H., & Greiner, A. (2007). Material encapsulation and transport in core-shell micro/nanofibers, polymer and carbon nanotubes and micro/nanochannels. *Journal of Materials Chemistry*, 17(25), 2585-2599.
- 212.Moghe, A. K., & Professor BS Gupta. (2008). Co - axial Electrospinning for Nanofiber Structures: Preparation and Applications. *Polymer Reviews*, 48(2), 353-377.
- 213.Deshmukh, S. P., & Li, K. (1998). Effect of ethanol composition in water coagulation bath on morphology of PVDF hollow fibre membranes. *Journal of Membrane Science*, 150(1), 75-85.
- 214.Wang, D., Li, K., & Teo, W. K. (1999). Preparation and characterization of polyvinylidene fluoride (PVDF) hollow fiber membranes. *Journal of membrane science*, 163(2), 211-220.
- 215.Dror, Y., Salalha, W., Avrahami, R., Zussman, E., Yarin, A. L., Dersch, R., ... & Wendorff, J. H. (2007). One - Step Production of Polymeric Microtubes by Co - electrospinning. *Small*, 3(6), 1064-1073.
- 216.Theron, A., Zussman, E., & Yarin, A. L. (2001). Electrostatic field-assisted alignment of electrospun nanofibres. *Nanotechnology*, 12(3), 384-390.
- 217.Zhang, Y. Z., Wang, X., Feng, Y., Li, J., Lim, C. T., & Ramakrishna, S. (2006). Coaxial electrospinning of (fluorescein isothiocyanate-conjugated bovine serum albumin)-encapsulated poly (-caprolactone) nanofibers for sustained release. *Biomacromolecules*, 7(4), 1049-1057.
- 218.Wang, M., Jian, H. Y., Kaplan, D. L., & Rutledge, G. C. (2006). Production of submicron diameter silk fibers under benign processing conditions by two-fluid electrospinning. *Macromolecules*, 39(3), 1102-1107.
- 219.Prilutsky, S., Zussman, E., & Cohen, Y. (2008). The effect of embedded carbon nanotubes on the morphological evolution during the carbonization of poly (acrylonitrile) nanofibers. *Nanotechnology*, 19(16), 165603.

220. Elsner, N., Dubreuil, F., & Fery, A. (2004). Tuning of microcapsule adhesion by varying the capsule-wall thickness. *Physical Review E*, 69(3), 031802.
221. Na, H. N., Chen, P., Wong, S. C., Hague, S., & Li, Q. (2012). Fabrication of PVDF/PVA microtubules by coaxial electrospinning. *Polymer*, 53(13), 2736-2743.
222. Bormashenko, Y., Pogreb, R., Stanevsky, O., & Bormashenko, E. (2004). Vibrational spectrum of PVDF and its interpretation. *Polymer testing*, 23(7), 791-796.
223. Park, Y. J., Kang, Y. S., & Park, C. (2005). Micropatterning of semicrystalline poly (vinylidene fluoride)(PVDF) solutions. *European polymer journal*, 41(5), 1002-1012.
224. Teo, W. E., & Ramakrishna, S. (2006). A review on electrospinning design and nanofibre assemblies. *Nanotechnology*, 17(14), R89.
225. Mohammadi, B., Yousefi, A. A., & Bellah, S. M. (2007). Effect of tensile strain rate and elongation on crystalline structure and piezoelectric properties of PVDF thin films. *Polymer testing*, 26(1), 42-50.
226. Lu, F. J., & Hsu, S. L. (1984). Spectroscopic study of the electric field induced microstructural changes in poly (vinylidene fluoride). *Polymer*, 25(9), 1247-1252.
227. Sajkiewicz, P., Wasiak, A., & Gołowski, Z. (1999). Phase transitions during stretching of poly (vinylidene fluoride). *European polymer journal*, 35(3), 423-429.
228. Wei, X., Xia, Z., Wong, S. C., & Baji, A. (2009). Modelling of mechanical properties of electrospun nanofibre network. *International Journal of Experimental and Computational Biomechanics*, 1(1), 45-57.
229. Xia, Z., & Curtin, W. (2008). Multiscale modeling of tensile failure in fiber-reinforced composites. *Multiscale Modeling and Simulation of Composite Materials and Structures*, 37-82.
230. Wen, W., Huang, X., Yang, S., Lu, K., & Sheng, P. (2003). The giant electrorheological effect in suspensions of nanoparticles. *Nature Materials*, 2(11), 727-730.
231. Wen, W., Huang, X., & Sheng, P. (2007). Electrorheological fluids: structures and mechanisms. *Soft Matter*, 4(2), 200-210.
232. Huang, X., Wen, W., Yang, S., & Sheng, P. (2006). Mechanisms of the giant electrorheological effect. *Solid state communications*, 139(11), 581-588.
233. Halsey, T. C. (1992). Electrorheological fluids. *Science*, 258(5083), 761-766.
234. Tao, R., & Sun, J. M. (1991). Three-dimensional structure of induced electrorheological solid. *Physical review letters*, 67(3), 398-401.

235.Chen, Y., Sprecher, A. F., & Conrad, H. (1991). Electrostatic particle - particle interactions in electrorheological fluids. *Journal of applied physics*, 70(11), 6796-6803.

236.Wong, S. C. U.S. Patent Application 13359020, 2012.